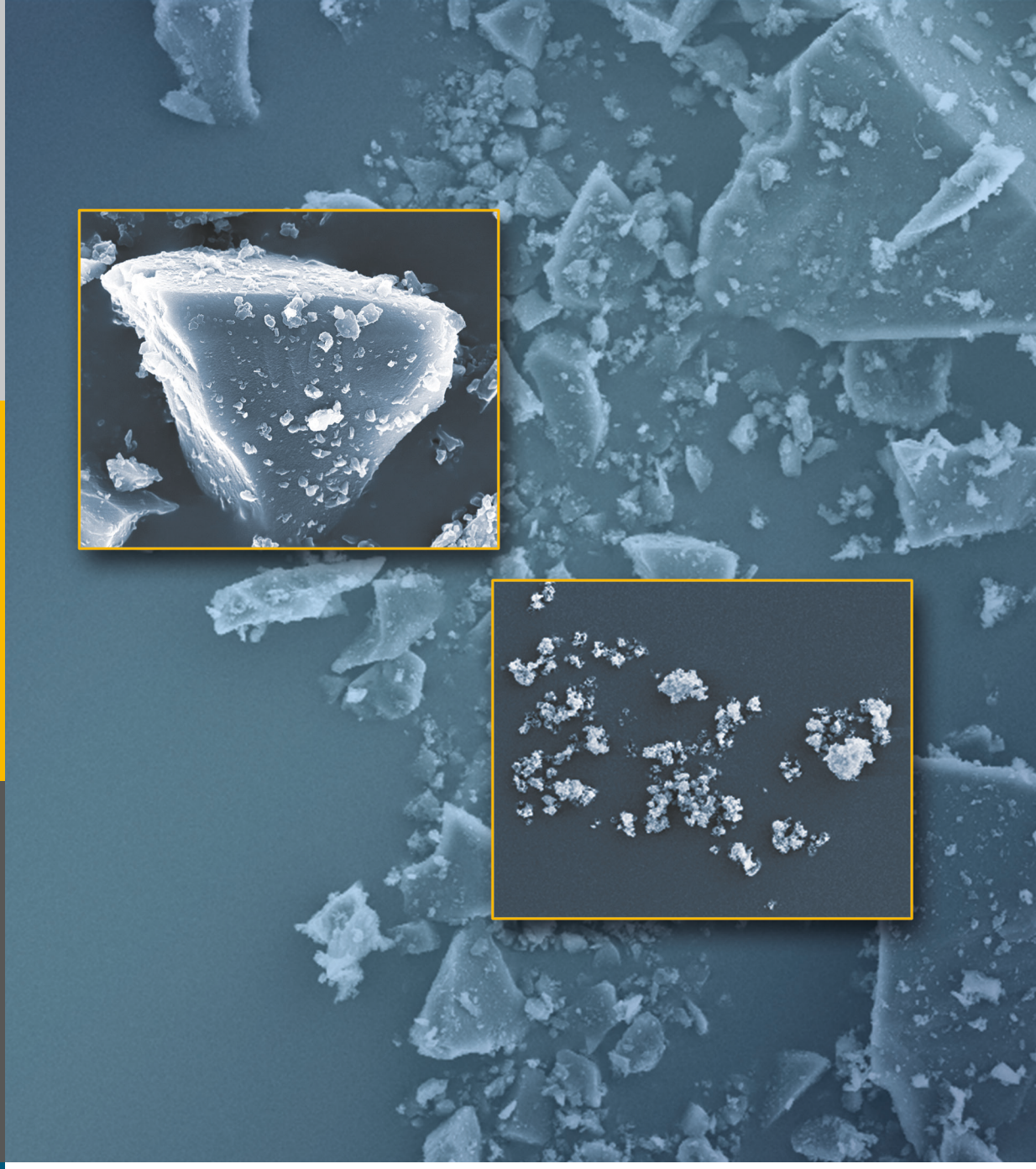

Study on the Complex Li-N-H Hydrogen Storage System

Linnan Du

Member of the Helmholtz Association

JÜLICH
FORSCHUNGSZENTRUM

Schriften des Forschungszentrums Jülich
Reihe Energie & Umwelt / Energy & Environment Band / Volume 211

Forschungszentrum Jülich GmbH
Institute for Energy and Climate Research (IEK)
Materials Synthesis and Processing (IEK-1)

Study on the Complex Li-N-H Hydrogen Storage System

Linnan Du

Schriften des Forschungszentrums Jülich
Reihe Energie & Umwelt / Energy & Environment Band / Volume 211

ISSN 1866-1793 ISBN 978-3-89336-952-2

Bibliographic information published by the Deutsche Nationalbibliothek.
The Deutsche Nationalbibliothek lists this publication in the Deutsche Nationalbibliografie; detailed bibliographic data are available in the Internet at http://dnb.d-nb.de.

Publisher and Distributor: Forschungszentrum Jülich GmbH
Zentralbibliothek
52425 Jülich
Tel: +49 2461 61-5368
Fax: +49 2461 61-6103
Email: zb-publikation@fz-juelich.de
www.fz-juelich.de/zb

Cover Design: Grafische Medien, Forschungszentrum Jülich GmbH

Printer: Grafische Medien, Forschungszentrum Jülich GmbH

Schriften des Forschungszentrums Jülich
Reihe Energie & Umwelt / Energy & Environment, Band / Volume 211

D 294 (Diss., Bochum, Univ., 2013)

ISSN 1866-1793
ISBN 978-3-89336-952-2

The complete volume is freely available on the Internet on the Jülicher Open Access Server (JUWEL) at www.fz-juelich.de/zb/juwel

Abstract

Nowadays the developments of clean energy technologies become more and more necessary and important. Hydrogen-powered vehicles are a promising alternative to the current fossil fuel based vehicle infrastructure. However, so far there is still no hydrogen storage material which can fit the standards for an on-board hydrogen storage system.

On this background, this work deals with the development of a hydrogen storage material. The focus is put on the Lithium amide + Lithium hydride ($LiNH_2$+LiH) hydrogen storage system because of its high theoretical capacity and relatively low desorption temperature. Moreover, Lithium amide + Magnesium hydride ($LiNH_2$+MgH_2) as an alternative system was also briefly studied.

The aims of this work are to achieve a deeper understanding of the reaction mechanism with the help of microstructural and thermodynamic studies, building a model to describe the sorption process and then to improve the system properties.

As the desorption from $LiNH_2$ particles is the first step of the desorption process of the $LiNH_2$+LiH system, the properties and sorption behavior of $LiNH_2$ sample materials were studied separately first. So the work in this thesis can be mainly divided into two parts: $LiNH_2$ samples and $LiNH_2$+LiH samples. In order to activate the sample materials, both dry ball milling and wet ball milling (with tetrahydrofuran) methods were used. Boron nitride was mainly applied as catalyst. Furthermore, titanium tetrachloride was also used as an alternative additive. The sorption behaviors were studied with the help of a volumetric and a gravimetric system. Further investigation methods include X-ray Diffraction (XRD) method, Scanning Electron Microscope (SEM), Brunauer–Emmett–Teller (BET) method, Differential Thermal Analysis (DTA)/ Thermo Gravimetric Analysis (TGA)/ Mass Spectrometry (MS), and others.

The results obtained in this work show that no obvious microstructure differences have been found between the wet ball milled and dry ball milled samples. Boron nitride (BN) as additive has improved the recyclability of the $LiNH_2$+LiH system clearly. The activation energy of the desorption reaction of wet- and dry ball milled samples have been reduced with BN as additive. BN did neither influence the crystallite sizes nor the particle sizes of both of the $LiNH_2$ and $LiNH_2$+LiH as milled samples clearly. However, it has been found that BN can stabilize the crystallite sizes of $LiNH_2$+LiH samples during the high temperature desorption and absorption processes. Titanium tetrachloride as alternative additive had also improved the recyclability of $LiNH_2$+LiH samples. However, the resulted system pressure was not as high as that of the $LiNH_2$+LiH samples with BN as additive. BN did not improve the recyclability of the $LiNH_2$+MgH_2 samples. Apart from the experimental work, a model to describe the desorption behavior of $LiNH_2$ particles was developed to understand the desorption process.

Kurzfassung

In der heutigen Zeit nimmt die Entwicklung von Technologien zur Nutzung erneuerbarer Energien einen hohen Stellenwert ein. Wasserstoff bietet sich als vielversprechende Alternative zu den aktuell überwiegend verwendeten fossilen Brennstoffen an, insbesondere auch im Bereich der individuellen Mobilität. Allerdings ist gegenwärtig kein Speichermaterial verfügbar, das alle Anforderungen für die Wasserstoffspeicherung im Fahrzeug zufriedenstellend erfüllt.

Vor diesem Hintergrund beschäftigt sich die vorliegende Arbeit mit der Entwicklung eines Wasserstoffspeichermaterials. Der Fokus liegt hier auf dem System $LiNH_2$+LiH. Interessant wird dieses System durch seine hohe theoretische Wasserstoffspeicherkapazität sowie eine vergleichsweise niedrige Desorptionstemperatur. Darüber hinaus wurde $LiNH_2$+MgH_2 als Alternativsystem untersucht.

Ziel dieser Arbeit ist es anhand von Mikrostruktur- und thermodynamischen Untersuchungen ein tieferes Verständnis der Reaktionsmechanismen im System zu erlangen. Zudem soll ein Modell erarbeitet werden, welches die Sorptionsprozesse des Systems beschreibt. Nicht zuletzt sollen die gewonnen Erkenntnisse in die Weiterentwicklung des Systems einfließen.

Die vorliegende Arbeit gliedert sich in zwei Hauptteile. Da die Zersetzung von $LiNH_2$-Partikeln den ersten Schritt des Desorptionsprozesses im $LiNH_2$+LiH-System darstellt, wurde dieser Schritt im ersten Teil der vorliegenden Arbeit separat betrachtet. Im zweiten Teil der Arbeit steht das Gesamtsystem $LiNH_2$+LiH im Vordergrund. Um das Probenmaterial zu aktivieren, wurden sowohl trockene als auch nasse Kugelmahlprozesse eingesetzt. Bei der Mehrzahl der Versuche wurde Bornitrid als Katalysator eingesetzt. Alternativ wurde auch Titantetrachlorid verwendet. Zur Untersuchung des Sorptionsverhaltens standen sowohl ein volumetrisches als auch ein gravimetrisches System zur Verfügung. Weitere Charakterisierungsmethoden umfassen unter anderem Röntgenbeugung, Rasterelektronenmikroskopie, BET-Messungen und TG/DTA-MS.

Die im Rahmen dieser Arbeit erzielten Ergebnisse zeigen, dass hinsichtlich der Mikrostruktur keine erkennbaren Unterschiede zwischen nass- und trockengemahlenen Proben auftreten. Die Zugabe von Bornitrid als Additiv hat die Rezyklierbarkeit des Systems $LiNH_2$+LiH klar verbessert. Durch die Zugabe von Bornitrid als Additiv konnte die Aktivierungsenergie der Desorptionsreaktion sowohl für die nass- als auch der trocken gemahlenen Proben gesenkt werden. Weder hatte die Zugabe von Bornitrid einen deutlichen Einfluss auf die Kristallitgröße noch auf Partikelgröße von $LiNH_2$ und $LiNH_2$+LiH nach dem Mahlprozess. Jedoch konnte gezeigt werden, dass Bornitrid zu einer Stabilisierung der Kristallitgröße während der Hochtemperaturdesorptions- und -adsorptionsprozesse führt. Titantetrachlorid als alternatives Additiv führte ebenfalls zu einer verbesserten Rezyklierbarkeit der $LiNH_2$+LiH Proben. Der resultierende Systemdruck war jedoch niedriger als beim Einsatz von Bornitrid als Additiv. Durch den Einsatz von Bornitrid konnte bei den $LiNH_2$+MgH_2 Proben keine Verbesserung der Rezyklierbarkeit erreicht werden. Um den Desorptionsprozess besser zu verstehen, wurde neben den experimentellen Arbeiten ein Modell entwickelt, welches das Desorptionsverhalten von $LiNH_2$-Partikeln beschreibt.

Table of Contents

List of Abbreviations

BET	Brunauer–Emmett–Teller
CGH2	Compressed Gaseous Hydrogen
CV Model	Contracting Volume Model
DOE	United States Department of Energy
DTA	Differential Thermal Analysis
DTG	Differential Thermo Gravimetric
FWO Method	Flynn-Wall-Ozawa Method
IEK	Institute of Energy and Climate Research
JMA Model	Johnson-Mehl-Avrami Model
KAS Method	Kissinger–Akahira–Sunose Method
MOF	Metal Organic Framework
MS	Mass Spectrometry
MSB	Magnetic Suspension Balance
P-B Ratio	Pilling-Bedworth Ratio
QBSD	Quadrant Back Scattering Detector
SEM	Scanning Electron Microscopy
SSA	Specific Surface Area
TGA	Thermo Gravimetric Analysis
THF	Tetrahydrofuran (C_4H_8O)
XRD	X-ray Diffraction
YSZ	Yttria-Stabilized Zirconia

1. Introduction

1.1 Clean Energy and Hydrogen

In the last century, the energy supply was mainly based on coal, crude oil, and natural gas [Var10]. However, this fossil fuel-based economy will lead to several new problems in the future. The first one is the shortage of the crude oil supply. The so called “Hubbert peak theory” shows that the world crude oil production will decline in the near future. This theory can be applied not only to crude oil, but to many other natural resources, e.g. gas [Ben02], coal [Tao06], etc. Other problems arise due to the growing amounts of the greenhouse gas CO_2 in the atmosphere and the difficulties to control global warming and climate changes. From this it becomes clear that progress in carbon-free energy sources is essential to protect our environment and the development of the whole world.

Nowadays carbon-free energies mainly include wind energy, solar energy, hydrogen energy, etc. Lately, the first two energy sources have been developed well. However, both of them are fluctuating sources and the produced energy is not easily storable and transportable [Cro10]. In this context, hydrogen energy has attracted attention as a clean energy storage alternative. It is carbon-free, abundantly available from water, and has an exceptional gravimetric energy density which can reach up to 142 MJ/kg [Bro11]. However, the problem is that at atmospheric pressure hydrogen exists as low density gas. For example, 1 kg of hydrogen occupies a volume of about 12 m^3 at room temperature and atmospheric pressure. Therefore suitable hydrogen storage materials with high storage capacities are an important issue for the hydrogen energy economics.

1.2 Hydrogen Storage Target

The US Department of Energy (DOE) has defined the standards for an on-board hydrogen storage system. The target for the year 2010 [Uni05, Kle13] was a system storage capacity exceeding 6 wt% (2.0 kWh/kg) around 100°C [Osb09]. However, at the time of writing, a new target has been set [Uni09] for the year 2017, which is 5.5 wt% (1.8 kWh/kg). Moreover, the new target also requires a volumetric energy density of 1.3 kWh/l (0.04kg/l), a refueling time of less than 3.3 min per 5 kg, a minimum lifetime of 1500 hydrogenation/dehydrogenation cycles and a net storage system cost of less than 2 USD/kWh. Until now there is still no system which can satisfy all these demands. Table 1.1 shows the subset of original and revised DOE targets for on-board hydrogen storage systems for light-duty vehicles.

Table 1.1: A subset of original and revised DOE targets for on-board hydrogen storage systems for light-duty vehicles [Kle13]

Storage system parameter	Original 2010 target	Revised 2010 target	2017 target
Gravimetric capacity (%)	6	4.5	5.5
Volumetric capacity (g H_2/l)	45	28	40
Operational life (numbers of cycles)	1000	1000	1500
Fill time for 5 kg (min)	3	4.2	3.3
Minimum full flow rate (g H_2/(s*kW)	0.02	0.02	0.02
Min. delivery pressure (atm)	8	5	4
Fuel Purity (%)	99.99	99.97	99.97

1.3 Motivation and Aim of the Work

As discussed in section 1.1, nowadays it becomes more and more urgent and important to develop clean energy in order to protect the environment. Hydrogen storage material development is one essential part for the hydrogen energy development. At the moment several different hydrogen storage materials are available. However, state-of-the-art hydrogen storage materials do not meet all the requirements shown in Table 1.1.

From the requirements for the storage capacity, it follows that the physical hydrogen storage materials are far below the stated requirements. However, complex hydrides are promising materials to fulfill the requirements due to their higher hydrogen storage capacity. Among the complex hydrides, the $LiNH_2$+LiH system holds a relatively high theoretical storage capacity (>6 wt%) and low desorption temperature (< 250°C).

On this background, the specific aim of this work is to develop a hydrogen storage material based on the $LiNH_2$+LiH system. A deeper understanding of the material´s hydrogen desorption mechanisms shall be achieved by means of microstructural and thermodynamic studies and help to further enhance hydrogen storage properties of the material.

1.4 Outline

Chapter 2 begins with an overview of novel solid hydrogen storage materials, including physical and chemical storage materials. Their main advantages and disadvantages are illustrated. The $LiNH_2$+LiH hydrogen storage material is introduced in a separate subchapter with more details. That includes the reaction equations, thermaodynamic values, possible activation methods and state-of-the-art model analysis development. Methods to characterize gas sorption ability and theoretical background of the thermodynamic calculation are also introduced in chapter 2.

Chapter 3 gives the introduction of the experiment materials and experimental methods used in this study. In order to reduce the particle sizes of the samples, the ball milling method was used. Characterization methods are amongst others XRD, SEM, DTA/TG and BET. There are two devices to characterize the desorption and absorption ability of the samples, namely the volumetric Belsorp-HP system and the gravimetric system ISOSORP-MSB.

Chapter 4 is devoted to describe the experimental results and discuss them. As the $LiNH_2$ decomposition is the first step of the desorption process, the desorption behavior of the $LiNH_2$ powders influence the system performance critically. Due to this reason, the characters of $LiNH_2$ were studied in the first part of Chapter 4. Beside normal dry ball milling process, some samples have also been wet ball milled with tetrahydrofuran (THF). Some of the samples were doped with 3 wt% boron nitride (BN) as catalyst.

In the second part of Chapter 4, the $LiNH_2$+LiH samples are investigated. The dry ball milled and wet ball milled (with THF) samples with different milling time are studied. $LiNH_2$+LiH samples have been doped with different amounts of BN. Titanium tetrachloride ($TiCl_4$) as an alternative additive has also been tried with the $LiNH_2$+LiH samples. Furthermore, a short investigation was also done with the $LiNH_2$+MgH_2 system.

Additionally, a model has been built up to describe the desorption process of the $LiNH_2$ powders in Belsorp-HP system. However, some of the parameters of the model still need to be further adjusted to the experiment results.

2. Background

2.1 Physical Hydrogen Storage Methods and Materials

2.1.1 Gaseous Storage

The storage of gases in pressure vessels is a tested and viable technology. For hydrogen gas, this state is called compressed gaseous hydrogen (CGH_2 or CGH2). It is also currently the main hydrogen storage method used in automotive applications. Compressed hydrogen storage refers to storing hydrogen at high pressures, typically 35-70 MPa [Hua11]. Figure 2.1 shows a typical CGH2 tank suitable for a small car.

Figure 2.1: Example for a CGH2 tank with a storage density of 40.2 kg/m^3 (70 MPa) [VBG12]

Gas phase hydrogen storage is a relatively easy method. Compared to liquid phase storage, the energy demand for compression is significantly less. On the other hand, it is still of disadvantage that a relatively large volume is required.

2.1.2 Liquid Storage

Other than gas, hydrogen can also be stored as liquid at -253°C. Liquefaction was first achieved by Dewar in the year 1898 [Dew98]. The density of liquefied gases can reach 70 kg/m^3[Sat07], which is considerably higher compared to gas phase storage. However, the volumetric energy

of liquid hydrogen is still low as compared to other fuels; approximately a factor of 4 as compared to gasoline [God12].

Figure 2.2: Example of a liquid hydrogen fuel tank in the boot of a car [Ble12]

When storing hydrogen as liquid, the energy required to liquefy is critical [Heu03]. On the other hand, state-of-the-art applications for passenger vehicles consist of double-wall cylindrical tanks that hold a hydrogen storage mass of up to 10 kg. One example is shown in Figure 2.2. The ideal shell material of the tank is stainless steel, because it is very resistant to hydrogen brittleness and shows very low hydrogen permeability. This, however, increases the weight of the whole tank system including valves and heat exchanger to more than 100 kg [Kra03].

2.1.3 Carbon

Carbon materials such as activated carbon, carbon nanotubes and carbon nanofibers are the subjects of intensive study for hydrogen storage. This group of materials has a high specific surface area, which can physically absorb hydrogen on the surface or in the internal volume of the porous structures. The hydrogen storage ability depends nearly linearly on the specific surface area of the material [Jim09]. A typical proportionality constant between storage ability and the specific surface area is about 1.3 $x10^{-3}$wt% gm^{-2} [Ebe09]. The absorption mechanism is physical absorption, which means the bond between hydrogen molecular and carbon material is very weak. Therefore, high pressures and low temperatures are typically required for hydrogen storage with carbon material.

2.1.3.1 Carbon Nanofibers

The term graphite nanofiber is used in parallel to the term carbon nanofiber [Str06]. There are mainly three structural forms of carbon nanofibers: tubular, platelet and herringbone. They are classified by the angle of the graphite layer with respect to the filament axis.

Figure 2.3 shows the structure of a graphite nanofiber and details of the hydrogen absorption process. The interlayer spacing (0.34 nm) is sufficiently large to allow for the entrance of molecular hydrogen (diameter 0.29 nm) while restricting the entrance of other gas molecules such as oxygen and nitrogen. According to the early reports, the hydrogen storage ability can reach 3.3 wt % at 298 K and a pressure of 4.83 MPa [Hua07]. Hydrogen storage densities up to 7 wt% were reported to be achieved by Dillon et al. [Dil00]. However, according to later more fully reproducible and convincing data [Jim09], the storage ability of carbon nanofibers is actually very low (around 0.04 wt%).

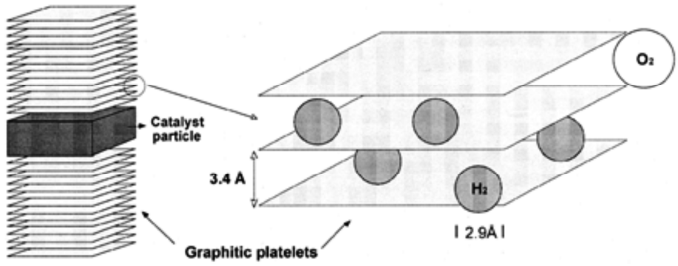

Figure 2.3: Schematic representation of the structure of a graphite nanofiber and details of the hydrogen absorption process [Ter98]

2.1.3.2 Carbon Nanotubes

Besides carbon nanofibers, carbon nanotubes (CNTs) with empty inner spaces and inter-tube spaces have been investigated intensively as hydrogen storage material in recent years.

Carbon nanotubes can be further classified into 2 groups: multi-walled nanotubes (MWNTs) and single-walled nanotubes (SWNTs). The SWNTs are a kind of fullerene, seamless cylinders wrapped with graphite. The diameter is 1-3 nm [Ku02]. MWNTs consist of multiple layers of graphite rolled on themselves to form tube shapes. Figure 2.4 shows the schematic diagrams of

SWNTs and MWNTs. MWNTs can be classed into two groups: Russian doll model and parchment model. For the MWNTs with the Russian doll model, sheets of graphite are arranged in concentric cylinders; while for the parchment model, a single sheet of graphite is rolled in around itself, similar to a rolled up paper. The inner diameter of MWNTs is about 1.5-15 nm, the outer diameter is around 2.5-30 nm and the interlayer distance is always in the range of 0.34-0.36 nm [Str06].

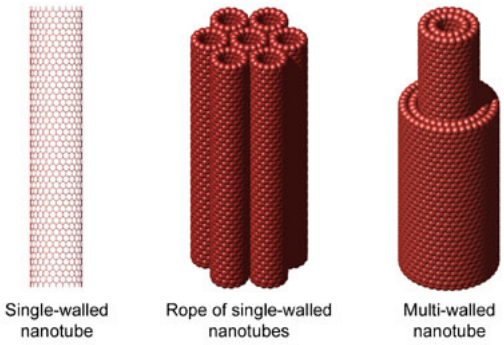

Figure 2.4: Schematic diagrams of single-walled carbon nanotubes (SWNTs) and multi-walled carbon nanotubes (MWNTs) [Nan13]

The hydrogen storage ability of carbon nanotubes shows no big difference from that of carbon nanofibers. Although really high sorption capacity for carbon nanotubes was reported in early report [Che01], it is now widely accepted that these results were incorrect and more reliable data have been published in the past few years suggesting that the adsorption of carbon nanotubes or carbon nanofibers shows a comparable behavior as that of other carbon materials [Ebe09].

2.1.3.3 Activated Carbon

Other than carbon nanotubes and carbon nanofibers, activated carbon has been utilized for decades to store gases. The production methods can be classified into physical reactivation and chemical activation. For physical reactivation, carbon containing material is first pyrolyzed at temperatures around 600-900°C in inert atmosphere. Then, the carbonized material is exposed

to oxidizing atmospheres. For chemical activation, prior to carbonization, the raw material is impregnated with certain chemicals. The chemical is typically an acid, strong base, or a salt. Activated carbon is much cheaper to produce than carbon nanofibers or carbon nanotubes. At the same time, the specific surface area is even larger than that of the other two materials [Jim09]. Properties such as porosity, pore size distribution (PSD), and specific surface area (SSA) of the material largely affect the hydrogen storage capability.

Some scientists have also tried to use activated carbon as structure material for hydride hydrogen storage material. The methods include chemical impregnation [Fan08] and melt infiltration [Gao10]. The results showed that the hydrogen desorption kinetics were improved.

2.2.4 Metal-Organic Frameworks (MOFs)

MOFs (also called coordination frameworks, coordination network materials or coordination polymers) are novel hydrogen storage materials. These materials are crystalline coordination polymers which contain organic ligands as linkers and metal ions or clusters as nodes. The hydrogen storage mechanism for MOFs is also, as activated carbon physical sorption. The illustration of MOFs synthesis and chemical composition is shown in Figure 2.5. The most important character of MOFs is that they have a much higher surface area (e.g., 5900 m^2/g [Zha08]) than carbon materials (1000 m^2/g or less) [Kum11].

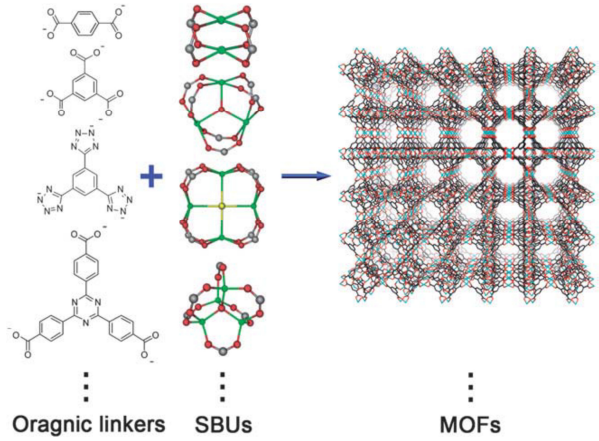

Figure 2.5: Illustration of MOFs synthesis and chemical composition [Zha08]

Rosi and co-workers [Ros03] were among the first to study the hydrogen uptake behavior of MOFs. They established a hydrogen uptake of 4.5 wt% at 78 K and 1 wt% at ambient temperature and a pressure of 20 bar. Compared with carbon materials, MOFs always show better hydrogen storage capability at very low temperature (77K). The key objective to enhance the hydrogen uptake of MOFs is to strengthen the interaction between hydrogen and the framework.

2.2 Chemical Hydrogen Storage Materials

2.2.1 Metal Hydrides

Although the first metal hydride was discovered more than 100 years ago, intensive research on this class of materials is relatively new [Hir10]. One important application of metal hydrides began in the 1960s, when metal hydrides were applied as negative electrodes of nickel-metal hydride (Ni-MH) batteries [Bro11]. This has been the most successful commercial application of metal hydrides. On the other hand, metal hydrides are also exploited in a number of other applications, such as gas separation and purification, temperature sensing, thermal compression, etc. Nowadays, metal hydrides form an important group among chemical hydrogen storage materials. Figure 2.6 shows a schematic of a metal hydride.

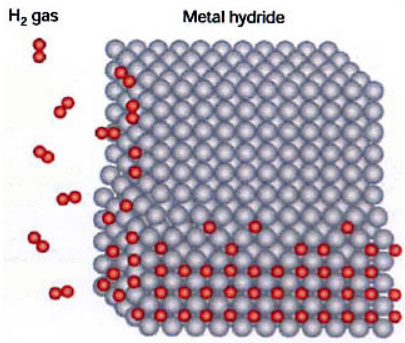

Figure 2.6: Schematic of a metal hydride. Hydrogen molecules (red) are inserted in between the atoms of the solid metal lattice [Sch01]

With some metals and alloys, hydrogen forms metal hydrides leading to solid-state hydrogen storage at moderate temperatures and pressures. This gives them the important safety benefit over the gas and liquid storage methods [Sak07]. Many metal alloys can react with hydrogen reversibly to form metal hydrides. However, only a few are appropriate for hydrogen storage [Heu03]. They must absorb and desorb hydrogen at moderate temperature and pressure; and second, they must be stable to keep their reactivity and capacity over many cycles. They can primarily be divided into two groups: intermetallic compounds and solid solution alloys.

For the intermetallic compounds, the host materials are ordered stoichiometric compounds typically formed from two metallic components A and B, where element A has a high affinity to hydrogen and element B has a low affinity to hydrogen [Zue03]. When AB reacts with hydrogen, the A and B components tend to form hydrides AH_x and BH_y, with enthalpies of formation ΔH_A and ΔH_B, representing a stable and an unstable hydride respectively. Compared to pure metal hydrides, intermetallic hydrides are considered to have a wider range of hydride stability. After reaction with hydrogen, the resultant intermetallic hydride $A_mB_nH_z$ (m and n are integers and z is a real number) has an enthalpy of formation: ΔH_{AB}, where $\Delta H_A<\Delta H_{AB}<\Delta H_B$ [Bro11]. Different n/m ratios influence the value of ΔH_{AB}. Hydrogen-absorbing intermetallics form several different groups, which can be distinguished according to their stoichiometry, including AB_5, AB_2, AB_3, A_2B_7, A_6B_{23}, AB and A_2B compounds. Some examples are shown in Table 2.1.

The application of intermetallic hydride compounds began with the negative electrode of Ni-MH batteries in the 1960s [Bro11]. However, the storage capacities of this group of materials are still far away from the DOE target quoted in Table 1.1.

Solid solution alloys, formed by dissolving one or more hydrogen-absorbing metallic elements in another, show also interesting hydrogen storage properties. Unlike the intermetallics described above, these materials do not necessarily have stoichiometric or near-stoichiometric compositions [Bro08]. They can be formed from a number of host solvents, including Pd, Ti, Zr and V. The so-called Laves phase-related Body-centered cubic (BCC) solid solution alloys are related materials, which are Ti–V–Mn, Ti–V–Cr, and Ti–V–Cr–Mn compounds that contain both Laves and BCC phases. However, similar to the intermetallic compounds, this group of material has a hydrogen capacity (2.2 wt% [Aki97]) which is much lower than the DOE target cited in Table 1.1.

Table 2.1: The most important families of hydride-forming intermetallic compounds [Zue03, Sch01]

Intermetallic compound type	Example	Theoretical capacity in wt%
AB_5	$LaNi_5$	1.37
AB_2	ZrV_2 $ZrMn_2$	3.01
AB_3	$CeNi_3$ YFe_3	
A_2B_7	Y_2Ni_7 Th_2Fe_7	
A_6B_{23}	Y_6Fe_{23}	
AB	TiFe ZrNi	1.89
A_2B	Mg_2Ni Ti_2Ni	3.59

There is a metal hydride which plays a very important role as hydrogen storage material: magnesium hydride (MgH_2). At first sight, MgH_2 is an attractive material. It exhibits a relatively low molecular weight, high hydrogen storage capacity (gravimetric capacity: 7.66 wt%), and a low material price. However, MgH_2 also has disadvantages such as slow reaction kinetics and high decomposition temperature. Apart from its high thermodynamic stability (ΔH = -75 kJ/mol H_2 [Bro08]), the kinetics of hydride formation and decomposition of the bulk material are too slow for practical purposes. MgH_2 has already been the subject of extensive investigations for more than 20 years to improve its kinetics of desorption and absorption of hydrogen and the cycle stability. For example, ball milling, doping and alloying are the most frequently used methods to improve the kinetic of hydrogen storage in the MgH_2 system. Many additives have been studied in order to improve this property. Figure 2.7 shows the catalytic effect of different transition metal oxides on the hydrogen desorption rate for MgH_2. It seems that nowadays the possibility to improve the properties of pure MgH_2 is rather limited.

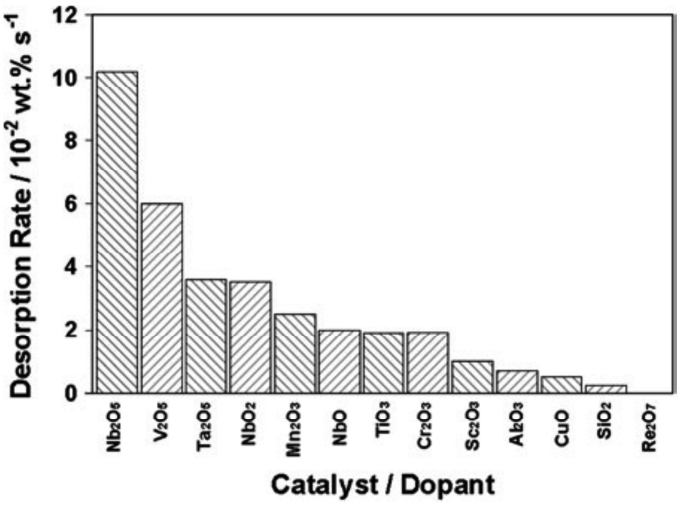

Figure 2.7: The catalytic effect of various transition metal oxides on the hydrogen desorption rate for MgH_2. Reaction rates were determined between 20% and 80% of the maximum hydrogen storage capacity in each case [Bar06]

2.2.2 Complex Hydrides

Some of the lightest elements in the periodic table, for example lithium, boron, sodium and aluminum can form stable, ionic hydrides [Sch01]. The most promising classes of materials for hydrogen storage are borohydrides, alanates and nitrides. During the decomposition process, hydrogen can be released while the complex hydride materials decompose into two or more components. Complex hydrides materials have many advantages. Specifically speaking, some complex hydrides have extremely high hydrogen mass percents ($LiNH_4$: 18.4 wt %) that surpass the current DOE targets. However, most complex hydrides desorb the hydrogen at very high temperature. For some systems, the reversibility of the reaction is not yet clear. Because of this, many studies have been focused on the improvement of the recyclability or the desorption kinetics in order to lower the desorption temperature of the materials.

2.2.2.1 Borohydrides

As mentioned before, borohydrides are an important group within the complex hydride storage materials. Borohydrides have the highest gravimetric hydrogen storage capacities of any of the complex hydrides [Bro08]. The desorption temperature and gravimetric hydrogen densities for several borohydrides are shown in Table 2.2.

Table 2.2: Desorption temperature (T_{des}) and gravimetric storage capacities of several borohydrides [Gro04, Ori07]

Compound	T_{des} (°C)	Storage capacity (wt%)
$LiBH_4$	380 950	13.8 18.4
$NaBH_4$	400	10.6
KBH_4	500	7.4
$Mg(BH_4)_2$	260-280	14.8
$Ca(BH_4)_2$	320	11.5

Among the group of borohydrides, $LiBH_4$ has a very high gravimetric hydrogen density (18.4 wt%). It has therefore attracted great interest as candidate hydrogen storage material. The thermodynamics, kinetics, and reversibility are the three main challenges being studied today.

The decomposition of $LiBH_4$ to desorb H_2 is realized in two steps [Wel09]:

Step 1: $\mathbf{LiBH_4 \rightarrow LiH + B + \frac{3}{2}H_2}$ **[13.8 wt%]** **Equation 2.1**

Step 2: $\mathbf{2LiH \rightarrow 2Li + H_2}$ **[4.6 wt%]** **Equation 2.2**

Step 1 takes place at 380°C without catalyst, while decomposition of LiH occurs at around 950°C [Au06]. The decomposition temperature, especially the temperature for the second step is too high for practical purposes. The dehydrogenation reaction of $LiBH_4$ is a reversible process, although the hydrogen absorption process requires elevated pressures and temperatures of 35.0 MPa at 600°C and 20.0 MPa at 690°C [Bro08].

Other borohydrides in Table 2.2 exhibit a higher hydrogen storage capacity than other groups of hydrogen storage materials as well. What should be noticed is that these are all theoretical values and most of them cannot be reversibly achieved in practice at relevant temperatures [Bro08]. However, as all the complex hydrides show high theoretical capacities, further studies of these materials seem worthwhile.

A newly developed borohydride was suggested for hydrogen storage: $Li_2B_{12}H_{12}$. According to theoretical calculations [Ohb06] and experimental results [Hwa08], it is an intermediate species in the decomposition process of $LiBH_4$. This was an important breakthrough in understanding the reaction mechanism of $LiBH_4$. Many materials have been tried to destabilize $LiBH_4$. For example, a report about the effect of boron on the activation energy of the decomposition of $LiBH_4$ showed that the kinetics of dehydrogenation was significantly enhanced by the addition of amorphous boron to pure $LiBH_4$ [Pen09]. This large impact of boron on the decomposition temperature demonstrated a new way to optimize dehydrogenation.

2.2.2.2 Alanates

Alanates are another group of complex hydrides. The most intensively studied reversible complex aluminum hydride is the sodium compound $NaAlH_4$. $NaAlH_4$ has a reversible hydrogen content of 5.6 wt% H_2. The decomposition of $NaAlH_4$ to liberate H_2 is realized in the following three steps:

Step 1: $\mathbf{3NaAlH_4 \rightarrow Na_3AlH_6 + 2Al + 3H_2}$ **Equation 2.3**

Step 2: $\mathbf{Na_3AlH_6 \rightarrow 3NaH + Al + \frac{3}{2}H_2}$ **Equation 2.4**

Step 3: $\mathbf{3NaH \rightarrow 3Na + \frac{3}{2}H_2}$ **Equation 2.5**

The reaction enthalpy (ΔH_r) for the first step is 37 kJ/mol H_2 while for the second step it is 47 kJ/mol H_2. The enthalpy values correspond to dehydrogenation temperatures of about 35°C and 100°C, respectively. The theoretical storage capacity of 7.4 wt% can be achieved by the

third step. However, because NaH is very stable, the third step requires temperature above 500°C. The disadvantage of alanates is that their reversibility is very limited. The irreversibility of this reaction, the instability of the hydride and the slow desorption kinetics are reasons why this material is not considered a particularly promising hydrogen storage material [Bro08]. Other alanates such as $KAlH_4$, $LiAlH_4$, $Ca(AlH_4)_2$ and $Mg(AlH_4)_2$ have also been considered for hydrogen storage. Their theoretical gravimetric hydrogen capacities are 5.71, 10.54, 7.84 and 9.27 wt%, respectively. However, all of them suffer from the disadvantage of too high desorption temperature, irreversible reaction, or low technical hydrogen capacity [Che01].

2.3 $LiNH_2$+LiH System Literature Review

2.3.1 Background and Reactions

Different from other metal hydrides or complex hydrides, the Li–N–H system is composed of both metallic and non-metallic elements in which the storage process involves the breaking and forming of the non-metal hydrogen bonds [Mic10]. Chen et al. [Che02] were the first to describe it. In fact, this discovery was important not only for practical reasons of hydrogen storage; it was also revolutionary in the solid-state hydrogen storage field. But it also brings many challenges. Despite good reversibility and an acceptable hydrogen capacity (about 6.5 wt%), the system is restricted by high desorption temperatures and low reaction kinetics [Nay11]. The whole process is represented by the following reaction:

$$\mathbf{Li_3N + 2H_2 \leftrightarrow LiNH_2 + 2LiH} \qquad \textbf{Equation 2.6}$$

with: Δ H=-96.3 kJ/mol H_2 [Ich04]

Theoretically, 10.4 wt% of hydrogen can be reversibly stored in this reaction. Ichikawa et al. [Ich04] claimed that the reaction in Equation 2.6 includes in fact two steps:

$$\mathbf{Li_3N + H_2 \leftrightarrow Li_2NH + LiH} \qquad \textbf{Equation 2.7}$$

with: Δ H=- 165 kJ/mol H_2

and

$$\mathbf{Li_2NH + H_2 \leftrightarrow LiNH_2 + LiH} \qquad \textbf{Equation 2.8}$$

with: Δ H=-45 kJ/mol H_2 [Var10a]

So in some literatures [Son06], Equation 2.6 is described as:

$$\mathbf{Li_3N + 2H_2 \leftrightarrow Li_2NH + LiH + H_2 \leftrightarrow LiNH_2 + 2LiH} \qquad \textbf{Equation 2.9}$$

If the two back reactions steps (desorption) shown in Equation 2.9 could both be realized, Li_3N can theoretically absorb approx. 10 wt% hydrogen [Hu05]. However, its reversible hydrogen capacity is only about 6.5 wt% because only a fraction of the hydrogen absorbed can be desorbed at relatively low temperatures.

First reported by Hu and Ruckenstein [Hu03] and Ichikawa et al. [Ich04], it is now well accepted that the reaction shown in Equation 2.8 can be further separated into two reaction steps [Var11, Yao07]:

$$\mathbf{2LiNH_2 \rightarrow Li_2NH + NH_3} \qquad \textbf{Equation 2.10}$$

$$\mathbf{NH_3 + LiH \rightarrow LiNH_2 + H_2} \qquad \textbf{Equation 2.11}$$

Because the two latter reactions shown in Equation 2.10 and Equation 2.11 are endothermic and exothermic respectively, the hydrogen desorption occurs as soon as $LiNH_2$ has decomposed into Li_2NH and NH_3 [Ich04a].

2.3.2 Possible Activation Methods

In Chen et al.'s report [Che02], several kinds of additives have been used with the Li-N-H hydrogen storage materials in order to improve them. One of the first reports about catalytic effects was from Isobe, Ichikawa, and their colleagues in Japan [Iso05, Ich05a]. They had used Ti (nanoparticles), Ti (microparticles), $TiCl_3$, TiO_2 (nanoparticles), TiO_2 (microparticles) [Iso05], or $TiCl_3$, VCl_3, and Fe, Co, and Ni nanoparticles with sizes of several tens of nanometers [Ich05a] as additives.

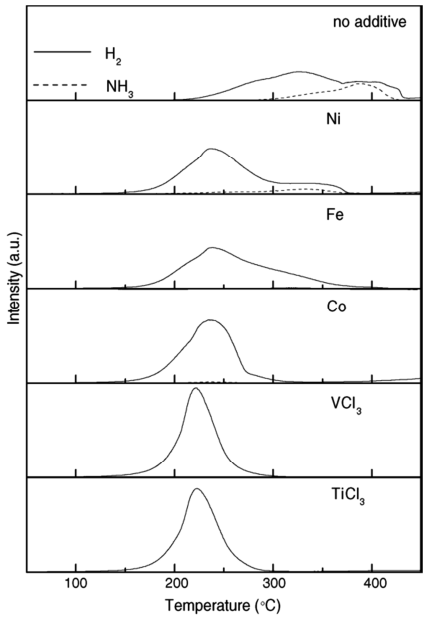

Figure 2.8: Thermal desorption profiles of H_2 and NH_3 of the ball milled mixtures of 1:1 $LiNH_2$ and LiH, in which a small amount (1 mol%) of nanometer sized Ni, Fe and Co, micro size VCl_3 and $TiCl_3$ were added respectively before milling [Ich05a]

Both reports cited suggest that $TiCl_3$ improves the hydrogen desorption properties. Fig 2.8 shows the comparison of $TiCl_3$ and other additives. The reversibility of the sample with $TiCl_3$ did not change after 3 cycles [Ich05a]. Besides $TiCl_3$, Ti^{nano} and $TiO_2{}^{nano}$ also showed good catalytic effects in contrast to Ti^{micro} and $TiO_2{}^{micro}$, which did not improve the results compared to the reaction without additives [Iso05]. Later, Hino et al. [Hin07] studied the catalytic effect of $TiCl_3$ in more detail. They found that with 1 mol% $TiCl_3$, the NH_3 to H_2 ratio was on the magnitude of 0.1% in the high-temperature range of 300-400°C.

In the study from Yao et al. [Yao07], chemical additions such as Mn, V, MnO_2 and V_2O_5 were investigated. The results showed that Mn, V and their oxides could promote the thermal decomposition of $LiNH_2$, but had no significant effect on the hydrogen desorption of the $LiNH_2$ + LiH mixture. Different from most the other studies [Hu03, Mar06], they think that the rate limiting step for dehydrogenation from $LiNH_2$ + LiH is the reaction between LiH and NH_3.

Varin and Yang [Var11] studied the effects of graphite on the reversible storage of hydrogen in the $LiNH_2$ + LiH system. However, there was no measurable effect of graphite as additive on the thermodynamic properties.

Apart from chemical additions, other methods have been used to improve the $LiNH_2$+LiH hydrogen storage system. The most widely used is the ball milling method. So far, in most studies, the samples were milled with steel balls at room temperature [Ich05a, Yao06, Var11]. However, Osborn et al. [Osb09] performed ball milling at -20°C, -40°C, and -196°C. The results got with the ball milled samples at -40°C and -20°C were similar, but the -196°C powders exhibited largely increased hydrogen desorption kinetics. Varin et al. studied the influence of the milling time [Var10a]. They found after high-energy ball milling of a 1:1 molar ratio of $LiNH_2$+LiH that the grain sizes of $LiNH_2$ and LiH constituents decreased monotonically with increasing milling time. The specific surface area (SSA) of the powders increased up to 25 h of milling duration and then decreased again after milling for 100 hours due to the larger agglomerations.

In order to enhance contact between LiH and $LiNH_2$, Yao et al. [Yao07] selected a molar ratio of 1:1.2 for the $LiNH_2$ + LiH mixture with a slight excess of LiH. Later, Varin investigated the influence of the molar ratio of $LiNH_2$ and LiH [Var10a]. They prepared mixtures with three different molar ratios of $LiNH_2$ and LiH: 1:1.0, 1:1.2, and 1:1.4. After ball milling, the lowest activation energy was observed for a molar ratio of 1:1.2.

2.3.3 Modeling Study

Shaw et al. [Sha08a] developed a model for the rate-limiting step in the $LiNH_2$-LiH hydrogen storage system. As it is well accepted that the reaction between LiH and Li_2NH is much faster than the desorption reaction of $LiNH_2$ particles [Hu03, Mar06], the total reaction is dictated by the first reaction. Only the rate of each step in Equation 2.10 needs to be investigated in order to identify the rate-limiting step of the whole desorption reaction.

The model built by Shaw et al. [Sha08a] was calculated from the Pilling-Bedworth (P-B) ratio [Pil23] which is helpful to explain the porosity of the oxide scale and its adhesion to the metal during metal oxidation.

P-B ratio= V_o/V_m **Equation 2.12**

with: V_o: Volume of the oxide scale

V_m: Volume of the metal

If the P-B ratio is less than 1, the shell tends to be porous. When the P-B ratio is between 1 and 2, the oxide shell can fully cover the metal surface, however, with compressive stress. When the P-B ratio is larger than 2, the oxide shell often cracks and detaches due to the high compressive stress in the shell [Pil23]. Based on the data shown in Table 2.3, the P-B ratio for $LiNH_2$ is 0.5 and for LiH is 2.0. Therefore, the shell around $LiNH_2$ particles is porous and that around LiH particles tends to flake off, as shown in Figure 2.9.

Table 2.3: Molar volume of the chemicals in the $LiNH_2$-LiH system

	$LiNH_2$	**Li_2NH**	**LiH**
Molar volume [cm^3mol^{-1}]	19.44 [Sha08a]	19.51 [Sha08a]	9.7 [Sha08a]

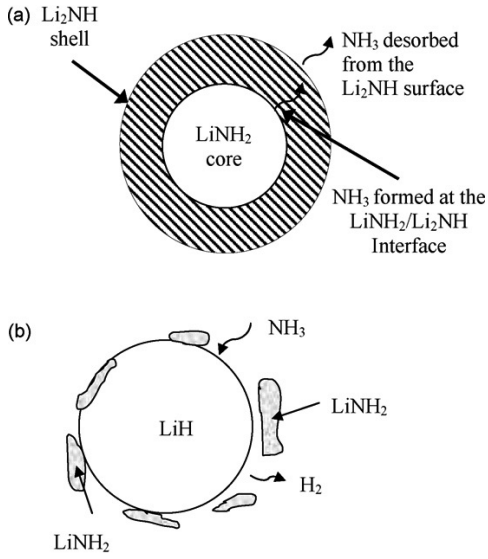

Figure 2.9: Schematic of the hydrogen release pathway of the $LiNH_2$- LiH system: (a) the Li_2NH product from Equation 2.10 forms a continuous shell outside the $LiNH_2$ shrinking core, leading to a reaction rate controlled by NH_3 diffusion through the Li_2NH product layer, and (b) the $LiNH_2$ product from Equation 2.11 flakes off continuously, resulting in a direct reaction between NH_3 and the constantly regenerated new LiH surface [Sha08a]

It is important to determine the rate-limiting step of the desorption reaction of the $LiNH_2$ + LiH mixture. Based on the model given above, Equation 2.10 can be divided into 3 steps:

Step 1: Decomposition of $LiNH_2$ to Li_2NH and NH_3 at the $LiNH_2/Li_2NH$ interface.

Step 2: Diffusion of NH_3 through the porous Li_2NH product layer from $LiNH_2/Li_2NH$ interface to the Li_2NH surface.

Step 3: Desorption of NH_3 from the Li_2NH surface.

As described by Shaw et al. [Sha08a], if the rate of the desorption reaction of $LiNH_2$ particles is controlled by Step 1, it can be described by two models, the Johnson-Mehl-Avrami (JMA) model and the contracting volume (CV) model. The JMA model describes the nucleation of randomly dispersed second-phase particles independent from their location [Min94]. It can be written as:

$$f = 1 - \exp(-k_1 t^3)$$ **Equation 2.13**

with f: the fraction of H2 released

t: time

k1 related factor

In the CV model, nucleation starts from the surface of the existing particles and then continues to grow towards the core moving the $LiNH_2/Li_2NH$ interface at a constant speed. This relation is found to have the following formula [Din01]:

$$(1 - f)^{\frac{1}{3}} = 1 - \frac{k_2}{R} t$$ **Equation 2.14**

with: k_2: related factor

R: gas constant

However, if the rate is controlled by Step 2, then the fraction of H_2 released will follow a parabolic-rate law derived from Fick's second law with the following formula [Mar06]:

$$(1 - f)^{\frac{1}{3}} = 1 - \frac{k_3^{1/2}}{R} t^{1/2}$$ **Equation 2.15**

with: k_3: related factor

Finally, if the rate is controlled by Step 3, i.e., desorption of NH_3 into the surrounding atmosphere assuming a constant pressure, the fraction of H_2 released will exhibit a linear relationship between f and t [Tho97], as expressed by:

$$f = k_4 R^2 t$$ **Equation 2.16**

with: k_4: related factor

It has been found that [Sha08a] the experimental data of Shaw et al. could be better fitted by the diffusion-controlled model far better than by the moving-boundary-controlled and the NH_3-desorption-controlled model. Because of this reason, they gave the conclusion that the diffusion is the rate limiting step in the desorption process of $LiNH_2$+LiH material.

2.4 $LiNH_2$ + MgH_2 Systems

Just when investigations of the Li-N-H hydrogen storage system began, Li–Mg–N–H systems were studied independently by Luo [Luo04], Leng et al. [Len04], and Y. Nakamori and Orimo [Nak04] at almost the same time. $LiNH_2$+MgH_2 [Luo04, Lu07] or $Mg(NH_2)_2$+LiH [Len04, Xio05] were used as starting material. The reaction mechanism of the Li-Mg-N-H hydrogen storage system is complicated and different molecular ratios between Li and Mg can be found in the literature. Some typical ratios are Mg:Li= 1:2 [Luo04, Jan07], Mg:Li= 1:1, Mg:Li= 3:8 [Len04] and Mg:Li= 1:4[Nak04]. Two of these systems will be described as examples.

2.4.1 $2LiNH_2$+ MgH_2

For the ($2LiNH_2$+MgH_2) system, the hydrogen exchange reactions have been described as follows [Sha08, Che05]:

$$\mathbf{2LiNH_2 + MgH_2 \rightarrow Li_2NH + MgNH \leftrightarrow Mg(NH_2)_2 + 2LiH} \qquad \textbf{Equation 2.17}$$

Or:

$$\mathbf{2LiNH_2 + MgH_2 \rightarrow Li_2MgN_2H_2 + 2H_2 \leftrightarrow Mg(NH_2)_2 + 2LiH} \qquad \textbf{Equation 2.18}$$

The reversible reactions appear to take place between $Li_2MgN_2H_2$+$2H_2$ and $Mg(NH_2)_2$ +2LiH. It is suggested that $Mg(NH_2)_2$+2LiH is either thermodynamically or kinetically more favourable than $2LiNH_2$+MgH_2. Some reports said that $Mg(NH_2)_2$ can also be formed by long-time ball milling (over 15 hours).

With the desorption temperature set as 200°C, the absorption temperature as 220°C and 125°C and the pressure was 110 atm, the hydrogen uptake capacity was about 4 wt% within 3 hours for material milled for 5 hours [Che05, Pot10], while samples that were ball milled for 45 hours took up about 4.3 wt% of hydrogen within 2 hours [Che05].

2.4.2 $LiNH_2$+ MgH_2

Apart from $LiNH_2$+LiH system, there are also some literatures focusing on the $LiNH_2$+ MgH_2 system [Akb07]:

$$\mathbf{LiNH_2 + MgH_2 \rightarrow LiMgN + 2H_2} \qquad \textbf{Equation 2.19}$$

This reaction yields theoretically 8.2 wt% of H_2. Simulations based on first principle calculations of total and vibrational free energy suggest that the reaction between $LiNH_2$ and MgH_2 (molar ratio 1:1) would take place according to the following steps which are given by [Lu09]:

$$\mathbf{LiNH_2 + MgH_2 \rightarrow \frac{1}{2}Mg(NH_2)_2 + LiH + \frac{1}{2}MgH_2 \rightarrow LiH + \frac{1}{4}Mg(NH_2)_2 + \frac{1}{4}Mg_3N_2 + H_2 \rightarrow \frac{1}{2}LiH + \frac{1}{4}Li_2MgN_2H_2 + \frac{1}{4}Mg_3N_2 + \frac{3}{2}H_2 \rightarrow LiMgN + 2H_2} \qquad \textbf{Equation 2.20}$$

Experiments yielded 6.1 wt% hydrogen releases for the 1:1 ratio system after ball milling and subsequent heat treatment [Lu09]. $Mg(NH_2)_2$ and LiH could be formed during high-energy ball milling.

2.5 Methods to Characterize Gas Sorption Ability

2.5.1 Volumetric Techniques

The volumetric method is the most common of the measurement techniques to investigate the gas sorption ability of a sample. It can be implemented using a gas handling system of known volume in which temperature and pressure can be measured exactly. The amount of gas absorbed or desorbed by a sample can be calculated using the ideal gas law:

$$\mathbf{pV = nRT} \qquad \textbf{Equation 2.21}$$

with: p: pressure

V: volume

n: number of moles

R: gas constant

T: temperature

A schematic diagram of a typical manometric sorption measurement system is shown in Figure 2.10. The sample to be studied is filled in the volume V_2, V_2 is connected with the volume V_1 which has a defined volume. The pressure in V_1 is measured using a manometer. Valve A and Valve B in Figure 2.10 control the experimental gas (for example: hydrogen) to go in and out. In addition to the hydrogen inlet valve, there might be other admission valves, for example, to flush the system before and after the measurement with inert gas.

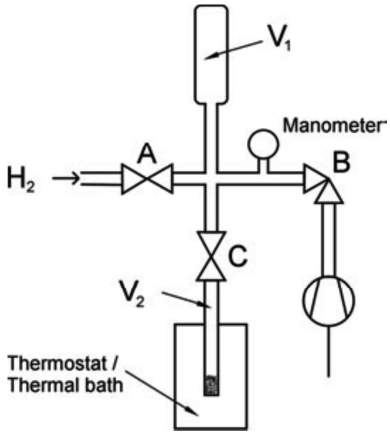

Figure 2.10: A schematic diagram of a typical manometric sorption measurement system [Bro08]

From Figure 2.10 and Equation 2.21, the amount of desorbed gas *n* at temperature *T* can be derived as:

$$\mathbf{n} = \frac{\mathbf{P}(\mathbf{V_1}+V_2-V_s)}{\mathbf{RT_r}} + \frac{\mathbf{PV_s}}{\mathbf{RT_S}} \qquad \textbf{Equation 2.22}$$

with: T_r: temperature in Volume V_1

T_s: sample temperature

P: pressure measured at the manometer

R: gas constant

V_s: volume with experimental temperature

The problem of Equation 2.22 is that the volume V_s is difficult to define. There are also temperature gradients between the sample temperature (T_s) and temperature in V_1 which have to be considered. The difference between Equation 2.21 and Equation 2.22 comes from the temperature difference. The temperature in V_1 is close to room temperature. However, the experimental temperature of the sample is always at several hundred degrees Celsius. Compared to V_1 and the rest volume in V_2, the heating volume of the sample is small and can be neglected.

2.5.1.2 Flowing volumetric method

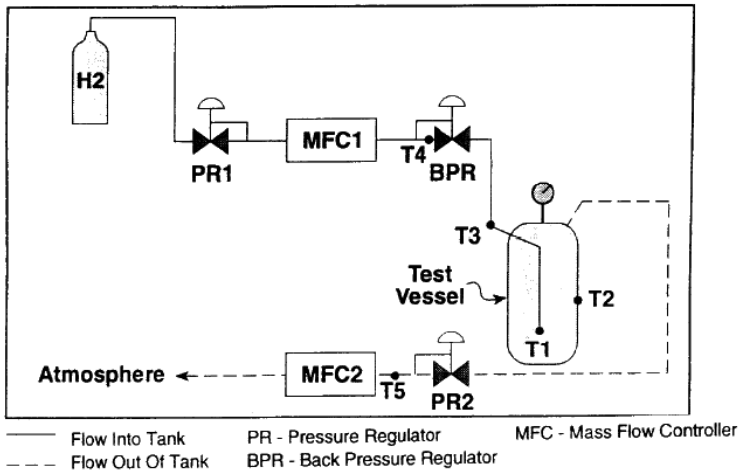

Figure 2.11: Simplified scheme of the flowing volumetric method [Hyn96]

Figure 2.11 shows a simplified example of the major parts used for the flowing volumetric method. The amount of hydrogen desorbed or absorbed by a sample is determined by measuring the flow rate of hydrogen into the sample cell with a mass flow controller (MFC). In order to measure both the mass flow into and out of the test vessel, two separate mass flow controllers with corresponding pressure regulators are required. When used at isobaric conditions, the resulting flow rate should be integrated as a function of time. The integral of the total mass flow signal gives the total absorbed quantity. However, from Figure 2.11 it can be seen that the system is more complicated than the manometric method. The integral calculation of inward and outward flow is not trivial and gives a limitation of this method.

2.5.2 Gravimetric Techniques

Gravimetric analysis requires weighing the solids obtained from a sample by evaporation, filtration or precipitation [Dav02]. Gravimetric techniques were originally applied to measure the adsorption of gases and vapors to carrier materials. In recent times this method has been used effectively to study the gas absorption/desorption performance of hydrogen storage

material [Bro11a]. A typical gravimetric hydrogen sorption measurement system is built with the following parts: a balance with a high precision, a vacuum system for evacuation and sample degassing, a gas supply system that can control the hydrogen pressure in the balance chamber and an electrical heater or a thermostat to control the sample temperature during experiments. After the sample is adhered to the balance, the system should be evacuated. The measurement is performed under the desired gas atmosphere (hydrogen, inert gas or vacuum) and defined temperature programs. After corrections, the measured weights can be plotted as a function of pressure or temperature.

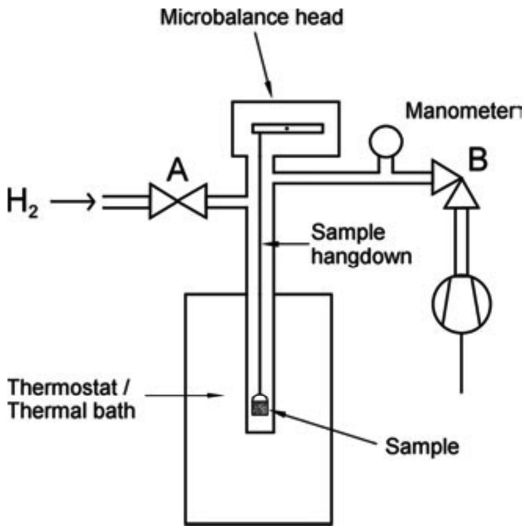

Figure 2.12: A schematic diagram of a basic gravimetric sorption measurement system [Bro08]

A schematic diagram of a basic gravimetric system is shown in Figure 2.12. Valves A and B control the hydrogen gas inlet and vacuum outlet, respectively. They can control the hydrogen pressure in the sample chamber. A magnetic suspension balance in which the balance mechanism is isolated from the sample chamber can also be applied. The thermostat, electrical heater or even liquid nitrogen can be used as temperature-controlling unit, if necessary. Depending on the required hydrogen pressure ranges, there can be one or more pressure measuring devices in the system. The vacuum pump can be of any type, although an oil-free

system with UHV capability is preferable, particularly if samples are to be degassed. For microporous materials high vacuum is essential and thus a turbo molecular pump backed by a membrane or scroll pump is recommended. For the experiment with hydrogen storage material, the hydrogen supply should be of very high purity, so the system must be well evacuated before an experiment starts.

2.6 Thermodynamic Calculations

2.6.1 Calculation of Activation Energy

The activation energy is defined as the energy that must be overcome in order for a chemical reaction to occur. It can be assumed as the height of a potential barrier, separating the potential energies of the reactants and the products. It is an important factor to assess whether a reaction is easy to happen or not. In order to estimate whether a hydrogen storage system absorbs or desorbs hydrogen easily, it is a significant parameter.

Model free methods are most reliable to calculate the activation energy [Sta03]. Examples are the Friedman method, Kissinger-Akahira-Sunose (KAS) method [Aka71], Flynn-Wall-Ozawa (FWO) method [Oza65] and Kissinger method [Kis57]. In the following, the background of these methods will be introduced.

In a reaction, the transformed fraction α is usually used to study the reaction kinetics [Ven11]:

$$\alpha = \frac{m_0 - m_t}{m_0 - m_\infty} \qquad \textbf{Equation 2.23}$$

with: m_0: initial mass

m_t: mass at time t

m_∞: mass at the end of the reaction

Many references use the simplifying assumption that the transformation rate during a reaction is the product of two functions: *k(T)*, only depending on the temperature *T*, and *f(α)* only depending on the transformed fraction α [Sta03]. So :

$$\frac{d\alpha}{dt} = f(\alpha)k(T) \qquad \textbf{Equation 2.24}$$

The temperature dependent function is always assumed to follow an Arrhenius type dependency [Sta03]:

$$\mathbf{k(T) = k_0 exp(-\frac{E}{RT})}$$ **Equation 2.25**

with: E: activation energy

T: temperature

k_0: reaction constant

The Kissinger method [Kis57] is also called the modified Kissinger`s equation or peak-displacement method [Bos79]. It is a maximum rate method. In this method, it is assumed that the equivalent stage is the stage at which the maximum rate of transformation is achieved [Sta03]. This should be the differential thermo gravimetric (DTG) peak during the experiment. If the sample has a good contact with the sample holder, this peak position should be equated to the differential thermal analysis (DTA) peak position.

The function f(α) in Equation 2.24 depends on the particular decomposition mechanism. The simplest and most frequently used model for f(α) in the analysis of thermo gravimetric analysis (TGA) data:

$$\boldsymbol{f(\alpha) = (1-\alpha)^n}$$ **Equation 2.26**

with: n: order of reaction.

Inserting Equation 2.26 into Equation 2.24, results in:

$$\boldsymbol{\frac{d\alpha}{dt} = \beta \frac{d\alpha}{dT} = (1-\alpha)^n k(T) = k_0 (1-\alpha)^n \exp\left(-\frac{E}{RT}\right)}$$ **Equation 2.27**

with: ß: Heating rate

At T_{max} the reaction rate is maximum and thus:

$$\boldsymbol{\frac{d(\frac{d\alpha}{dt})}{dt} = 0}$$ **Equation 2.28**

So, with Equation 2.27 and Equation 2.28, result in:

$$\boldsymbol{\frac{\beta}{T_{max}^2} = \frac{AR}{E} n(1-\alpha_{max})^{n-1} exp(-\frac{E}{RT_{max}})}$$ **Equation 2.29**

with: A: constant

Taking the logarithm on both sides of Equation 2.29, results in:

$$\ln\left(\frac{\beta}{T^2_{max}}\right) = \ln\left(\frac{AR}{E}\right) + \ln(n(1-\alpha_{max})^{n-1}) - \frac{E}{RT_{max}}$$ **[Yan03] Equation 2.30**

The activation energy can thus be determined from a plot $\ln(\beta/T_{max}^2)$ against $1/T_{max}$.

2.6.2 Van't Hoff Equation

The Van't Hoff equation [Hof00] also known as the Vukancic-Vukovic equation in chemical thermodynamics relates the change in temperature T to the change in the equilibrium constant k, yielding the standard enthalpy change for the process. Therefore, this equation can be used to calculate the standard enthalpy change of a reaction process.

It is derived as follows:

The Gibbs free energy Δ G is defined as:

$$\Delta G = \Delta H - T\Delta S$$ **Equation 2.31**

with: ΔH: enthalpy of reaction

ΔS: entropy of reaction

T: temperature

or in the case of an isothermal reaction as:

$$\Delta G = -RT \ln k$$ **Equation 2.32**

with: k: the equilibrium factor

Inserting Equation 2.32 into Equation 2.31, results in:

$$\ln k = -\frac{\Delta G}{RT} = -\frac{\Delta H}{RT} + \frac{\Delta S}{R}$$ **Equation 2.33**

With: R: gas constant

for an example reaction:

$$\mathbf{aA + bB \rightarrow cC + dD} \qquad \textbf{Equation 2.34}$$

with: A, B: reactants

C, D: products

a ,b ,c, d: coefficients of the reactants and products

The equilibrium factor k is:

$$\mathbf{k = \frac{\alpha_C^c * \alpha_D^d}{\alpha_A^a * \alpha_B^b}} \qquad \textbf{Equation 2.35}$$

Where α is the activity of the coefficients or products. For the solid phase, α is considered as 1, however, for the gas phase, α equals P/P_0, with P being the gas partial pressure, and P_0 is the standard pressure (1 atm).

Applying Equation 2.35 to our hydrogen storage system:

$$\mathbf{LiNH_2 + LiH \rightarrow Li_2NH + H_2 \uparrow} \qquad \textbf{Equation 2.36}$$

yields k as:

$$\mathbf{k = \frac{\alpha_{H_2}^1 * \alpha_{Li_2NH}^1}{\alpha_{LiNH_2}^1 * \alpha_{LiH}^1} = \frac{\alpha_{H_2} * 1}{1 * 1} = \alpha_{H_2} = \frac{P_{H_2}}{P_0}} \qquad \textbf{Equation 2.37}$$

Combining Equation 2.37 with Equation 2.33 results in:

$$\mathbf{\ln\left(\frac{P_{H_2}}{P_0}\right) = -\frac{\Delta H}{RT} + \frac{\Delta S}{R}} \qquad \textbf{Equation 2.38}$$

So, with a plot of ln (P_{H2} /P_0) versus 1/T, the reaction enthalpy can be calculated.

3 Material and Methods

3.1 Material Handling

As the samples to be studied were sensitive to air, all storage and handling was done in the BRAUN UNlab Glovebox workstation (M. Braun Inertgas-Systeme GmbH, Germany) shown in Figure 3.1 under inert gas conditions.

Figure 3.1: BRAUN UNlab glovebox workstation

The main part of the glovebox is built of stainless steel with a large scratch-resistant polycarbonate window in front. The atmosphere inside the glovebox is argon. The leakage rate of the whole system was smaller than 0.05 vol% per hour. In order to keep the organic solvent vapor components in the glovebox low, a reservoir of activated carbon (5 kg) was connected to the glovebox. The system was also installed with oxygen and moisture analyzers for a purity level < 1 ppm. With the help of redundant filter columns, the inside oxygen and moisture could be maintained at ultralow levels (less than 1 ppm).

3.2 Sample Preparation

Lithium amide ($LiNH_2$, purity 95%) and lithium hydride (LiH, purity 98%) were purchased as powders from Sigma-Aldrich Chemie GmbH. Tetrahydrofuran (THF, purity 99.5%) was purchased from Acros Organics. The addtitives (BN and $TiCl_4$) were purchased from Sigma-Aldrich Chemie GmbH. All samples were stored and handled in the glovebox.

The specific surface area (SSA) is one of the most important properties of hydrogen storage materials. Accordingly, hydrogen storage materials with larger specific surface areas have better desorption properties. In order to reduce the particle size of the raw material, a planetary ball milling method was used in this study. Figure 3.2 shows the inside of the milling machine (Planetary Ball Mill PM 400, RETSCH GmbH. Germany)

Figure 3.2: Planetary Ball Mill PM 400 milling machine

Planetary milling processes in this study were performed with four milling containers. One is shown in Figure 3.3(a). The milling containers were made from stainless steel. After the containers were filled with sample powder and the yttrium stabilized zirconia (YSZ) milling balls in the glovebox, each of them was sealed with 8 nuts and bolts together with an O-ring and set

into the milling machine. During the milling process, the containers rotated around the central axis and simultaneously around their own axes in opposite direction - like the planets rotate around the sun. The sample particles underwent multiple collisions with the grinding media and the jar walls. High velocity of moving milling bodies made high stress on the activated materials.

In most studies described in the literature, steel balls were chosen as milling media [Ich05a, Yao06, Var11]. However, in this study YSZ ceramic balls (Tosoh Corporation, Japan) were used. The YSZ milling media (Figure 3.3b) are of high density and provide a great impact force resulting in superior grinding efficiency. Compared to steel milling media, YSZ balls are more resistant to corrosion. They provided best results when used in wet grinding with dispersions.

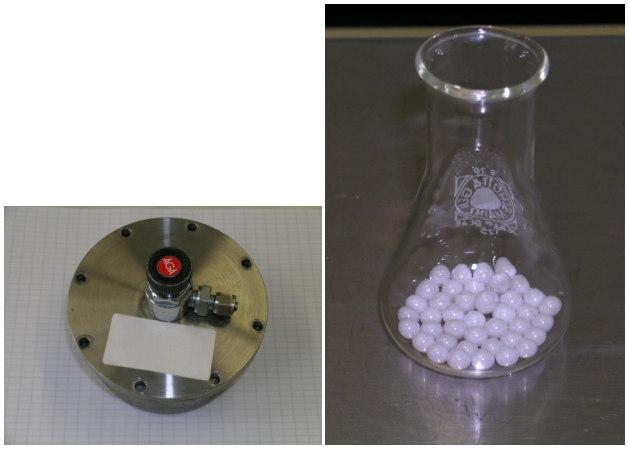

(a) (b)

Figure 3.3: (a) Ball milling container; (b) YSZ milling balls (diameter: 5 mm)

The ball to sample weight ratio in this study was set to 10:1, which means that per 5 g sample powder 50 g YSZ milling media was added.

Milling was performed as wet ball or dry ball process. Meng [Men10] has referred that tetrahydrofuran (THF) as a part of milling media works good to reduce the sample particle sizes. So in this study for wet ball samples THF was added. The weight ratio between THF and the

sample material was 4:1. This resulted in a mixture of 20 g THF and 50 g milling balls per 5 g sample powder.

The diameter of the milling balls shown in Figure 3.3 was 5 mm. But most samples in this study were milled by a mixture of milling balls of different diameters. The weight ratio between 5 mm milling balls and 2 mm milling balls was 7:3, for example. The idea behind this approach was to destroy the large particles by the strong impact of the large milling balls and, at the same time, destroy the small particles into even smaller ones by the smaller milling balls. In some cases, the milled samples were milled a second time with very fine milling balls (diameter: 0.1 mm).

After milling, the dry ball milled samples were transferred back to the glovebox, taken out and stored there directly. The wet ball milled material have to be stored in the glovebox for about 20 hours in order to dry them from THF.

3.3 Sample Characterization

3.3.1 XRD Method

Phase composition and microstructure of the sample powders were analyzed by X-ray diffraction (XRD) with a Bruker D4 ENDEAVOUR diffractometer (Bruker AXS GmbH, Karlsruhe) which is shown in Figure 3.5a.

3.3.1.1 Bragg Condition

During XRD analysis, X-rays are reflected by atoms in the crystal lattice to be analyzed. Figure 3.4 shows the principle of diffraction: the spacing between reflecting planes in the crystal is d and the scattering angle of the X-rays is θ. The incoming beam is scattered by the atoms in each plane. The path difference for waves reflected by successive planes is 2d*sin θ. If the path difference for successive plane is an integer multiple of the incoming wavelengths, the diffracted waves will combine to produce a strong diffracted beam. Hence the condition for diffraction (the Bragg condition) is [Bra13]:

$$n\lambda = 2d \sin\theta \qquad \text{Equation 3.1}$$

with: n: integer

λ: wavelength of the incoming x-rays.

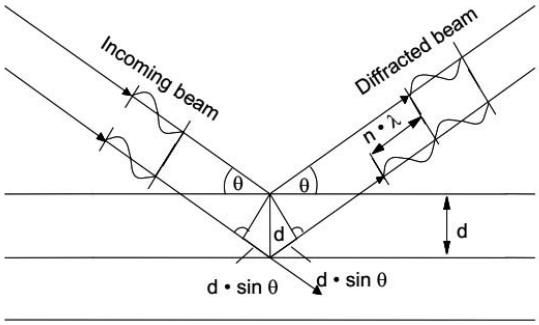

Figure 3.4: Schematic illustration of the diffraction of X-rays in a crystalline material. Bragg's law is fulfilled if the path length difference between the X-rays is equal to nλ

The Bragg condition is suitable for any set of planes whose spacing is greater than half the wavelength of the used X-rays. This condition sets a limit on how many orders of diffracted waves can be obtained.

The resulting XRD pattern is obtained by measuring the intensity of scattered waves as a function of the scattering angle. The intensities are plotted against 2θ and show characteristic patterns for each investigated phase. Very strong intensities known as Bragg peaks are obtained in the diffraction pattern when the scattered waves satisfy the Bragg condition. The resulting patterns are analyzed with the help of software HighScore Plus (PANalytical B.V., Almelo, Netherlands).

As the samples in this study were sensitive to air, a special sample holder to separate the sample from air was necessary (cf. Figure 3.5b). The sample was prepared in the glovebox and sealed with an O-ring. During the whole XRD procedure, the inner atmosphere in the sample holder was Ar.

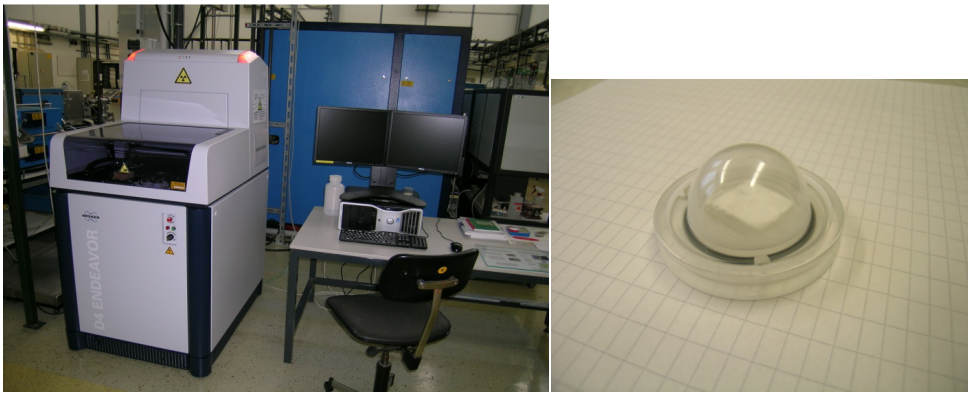

(a) (b)

Figure 3.5: (a): Bruker D4 ENDEAVOUR diffractometer; (b): XRD sample holder for air-sensitive samples

3.3.1.2 Williamson-Hall Method

The Williamson-Hall method was invented by G. K. Williamson and his student, W. H. Hall [Wil53] in the year 1953. It is a method to estimate crystallite sizes and strains with the peak width information from the XRD measurement. In general, the peak broadening contains contributions from both crystallite size and strain. The simplification of Williamson and Hall is to assume that the convolution is a simple sum:

$$\beta\,(\text{sample}) = \beta\,(\text{size}) + \beta\,(\text{strain}) \qquad \textbf{Equation 3.2}$$

with: ß: lattice strain

According to the Scherrer equation [Sch18], the crystallite size contributes as:

$$\beta(\text{Size}) = \frac{\lambda}{D\cos\theta} \qquad \textbf{Equation 3.3}$$

with: D: mean size of the ordered (crystalline) domains

λ: X-ray wavelength

θ: Bragg angle.

and the contribution from strain is

$$\beta(\mathbf{strain}) = 4\varepsilon \tan\theta \qquad \textbf{Equation 3.4}$$

with: ε: lattice strain

Inserting Equation 3.3 and Equation 3.4 into Equation 3.2 yields

$$\beta = \frac{\lambda}{D\cos\theta} + 4\varepsilon \tan\theta \qquad \textbf{Equation 3.5}$$

Multiplied with cosθ results in

$$\beta \cos\theta = \frac{\lambda}{D} + 4\varepsilon \sin\theta \qquad \textbf{Equation 3.6}$$

Plotting β cosθ versus sinθ, the crystallite size can be derived from the y-intercept of the fitted line and the strain can be estimated from its slope.

3.3.2 DTA-TG-MS

3.3.2.1 DTA and TGA

Differential thermal analysis (DTA) is a thermoanalytical technique. During heating and cooling, physical and chemical changes are taking place such as melting, solidification, crystal transformation, decomposition, chemical combination, absorption, and desorption. These changes will cause enthalpy changes of the system, resulting in thermal effects. In a DTA measurement, the material to be analyzed and a reference material are undergoing identical thermal cycles. Any temperature differences between the sample and the reference are plotted against time or temperature.

A DTA system consists of a sample holder comprising thermocouples, sample containers, a furnace, and a recording system. There are two thermocouples connected to a voltmeter. One thermocouple is placed in an empty Al_2O_3 sample container, while the other one is placed in a sample of the material to be studied. As the temperature is increased, there will be a deflection of the voltmeter if the sample is undergoing a phase transition. The input heat will raise the

temperature of the neutral reference substance to keep it at the same temperature as the sample under analysis.

Thermogravimetric analysis (TGA) is based on three measurements: weight, temperature and time. A derivative weight loss curve can be used to tell the point at which weight loss is most apparent.

3.3.2.2 Quadrupole Mass Spectrometry (QMS)

Mass spectrometry (MS) is an analytical technique that measures the mass-to-charge ratio of charged particles. It is used to determine masses of particles, the elemental composition of a sample or molecule, and to elucidate the chemical structure of molecules [Chh07]. The quadrupole mass analyzer consists of four parallel metal rods, each rod pair connected electrically. A radiofrequency voltage is applied between one pair of rods and the other. A direct current voltage is added to the RF voltage. Ions travel down the quadrupole between the rods. Only ions of a certain mass-to-charge ratio (m/z) will reach the detector for a given ratio of voltages. Other ions have unstable trajectories and will collide with the rods. This permits selection of an ion with a particular m/z or allows the operator to scan for a range of m/z-values by continuously varying the applied voltage.

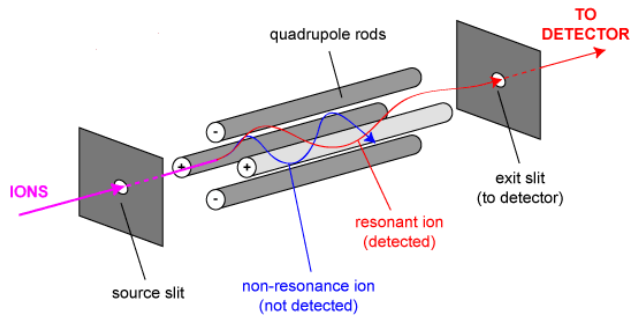

Figure 3.6: Schematic of a quadrupole analyzer [Bri10]

Mass spectrometers, composed of a mass filter, an electron impact ion source and ion detector, work only in high vacuum. Therefore, an interface is required for coupling of a thermo balance to the mass spectrometer, which works with a purge gas flow at atmospheric pressure.

Figure 3.7: QMS 403 AëolosTM quadrupole mass spectrometer (right) connected with the DTA-TG device (left)

(a) **(b)**

Figure 3.8: Glass bottles for (a): Al_2O_3 crucible with sample and (b): SEM sample holder transfer

In this study, the desorbed gases during the DTA measurements were analyzed with a QMS 403 Aëolos^{TM} quadrupole mass spectrometer (Figure 3.7). It is a new compact mass spectrometer with a heated capillary inlet system for routine analysis of gases and, especially for volatile

decomposition products of thermal analysis. This system has been optimized for coupling to differential scanning calorimeters and thermo gravimetric analyzers. The measurements are carried out at the same time and the test conditions are identical for TG, DTA, and MS signals alike.

3.3.3 Scanning Electron Microscopy (SEM)

In this study, the morphology of the sample powders were imaged with an SEM (Zeiss, Microscopy GmbH, Oberkochen, Germany).

The first step of sample preparation was done in the glovebox. The electrically conductive carbon tapes were adhered onto pin stubs. Then, the powders were scattered onto the electrically conductive carbon tapes and slightly pressed with a glass slide in order to get better conductivity. After that, the pin stubs were put into the same type of glass bottle used for DTA analysis (Figure 3.8a) and transferred to the SEM.

3.3.4 Specific Surface Area According to BET

In this study, the specific surface areas of the prepared powders were determined by using the Areameter II instrument, which is shown in Figure 3.9 (Ströhlein Instruments, Germany). The measuring principle is based on the so-called BET method, introduced by Brunauer, Emmett and Teller in 1938 [Bru38].

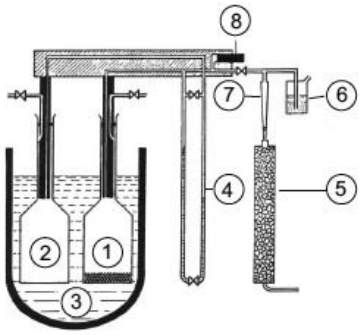

1 specimen cup
2 reference cup
3 cold bath (water or liquid nitrogen)
4 differential pressure manometer
5 drying column
6 over pressure vessel
7 flow meter
8 buffer volume

Figure 3.9: Areameter II from Ströhlein Instrument

The concept is an extension of the Langmuir theory. It is a theory for monolayer molecular adsorption to multilayer adsorption with the following hypotheses:

1. Gas molecules physically adsorb on a solid in layers infinitely;

2. There is no interaction between each adsorption layer;

3. The Langmuir theory can be applied to each layer.

The resulting BET equation is expressed by Equation 3.7:

$$\frac{1}{v\left[\left(\frac{P_0}{P}\right)-1\right]} = \frac{c-1}{v_m c}\left(\frac{P}{P_0}\right) + \frac{1}{v_m c} \qquad \textbf{Equation 3.7}$$

with: P: equilibrium pressure

P_0: saturation pressure

v: adsorbed gas quantity

v_m: monolayer adsorbed gas quantity

c: BET constant (related to the enthalpy of adsorption and condensation of the adsorbed gas)

$$c = \exp\left(\frac{E_1 - E_L}{RT}\right) \qquad \textbf{Equation 3.8}$$

with: E_1: the heat of adsorption for the first layer

E_L: the heat of adsorption for the second hand higher layers

A straight line 1/v [(P_0/P)-1] vs. P/P_0 can be plotted with Equation 3.7, This plot is called a BET plot. v_m can be calculated. With Equation 3.9, the specific surface area (SSA) can be determined.

$$S_{BET} = \frac{\upsilon_m N s}{V a}$$

Equation 3.9

with: N: Avogadro's number

s: adsorption cross section of the adsorbing species

V: molar volume of adsorbed gas

a: mass of adsorbent

3.4 Sorption Test and Characterization

As introduced in Chapter 2.5, mainly two kinds of methods are used for sorption measurements: the volumetric and the gravimetric method. In this study, both methods were used. The systems applied will be described in detail:

3.4.1 Belsorp-HP

The Belsorp-HP (BEL INC, Japan) shown in Fig 3.10a is an automatic high-pressure gas adsorption system. In this study, it was used for the volumetric method to study desorption kinetics and equilibrium pressure of the samples. Depending on the selected temperature control devices, the experimental temperature can range from 77 K up to 673 K. With the appropriate software, adsorption and desorption isothermal measurements can be performed. High-pressure adsorption measurements can be done up to 13.5 MPa.

Figure 3.10b shows a diagram of the gas dosing system of the Belsorp-HP. AV1 controls the He inlet at a pressure of 0.15 MPa. AV2 controls the inlet of the absorption gas which was H_2 in this study. AV6 controls the connection between the sample holder and the gas dosing system. AV7 controls the connection between the pressure sensor P3 and the gas dosing system. It will be closed when the gas exceeds 127 kPa to protect P3. AV3-AV5 are used to decrease the pressure. AV4 should only be opened when the pressure is below 300 kPa. If AV5 is open, the pump produces the highest vacuum. This should be restricted to pressures below 10 kPa. The system can reach a vacuum of approx. $1.3*10^{-1}$ Pa. During the experiment, the value P1 will be recorded. A change of P1 indicates desorption or absorption of gas by the sample. The mass change of the sample can be calculated by applying the ideal gas law.

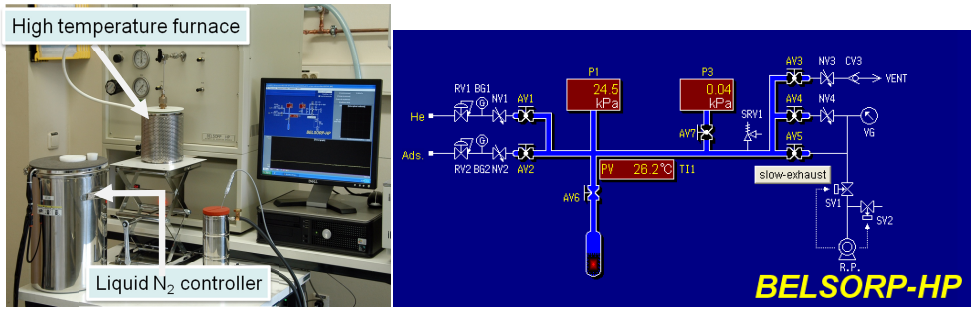

(a) **(b)**

Figure 3.10: (a): Belsorp-HP system; (b): software interface of Belsorp-HP

In order to know the initial temperature profile of the sample in the Beslorp-Hp system, the temperature profiles with different target temperature were measured and drawn in Figure 3.11. It can be seen that within the initial 30 min, the measured sample temperature was already almost equal to the target temperature. Samples could fully reach the target temperature in 60 min.

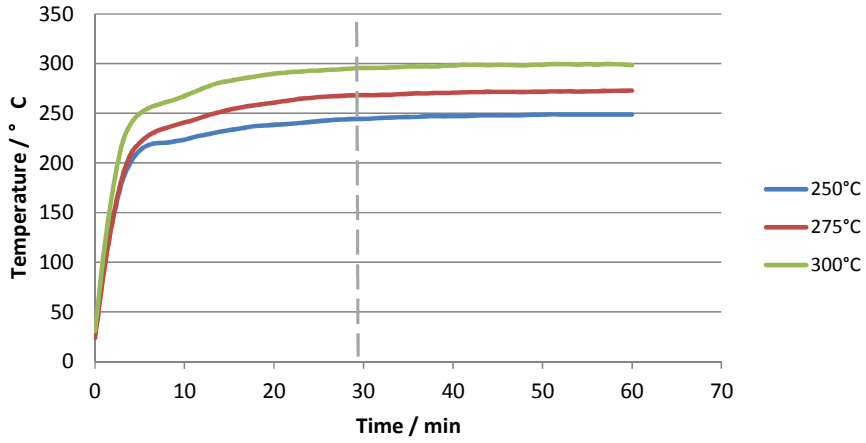

Figure 3.11: Measured temperature profile of the high temperature furnace used in Belsorp-Hp system (target temperature: 250°C, 275°C, and 300°C, respectively)

3.4.2 IsoSORP-MSB

IsoSORP-MSB (Rubotherm GmbH, Germany) is a gravimetric sorption analyzer with magnetic suspension balance. Other than the volumetric Belsorp-HP system, it can measure the mass change of the sample directly. It has the following components: magnetic suspension balance, gas dosing system, liquid nitrogen bottle, PC, and software. They are shown in Figure 3.12.

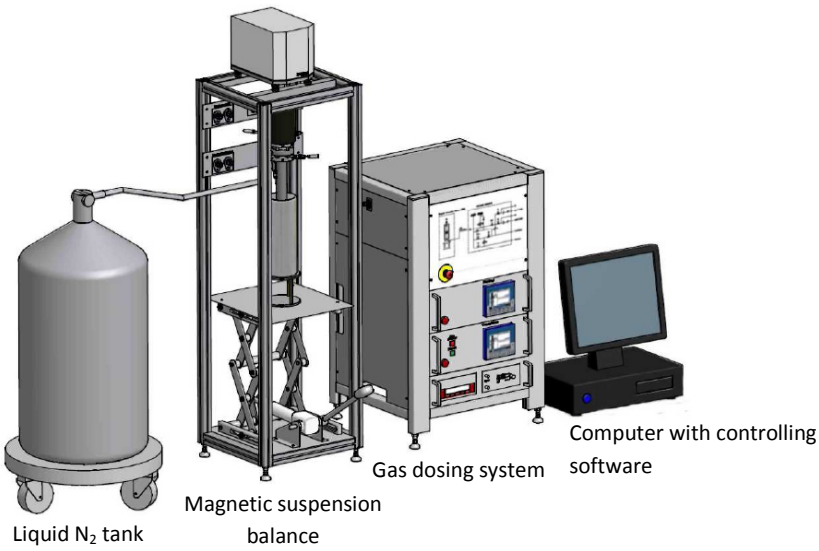

Figure 3.12: Sketch of the IsoSORP-MSB gas sorption analyzer [Rub10]

The magnetic suspension balance is the key part for the whole system. It allows to measure mass changes of the samples with high accuracy (10 µg for a load of up to 80 g) and under controlled environmental conditions (atmosphere, temperature and pressure).

The most interesting feature of the magnetic suspension balance is that it is possible to perform non-contact measurements. As shown in Figure 3.13, rather than hanging directly at the balance, the sample is linked to a so-called suspension magnet which consists of a permanent magnet, a sensor core, and a device for decoupling the measured load (sample). The electromagnet, which is attached to the weighing hook of the balance, maintains a freely

suspended state of the suspension magnet via an electronic control unit. Using this magnetic suspension coupling, the measuring force is transmitted without contact from the measuring chamber to the microbalance, which is located above the chamber under ambient atmospheric conditions.

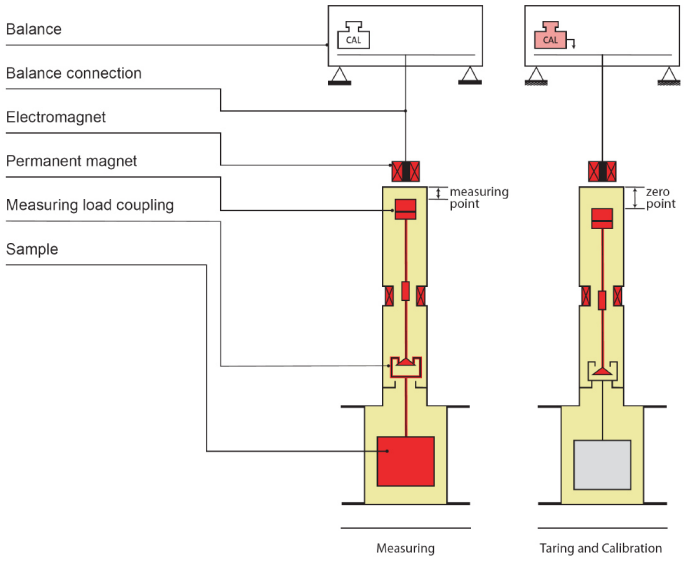

Figure 3.13: The measuring principle of a magnetic suspension balance [Rub10a]

As the samples in this study were air-sensitive, a special sample holder shown in Figure 3.14 was used. As described in Chapter 3.1, the sample preparation was done in a glovebox. The samples were put into the inner sample holder (see Figure 3.14b), which in turn was installed into the outer sample part and closed with the cover. After that, the inner atmosphere in the sample holder is inert gas and in this state the samples can be transferred from the glovebox to the magnetic suspension balance. Before closing the measuring cell, the whole system was flushed with inert gas for more than 5 min. During that time, the stick with 2 O-rings shown in Figure 3.14b can be removed.

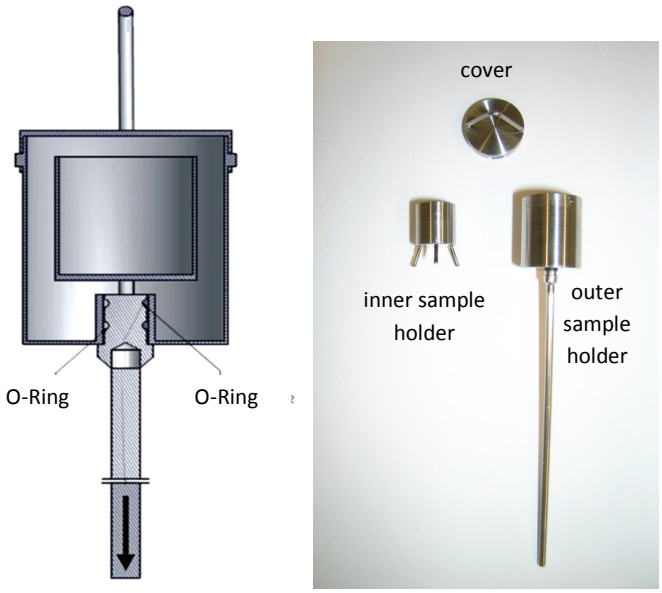

(a) (b)

Figure 3.14: Sample holder for the magnetic suspension balance of the IsoSORP-MSB (a): Schematic diagram of the internal structure; (b): photo of the 3 parts

4 Results and Discussion

4.1 $LiNH_2$ Single Component System

As described in chapter 2.4, the desorption process in the $LiNH_2$+LiH hydrogen storage system can be divided into two steps: In the first step $LiNH_2$ particles decompose and release NH_3. In the second step, NH_3 reacts with LiH particles while hydrogen is released. Because the $LiNH_2$ decomposition is the first step of the desorption process, the characteristics and desorption behavior of the $LiNH_2$ powders influence the system performance critically.

With the aim to perform a systematical study, this study was begun with the investigation of the first desorption step, using the $LiNH_2$ single component system. The $LiNH_2$ sample powders were activated with diverse ball milling processes for different milling periods. Three weight percent of boron nitride (BN) were used as additive in some of the experiments. Boron nitride was selected for two reasons. First, it has not been widely studied (in contrast to, for example, $TiCl_3$); second, it has already been shown that BN could improve the $LiNH_2$-LiH hydrogen storage system desorption kinetic [Agu07]. Table 4.1 shows the sample names and the corresponding preparation methods.

Table 4.1: $LiNH_2$ single component sample names and preparation methods

Sample name	Milling time / Hour	Dry/wet ball milled	Milling ball diameter / (Ratio)	BN Additive /wt%
LiNH2(as received)	_	_	_	_
LiNH2-3h-T	3	wet (with THF)	5 and 2 mm/ (7:3)	_
LiNH2-3h-D	3	dry	5 and 2 mm/ (7:3)	_
LiNH2-24h-D	24	dry	5 and 2 mm/ (7:3)	
LiNH2-72-T	72	wet (with THF)	5 and 2 mm/ (7:3)	_
LiNH2-72-D	72	dry	5 and 2 mm/ (7:3)	_
LiNH2-72-T-3BN	72	wet (with THF)	5 and 2 mm/ (7:3)	3
LiNH2-72-D-3BN	72	dry	5 and 2 mm/ (7:3)	3
LiNH2-72+24-T	1^{st} step: 72	wet (with THF)	1^{st} step: 5 and 2 mm/	_

	2^{nd} step: 24		(7:3) 2^{nd} step: 0.1 mm	
LiNH2-72+24-T-3BN	1^{st} step: 72 2^{nd} step: 24	wet (with THF)	1^{st} step: 5 and 2 mm/ (7:3) 2^{nd} step: 0.1 mm	3

4.1.1 Characteristics of Sample Powders

4.1.1.1 Microstructure Study Using Scanning Electron Microscopy (SEM)

Figures 4.1-4.4 display SEM images of $LiNH_2$ as received (Figure 4.1) and after different treatment procedures (Figure 4.2-4.4). The SEM samples were prepared by scattering the powders onto carbon tape followed by pressing with a glass plate in order to get better conductivity.

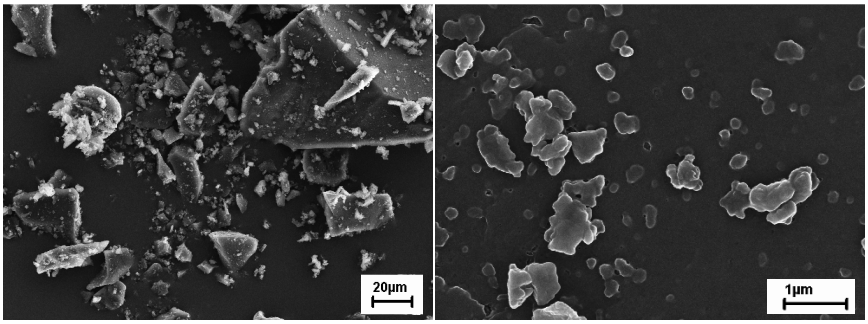

(a) **(b)**

Figure 4.1 :SEM images of $LiNH_2$ (as received)

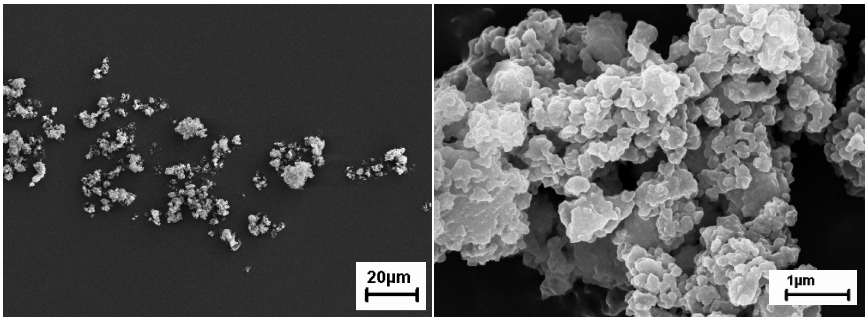

(a) **(b)**

Figure 4.2: SEM images of as milled sample: $LiNH_2$-3h-D

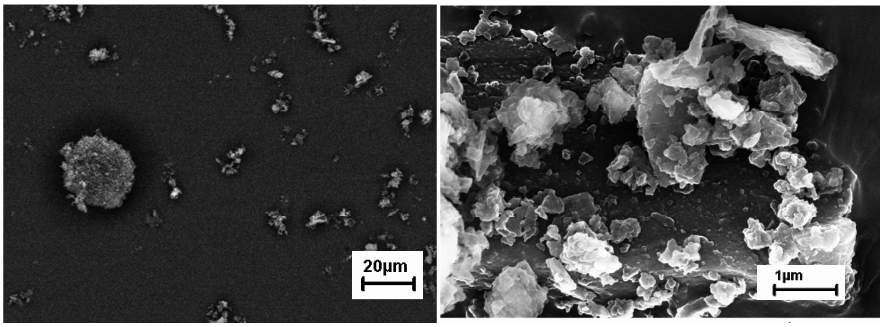

(a) **(b)**

Figure 4.3: SEM images of as milled sample: $LiNH_2$-3h-T

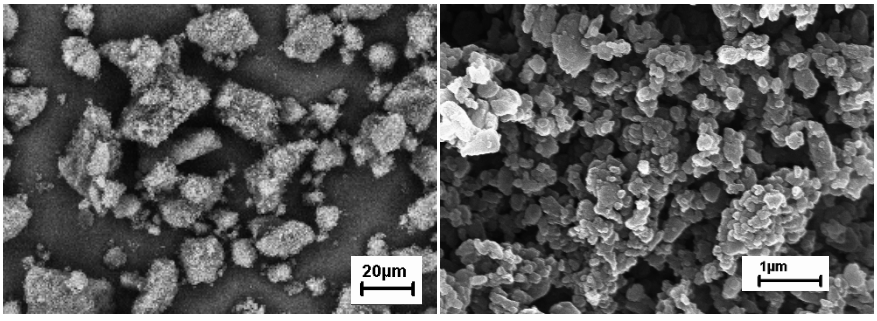

(a) **(b)**

Figure 4.4: SEM images of as milled sample $LiNH_2$-72-T

The resulted Particles of the as-received $LiNH_2$ powder came in various shapes and sizes (cf. Figure 4.1a). The surface of a bigger particle can be seen in Figure 4.1b. It was almost smooth. Some finer particles of 0.2-1 µm adhered to the surface of the bigger ones. Figure 4.2 and Figure 4.3 show that after three hours ball milling, the average particle sizes were significantly lower than in the as-received powders. Figure 4.2 (b) and Figure 4.3 (b) show the particles with larger magnification. In contrast to the smooth surface of the as-received material, the surfaces of the ball milled particles looked different. The fine particles formed agglomerates with relatively rough surfaces. After three hours wet ball milling, still large crystalline particles could be found. However, after 72 hours wet ball milling process (cf. Figure 4.4) the particle sizes were significantly smaller than the samples after three hours wet treatment.

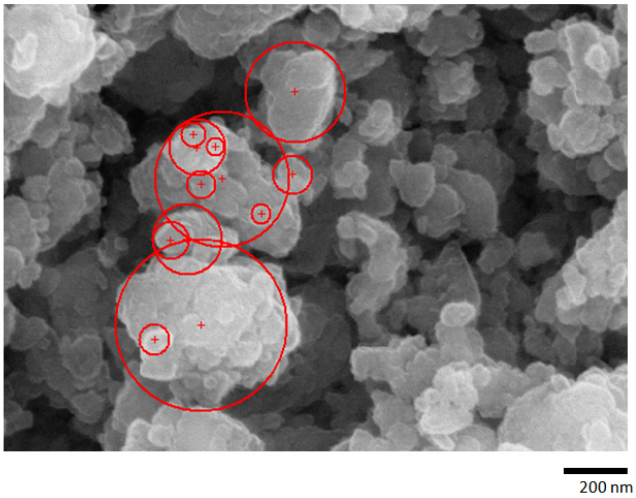

Figure 4.5: An example picture of particle size analysis with software AnalysisPro (Sample: LiNH2-72-T)

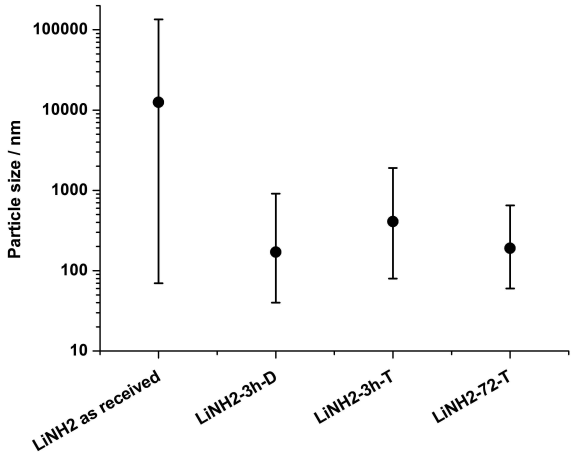

Figure 4.6: Particle sizes of the $LiNH_2$ as received and as milled samples

In order to quantify the particle sizes of the samples, the software Analysis Pro (Iter)was used to analyse the SEM images. For each sample, 100 particles were chosen randomly from 2-3 different SEM images. An example is shown in Figure 4.5. In this example twelve particles in the same region were measured (marked with red circles). The mathematical average values of the particle sizes were calculated by the software AnalysisPro and are illustrated in Figure 4.6. The bars in Figure 4.6 are not error bars but presenting the particle size distribution interval of the 100 particles under analysis.

For the as received sample, the particle sizes were in a range of about 80 nm to 100 µm with a mean value above 10 µm. After ball milling processes, the particle sizes of all the samples were significantly reduced. Corresponding to the SEM images in Figure 4.2(b) and Figure 4.3(b), particles with large size can be found in the 3 hours wet ball milled sample which led to a larger average particle size of the $LiNH_2$wet ball milled sample compared with the dry ball milled sample. A possible reason could be reduced friction and impact force acting on the sample due to the role of lubrication that THF plays. Increasing the milling time (72 h) leads clearly to a further reduction of the particle size (cf. Fig 4.6).

4.1.1.2 Microstructure Study Using X-ray Diffraction (XRD)

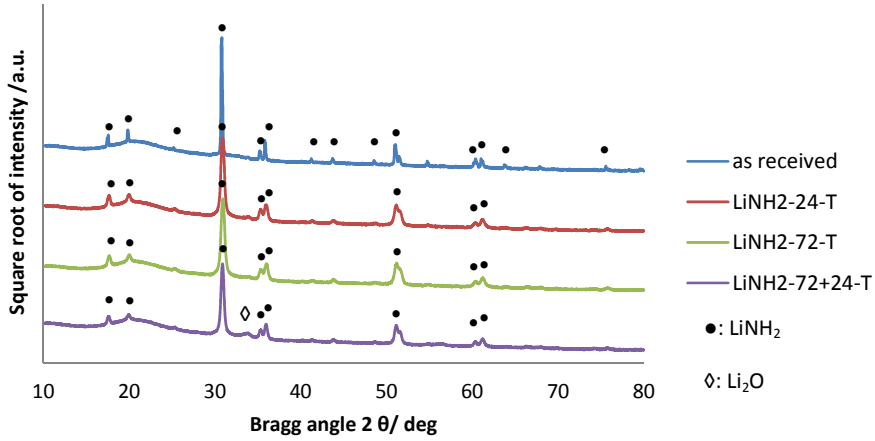

Figure 4.7: Comparison of the XRD patterns of $LiNH_2$ samples with different wet ball milling time periods

Figure 4.7 illustrates the XRD diagrams from an as-received sample and samples with different wet ball milling time periods. Except for sample LiNH2-72+24-T, there is no evidence for Li_2O in the samples. The small peak at about 2θ≈33° in sample LiNH2-72+24-T corresponds to the main peak position of Li_2O. The reason why this sample got slightly oxidized is explicable. First, it had a larger specific surface area which makes it higher tendency to get oxidation. Second, this sample was milled twice, in order to get the powder out of the suspension liquid with the fine milling balls (diameter: 0.1 mm), a waiting time of 24 hours was necessary for the milling balls to settle down to the bottom of the beaker. This long time period facilitated oxidation.

$LiNH_2$ exhibits several double peaks (2θ= 34.889° and 2θ= 35.619°, 2θ= 50.717° and 2θ= 51.260°, 2θ= 60.837° and 2θ= 60.970°). They could clearly be observed in the XRD pattern of the as-received sample. In the XRD patterns of all the ball milled samples, the peaks tend to be broader and all of the double peaks fuse into a single peak. This difference can be explained by a larger crystallite size of the wet ball milled samples. Based on the XRD pattern data of the samples, the crystallite size and strain had been calculated using the Williamson-Hall method. The results are shown in Figure 4.8. Compared to the as-received sample, all the wet ball milling

processes had led to a decrease in the crystallite size of the samples (cf. Fig 4.8a). As the milling time increased, the resulting sample crystallite size (cf. Fig 4.8a) and strain (cf. Fig 4.8b) increased, as well.

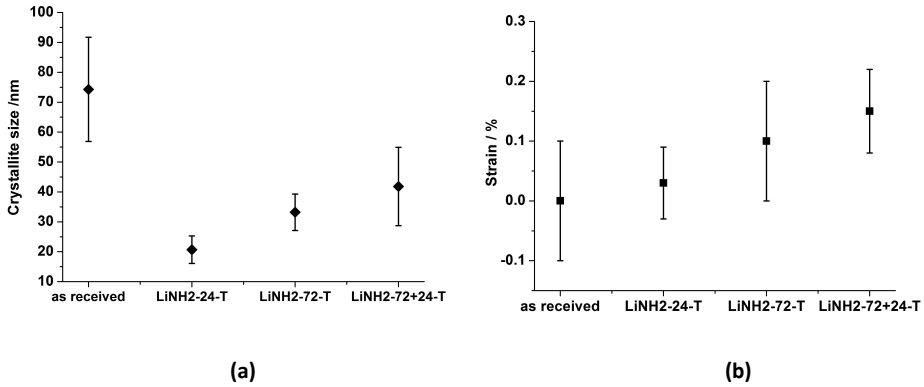

Figure 4.8: Comparison of (a) crystallite size and (b) lattice strain of $LiNH_2$ samples with different wet ball milling time periods (calculated with Williamson-Hall method)

A comparison of the XRD patterns of dry and wet ball milled $LiNH_2$ samples (cf. Fig 4.9) revealed, in general, no phase change for dry and wet ball milled samples. The XRD pattern of LiNH2-72-D exhibited a weak peak at around $2\theta \approx 33°$ which can be attributed to Li_2O. However, this peak could not be found in the wet ball milled material with the same process time. Other results were similar for wet and dry ball milled $LiNH_2$+LiH samples (see below). In general, the wet ball milled samples tended to be less easily oxidizable than dry ball milled material. Th possible reason for that may be the THF covered the $LiNH_2$ particles during the milling process and prevented them from oxidation.

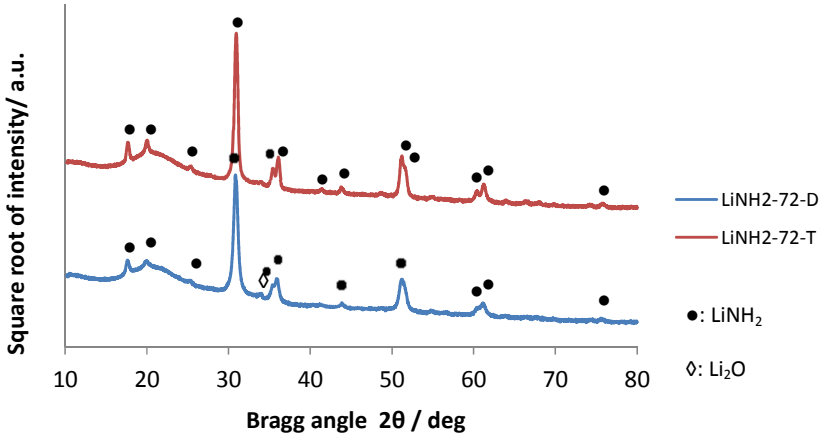

Figure 4.9: Comparison of the XRD patterns of dry and wet ball milled $LiNH_2$ samples

The size of the crystallites was calculated with Williamson-Hall plot based on the width of the peaks at different positions. The calculated results shown in Figure 4.10a illustrate that the wet ball milling produced larger crystallites than that dry ball milling after the same treatment time. The underlying mechanism for that phenomenon may be that THF acted as lubrication. The friction and impact force acted on the $LiNH_2$ sample particles were then reduced in the case of wet ball milling process. This assumption was supported by the calculated lattice strain values (cf. Fig 4.10b) which show that the dry ball milling process resulted in larger lattice strain than that of the wet ball milling process.

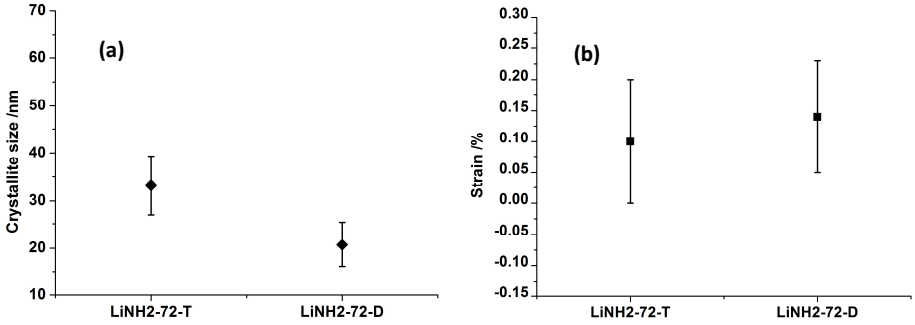

Figure 4.10: Comparison of (a) crystallite size and (b) lattice strain between dry and wet ball milled $LiNH_2$ samples

Figure 4.11 shows the comparison of the XRD patterns between the sample LiNH2-72-T and LiNH2-72-T-3BN. XRD patterns of the sample with BN as additive did not show clear phase differences from the sample without BN (cf. Fig 4.9). Just a minor additional peak at 2θ=26.8° could be discerned.

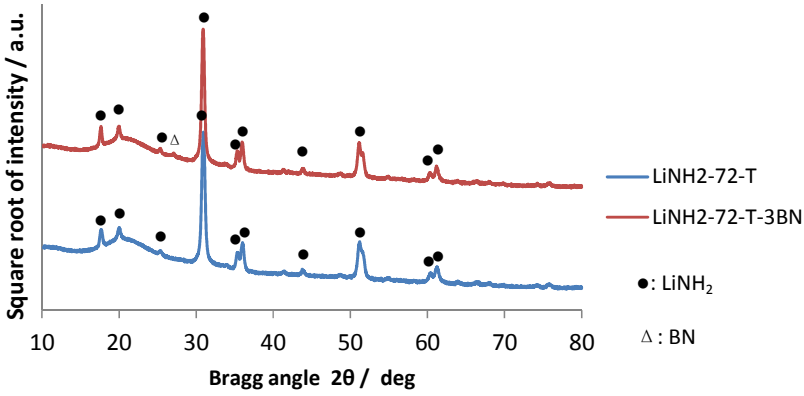

Figure 4.11: Comparison of the XRD patterns between wet ball milled $LiNH_2$ samples with and without BN additive

It can be seen in Figure 4.12 that this three percent by weight BN did not influence the crystallite size or the lattice strain of the sample clearly.

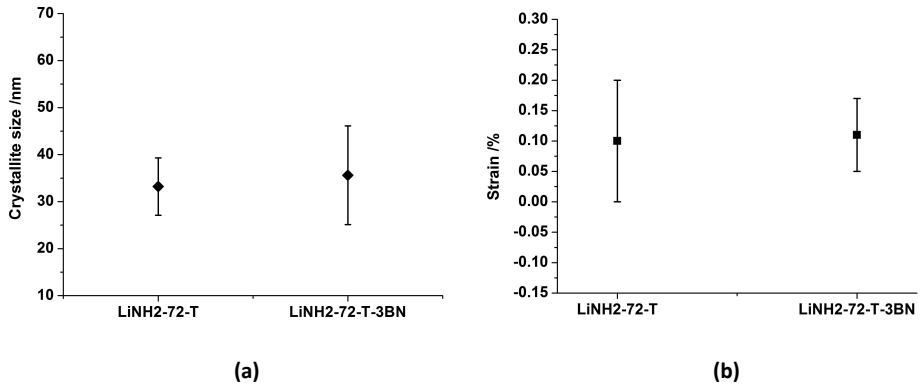

Figure 4.12: Comparison of (a) crystallite size and (b) lattice strain between samples with and without BN as additive

4.1.1.3 BET Results

The specific surface area is a very important parameter to evaluate a hydrogen storage system [Zue03]. To increase it is always a development target. The desorption of $LiNH_2$ is an important step of the $LiNH_2$-LiH system. In this study, the specific surface area of the $LiNH_2$ powders were measured using the BET method and the results are shown in Figure 4.13.

All ball milling processes were successful in increasing the specific surface area of the sample powders (28 - 119 m^2/g) as compared to that of the as-received material (2 m^2/g). A longer ball milling time led to higher specific surface areas of the sample powders. But the addition of 3 wt% of BN did not significantly influence the specific surface areas. The results of samples LiNH2-72-T (60 m^2/g) and LiNH2-72+24-T (119 m^2/g) demonstrate that an additional 24-hour fine-ball milling process can clearly improve the specific surface area of the $LiNH_2$ powder further.

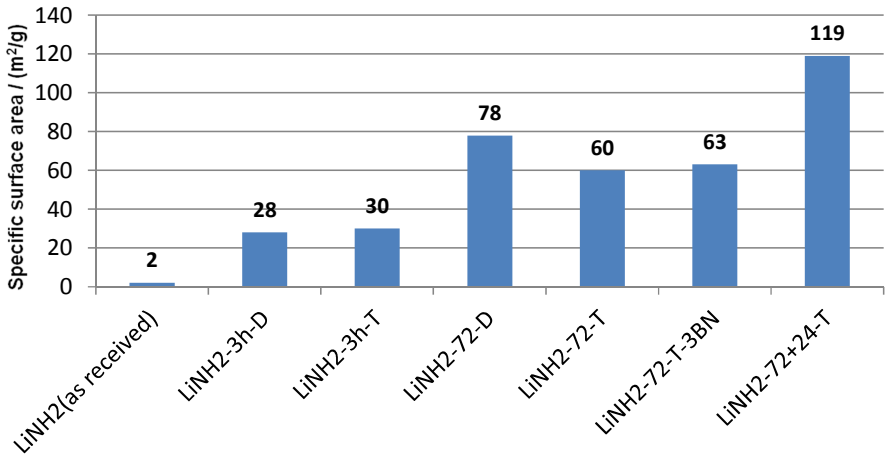

Figure 4.13: Specific surface area of $LiNH_2$ sample powders measured by the BET method

4.1.2 Sorption Behavior

Figure 4.14 displays the desorption results obtained from the IsoSORP-MSB system (magnetic suspension balance). A $LiNH_2$ as-received sample and a sample milled dry for 3 hours (LiNH2-3-D) were heated from 50°C up to 380°C at a rate of 2 K/min. Different from the experiment with the Belsorp-HP, the pressure during the entire experiment was well controlled at vacuum condition. This should help to desorb the hydrogen more efficiently.

The curves in Figure 4.11 indicate that within the same experiment condition the desorption reaction with $LiNH_2$ as received sample began much later (around 250°C) than that of the sample after 3 hours dry ball milling (around 100°C). However, the total weight losses of both samples were very similar.

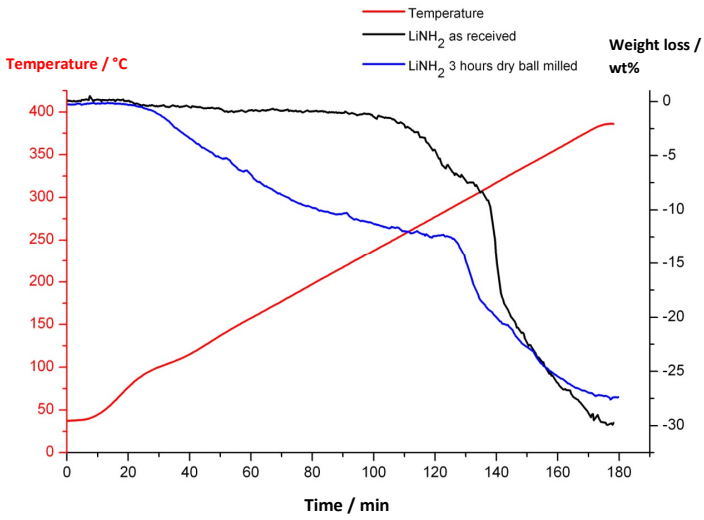

Figure 4.14: Comparison of desorption behavior between a $LiNH_2$ as-received sample and a 3-hour dry ball milled sample (IsoSORP-MSB)

As discussed before (see chapter 3.4.1), the Belsorp-HP is a closed system. The graph in Figure 4.15 illustrates slow desorption kinetics for all the samples. The maximum weight loss of $LiNH_2$ is, theoretically, 36.9 %. With the Belsorp-HP system, only around 1.5-2.5 wt% weight loss could be achieved within 550 min. This was nearly independent of the specific surface area, as indicated by the desorption curves of samples LiNH2-72+24 (119 m^2/g) and LiNH2-72-T (60 m^2/g), where the specific surface areas differed by a factor of 2. The sample with 3 wt% BN (LiNH2-72-T-3BN) tended to have faster desorption kinetics at the beginning.

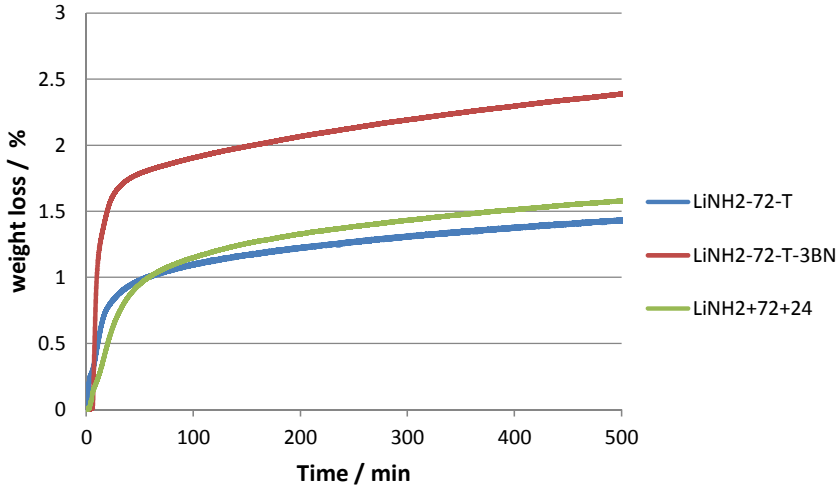

Figure 4.15: Sample desorption at 300°C in the Belsorp-HP system

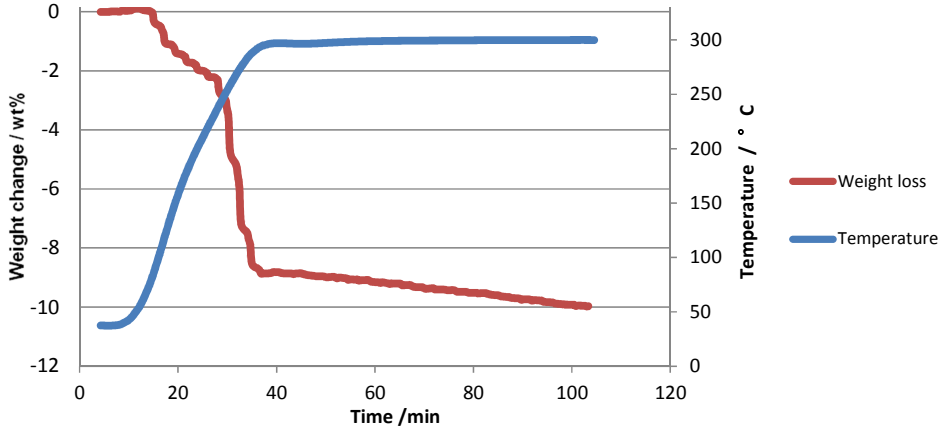

Figure 4.16: LiNH2-72-T desorption at 300°C in the magnetic suspension balance system

Figure 4.16 shows the desorption profile of sample LiNH2-72-T at 300°C with the magnetic suspension balance. The desorption temperature was same as that used in Figure 4.15. The pressure of the system was kept at vacuum level. It is obvious that the weight loss measured with the IsoSORP-MSB system reached already 10% within 100 minutes and hence was much

higher than the result obtained with the Belsorp-HP system shown in (500 min, 1.5 wt%). This was a general phenomenon. The NH_3 partial pressure stops probably the desorption of $LiNH_2$ particles very effectively and the low pressure in the IsoSORP-MSB system supports the forward reaction of the gaseous desorption.

4.1.3 Thermodynamic Calculations

In order to better understand the thermodynamic decomposition behavior of $LiNH_2$, DTA-TG-MS analyses were performed with samples LiNH2-72-T and LiNH2-72-T-3BN. The samples were heated from 50 to 400°C at rates of 1, 2, and 5 K/min, respectively.

As introduced in chapter 2.6.1, the maximum rate of transmission, which corresponds to the differential thermo-gravimetric (DTG) peak, could be used to calculate the activation energy. The DTG peak temperature was taken as described by Varin et al [Var11]. In case of good contact with the sample holder, the DTG peak position should be equal to the DTA peak position. As only thermo-gravimetric analysis (TGA) and Differential Thermal Analysis (DTA) data were available in this study, the DTG peak first had to be derived from the TGA data.

As shown in Figure 4.17, with the TGA experimental result of sample LiNH2-72-T-3BN (heating rate: 1 K/min), the DTG profile was calculated and drawn as blue line. Then the DTA and DTG peak positions were compared. As can be seen, both peak positions almost coincide. That means the maximum mass changing point match the maximum heat changing position. The same result was obtained for other LiNH2-72-T-3BN samples with different heating rates. Therefore, it seemed permissible to take the DTA peak data for further calculations.

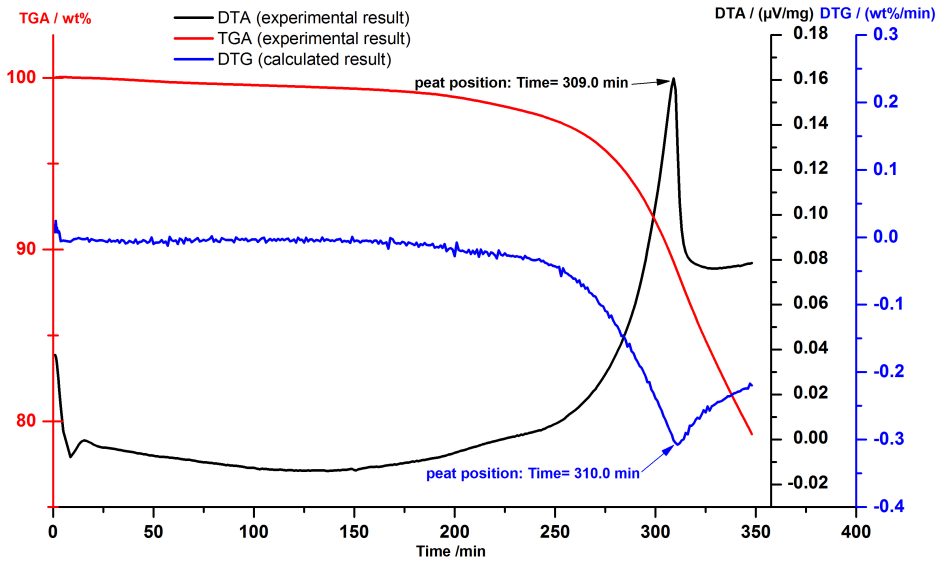

Figure 4.17: **Comparison of measured DTA and calculated DTG positions in the result obtained with sample LiNH2-72-T-3BN (heating rate: 1 K/min)**

All DTA/TGA experiments of the $LiNH_2$ samples revealed one clear endothermic peak in the temperature range between 350°C and 400°C(cf. Figure 4.18 and Figure 4.19), which is in agreement with published data from Varin and Yang [Var11]. With different heating rates, different DTA peak temperatures were obtained as shown in Figure 4.18 and Figure 4.19.

Based on the peak temperatures and heating rates, the activation energies of the LiNH2-72-T and LiNH2-72-T-3BN samples were calculated using the Kissinger method (see Chapter: 2.6.1). The corresponding linear fits are shown in Figure 4.20 and Figure 4.21, respectively. The resulting activation energies were 321.8±33.2 kJ/mol NH_3 and 260.2±18.0 kJ/mol NH_3, respectively. Both R square values (the square of the linear regression coefficient) were better than 0.95, which means that the calculated result should be reliable. The results suggest that the addition of BN can lower the activation energy of the $LiNH_2$ decomposition reaction.

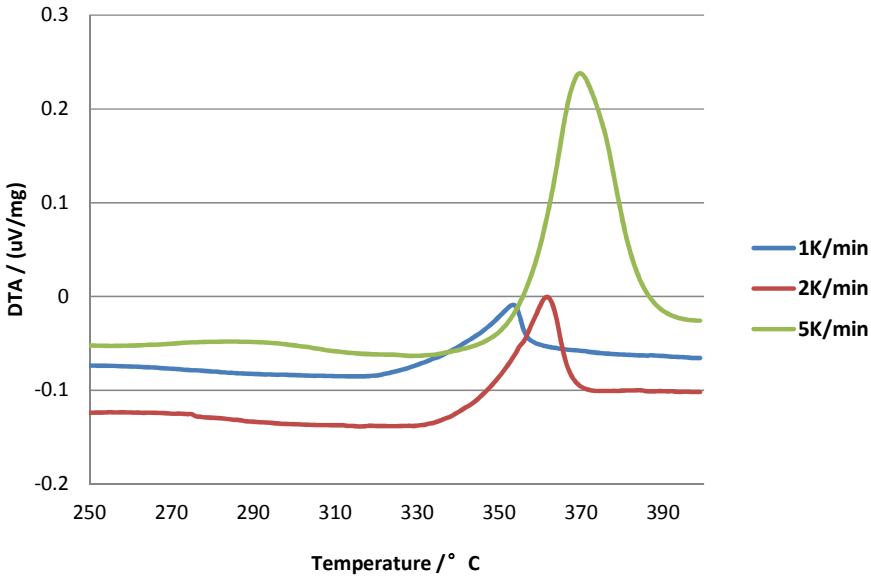

Figure 4.18: DTA results of $LiNH_2$-72-T, heating rate: 1 K/min, 2 K/min and 5 K/min

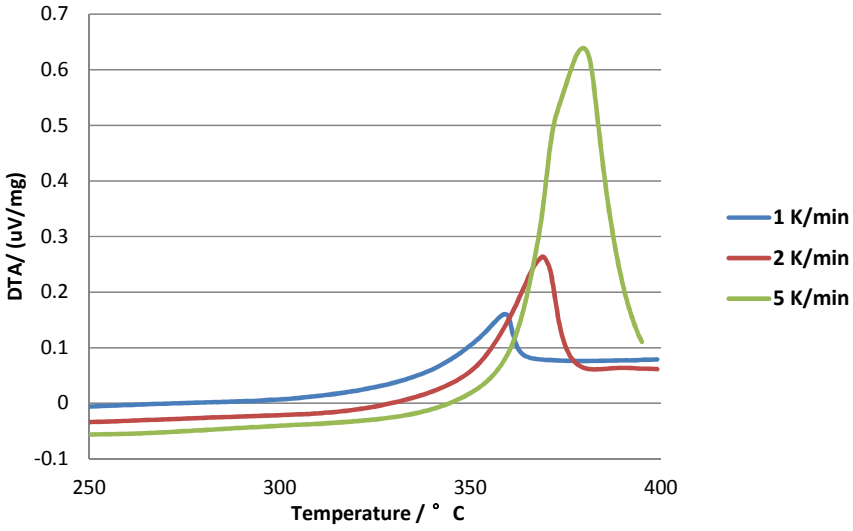

Figure 4.19: DTA results of $LiNH_2$-72-T-3BN, heating rate: 1 K/min, 2 K/min and 5 K/min

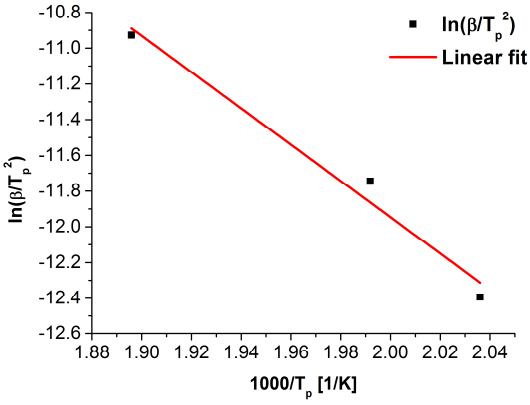

Figure 4.20: Activation energy calculation of sample LiNH2-72-T

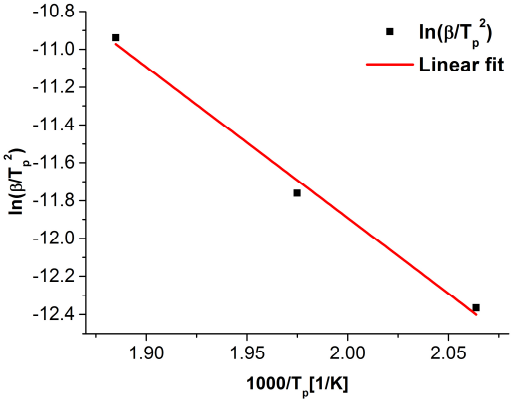

Figure 4.21: Activation energy calculation of sample $LiNH_2$-72-T-3BN

4.2 The $LiNH_2$+LiH System

Similar to the $LiNH_2$ samples, $LiNH_2$+LiH samples were also ball milled using different process parameters. In some cases the effect of BN as additive was studied, as well(see Table 4.2).

Table 4.2: $LiNH_2$ +LiH sample names, composition and milling process parameters

Sample name	Component	Milling time / Hour	Dry/wet ball milled	Milling ball diameter/ (Weight Ratio)	BN Additive / wt%
N12L(as received)	$LiNH_2$:LiH 1:1.2	_	_	_	_
N12L-24h-D	$LiNH_2$:LiH 1:1.2	24	Dry	5 and 2 mm/(7:3)	_
N12L-72-T	$LiNH_2$:LiH 1:1.2	72	Wet (with THF)	5 and 2 mm/(7:3)	_
N12L-72-D	$LiNH_2$:LiH 1:1.2	72	dry	5 and 2 mm/(7:3)	_
N12L-72-T-3BN	$LiNH_2$:LiH 1:1.2	72	Wet (with THF)	5 and 2 mm/(7:3)	3
N12L-72-T-1.5BN	$LiNH_2$:LiH 1:1.2	72	Wet (with THF)	5 and 2 mm/(7:3)	1.5
N12L-72-T-6BN	$LiNH_2$:LiH 1:1.2	72 h	Wet (with THF)	5 and 2 mm/(7:3)	6
N12L-72-D-3BN	$LiNH_2$:LiH 1:1.2	72 h	dry	5 and 2 mm/(7:3)	3
N12L-72+24-T	$LiNH_2$:LiH 1:1.2	1^{st} step: 72 2^{nd} step: 24	Wet (with THF)	1^{st} step: 5 and 2 mm/(7:3) 2^{nd} step: 0.1 mm	_

4.2.1 Characteristics of Sample Powders

4.2.1.1 Microstructure Study using Scanning Electron Microscopy (SEM)

In order to study the influence of various milling conditions on the samples, SEM images were taken of dry and wet ball milled samples after 24 and 72 hours of processing (Figure 4.22-Figure 4.25).

For each sample, two SEM images are shown. The micrographs on the left side were obtained with a backscattered electron detector (QBSD) at relatively small magnification. Those images are suitable to evaluate the size and morphology of the particle agglomerations. The images on the right side were obtained with a secondary electron detector (In-lens) at larger magnification to display the microstructure of individual particles.

The particle agglomerations of samples with shorter milling time (Fig 4.22a and 4.23a) had diameters up to 50 µm. For both the wet and dry ball milling, the agglomeration sizes were reduced after longer milling time (cf. Figure 4.24a and Figure 4.25a). The higher magnifications showed comparatively smaller primary particles for the dry ball milled samples. However, after long time dry ball milling processes, the packing densities of the particles were rather high. With wet ball milling, the agglomerates exhibited a lower packing density, which was associated with a higher specific surface area which will be quantitatively analyzed later. This observation may be attributed to the existence of the liquid phase between the particles in the wet ball milling process. The comparatively loose packing of the particles might help to enlarge the free surfaces of the samples.

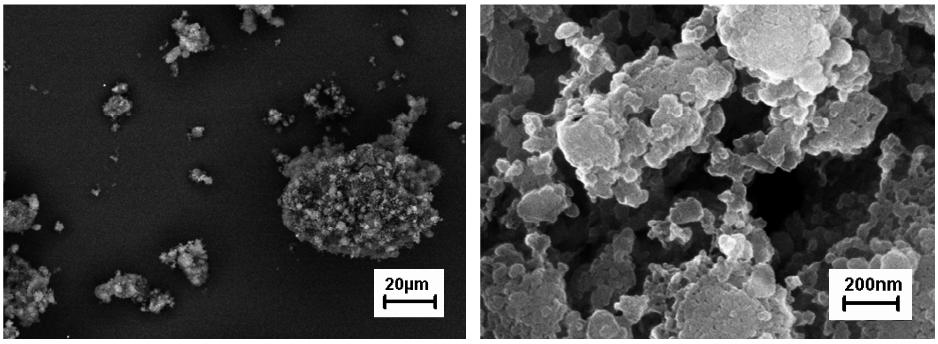

Figure 4.22: SEM images of sample N12L-24h-D

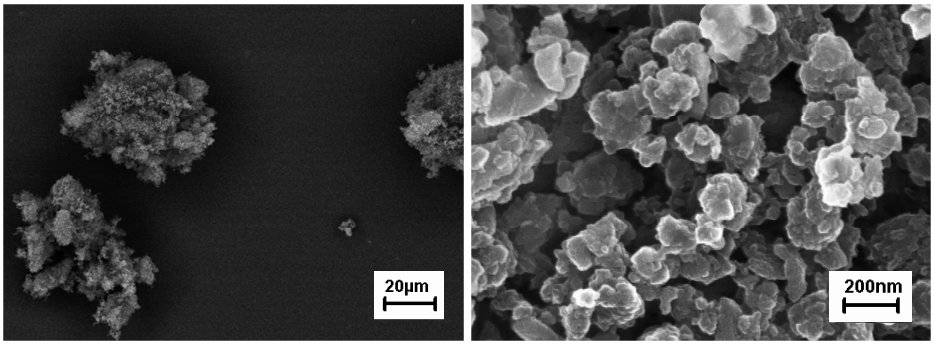

(a) (b)

Figure 4.23: SEM images of sample N12L-24h-T

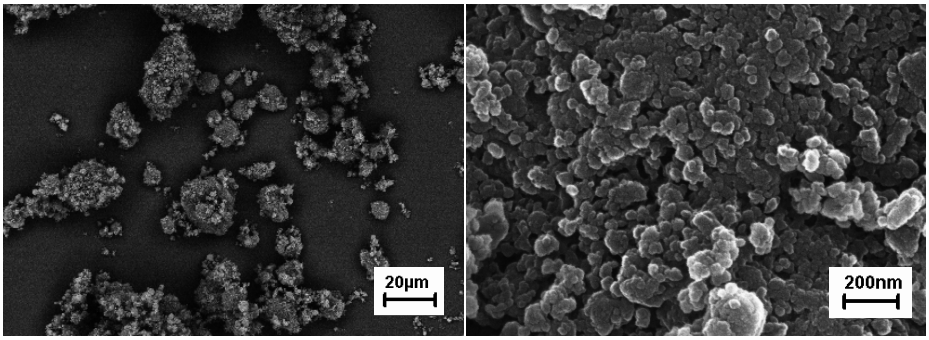

(a) (b)

Figure 4.24: SEM images of sample N12L-72h-D

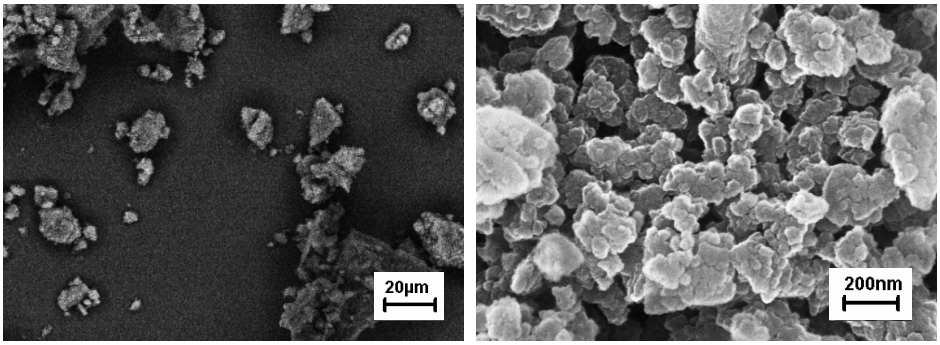

(a) (b)

Figure 4.25: SEM images of sample N12L-72h-T

The particle sizes of the four samples were studied with software Analysis Pro. 100 particles were chosen from 2-3 different SEM images for each sample. The resulted particle size distributions with mathematical mean values are illustrated in Figure 4.26. As discussed earlier, the particles of the dry ball milled samples always tended to have a high packing density. On the other hand, the higher impact and friction force led to particles with finer sizes. As shown in Figure 4.22b and Figure 4.24b, many such fine particles adhere together, sometimes more likely resulting in a newly formed big particle than an agglomeration. Therefore the dry ball milled samples have a wider range of particle size distribution than that of the wet ball milled samples (cf. Fig 4.26).

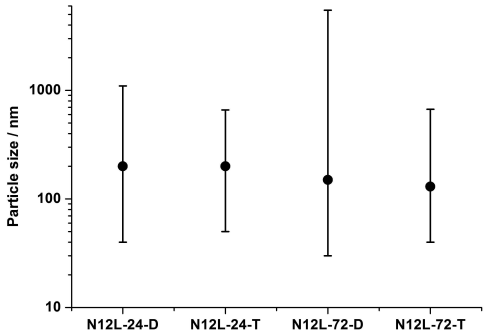

Figure 4.26: Particle size distribution of $LiNH_2$+LiH dry/wet milled samples with different milling time

The specific surface areas from Figure 4.27 are mostly higher than the results from Varin et al [Var10a] after 100 hours of ball milling (SSA: 45.6 m^2/g). This may be due to the planetary milling method and the high crushing strength of YSZ media which gave effective milling results.

In contrast to the $LiNH_2$ samples, the wet ball milled samples tended to have approx. 20 % larger specific surface areas as compared to dry ball milled samples. This indicated that the wet ball milling processes help to enlarge the specific surface areas of LiH but not of $LiNH_2$. It is also suggested that the lower packing density of the agglomerates after wet ball milling could enhance the specific surface area of the samples. A comparison of the BET results of the dry ball

milled (24 hours: 39 m^2/g; 72 hours: 69 m^2/g) and the wet ball milled samples (24 hours: 50 m^2/g; 72 hours: 92 m^2/g) support this conclusion.

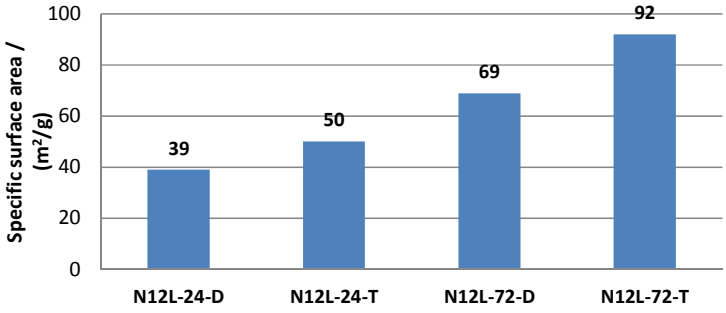

Figure 4.27: Specific surface area of $LiNH_2$ +LiH sample powders determined by the BET method

The influence of 24-hour additional milling with fine milling balls is presented in Figure 4.28. It can be seen that the particle size covers a range between approx. 40 and 500 nm before the fine ball milling process (cf. Fig 4.29, N12L-72-T). After 24 hours of additional milling with smaller balls, the resulting particle sizes were generally reduced (cf. Fig 4.29, N12L-72+24-T). What can be noticed is that the particles in Figure 4.28b tend to adhere closer to each other than those illustrated in Figure 4.28a. The reason may be that although the fine milling balls are small enough to smash the smaller particles, the impact force might be too weak to break the larger agglomerates.

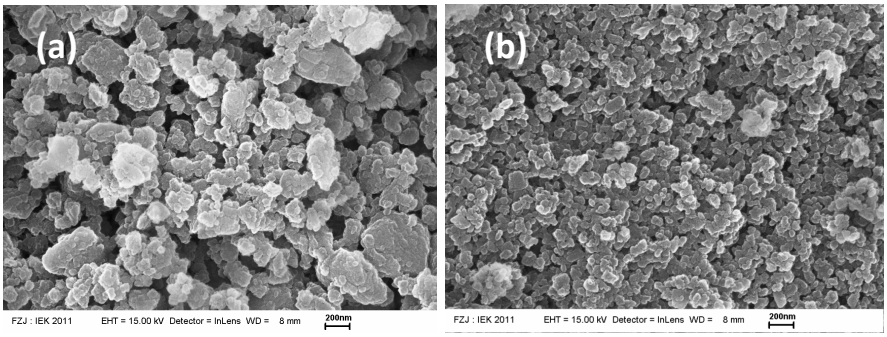

Figure 4.28: SEM image of (a): N12L-72-T and (b): N12L-72+24-T in large magnification

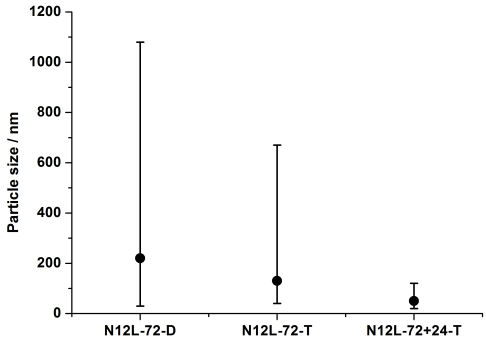

Figure 4.29: Particle size distribution of $LiNH_2$+LiH as milled samples

Figure 4.30 illustrates the specific surface areas of three wet ball milled samples measured by the BET method. Even though the SEMs show reduced particle sizes for the sample with repeated milling (N12L-72+24-T), the increase of the specific surface area is only 10 m^2/g. The limited increase coincided with the high packing density of the N12L-72+24-T sample particles (cf.Fig 4.28b).

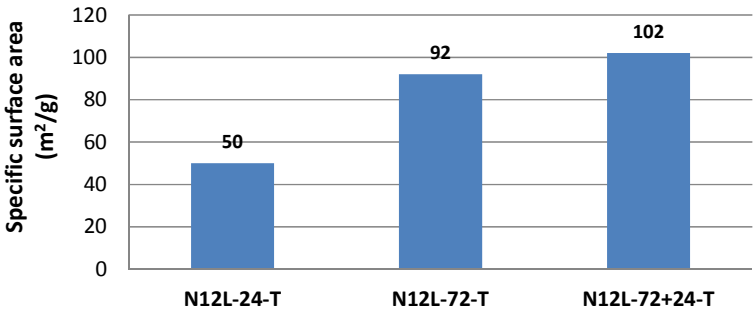

Figure 4.30: Specific surface area of three $LiNH_2$ +LiH sample powders measured by the BET method

4.2.1.3 Microstructure Study Using X-ray Diffraction (XRD)

The XRD patterns shown in

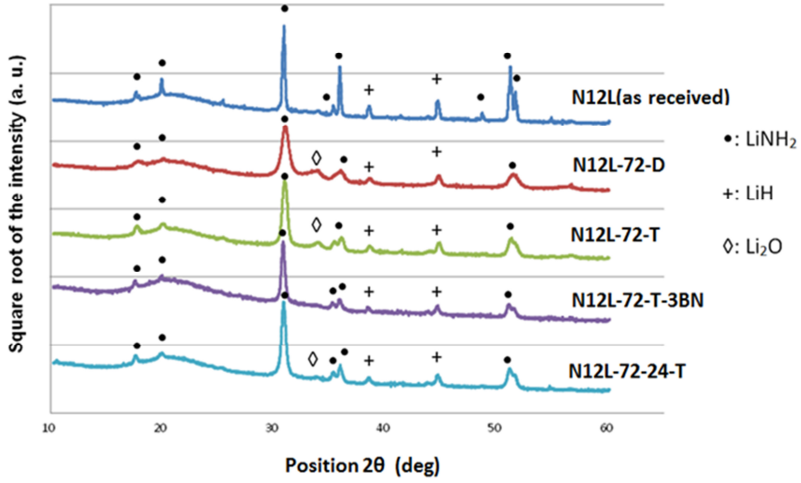

Figure 4.31 visualize that $LiNH_2$ and LiH phases existed in all the samples after dry or wet ball milling. No new phases except traces of Li_2O in some samples were found. Crystallite sizes of the samples calculated according to the Williamson-Hall method confirmed that both wet and dry ball milling processes reduced the crystallite size clearly (cf. Fig 4.32a) and introduced lattice strain (cf. Fig 4.32b). Neither the 3 wt% of BN nor the additional 24-hour fine wet ball milling process affected the crystallite size or lattice strain evidently.

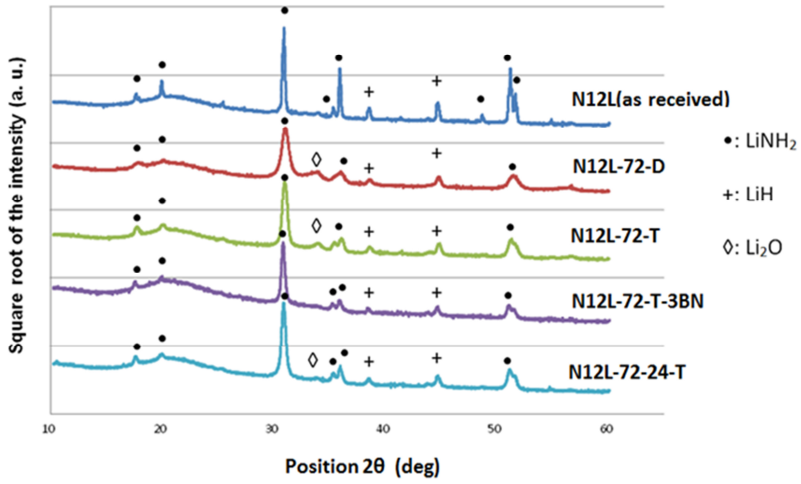

Figure 4.31: XRD patterns of five differently processed $LiNH_2$+LiH samples

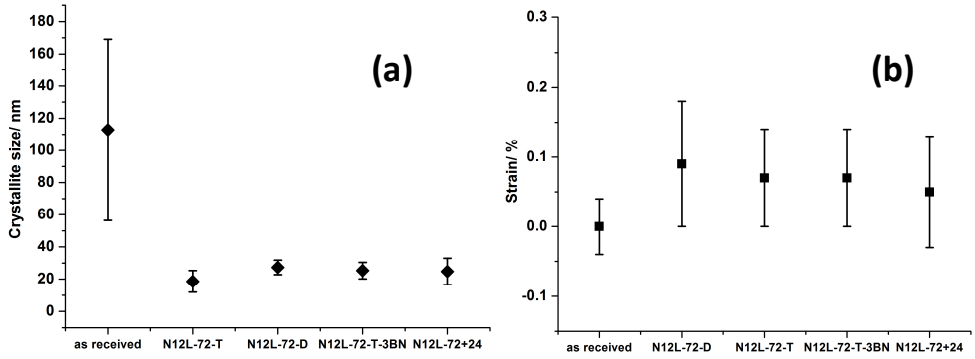

Figure 4.32: Calculated (a) crystallite sizes and (b) lattice strain of the as-received and differently milled $LiNH_2$+LiH samples

4.2.1.4 Characterization of Samples with Different Amounts of BN

In order to study the influence of different amounts of BN on the microstructure of $LiNH_2$+LiH samples, SEM images of samples with different amounts of BN were taken (sample N12L-72-T-3BN and sample N12L-72-T-6BN). The corresponding SEM images are presented in Figure 4.33.

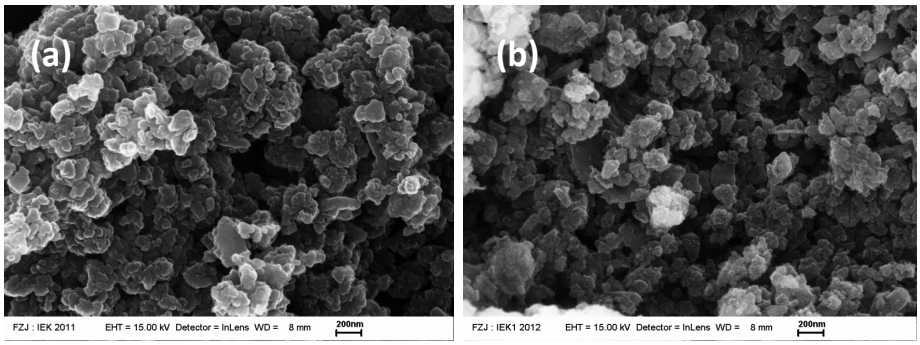

Figure 4.33: SEM image of (a): N12L-72-T-3BN and (b): N12L-72-T -6BN in large magnification

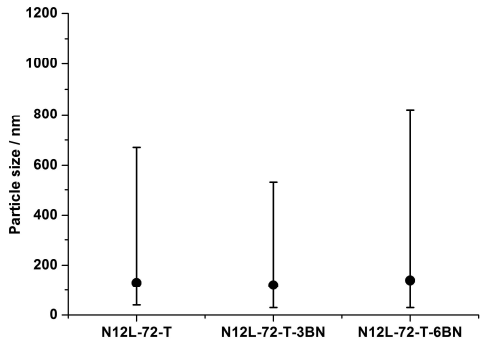

Figure 4.34: Particle size distribution of $LiNH_2$+LiH as milled samples with different amount of BN

In Figure 4.33, no clear morphology difference could be recognized between the two samples. The particle sizes were studied with software Analysis Pro. The results in Figure 4.34 showed no significant differences in mean particle size. Even a comparison with the sample without additive (cf. Fig 4.28a) does not reveal any significant difference between the three samples. Obviously, three weight percent of BN were not sufficient to influence particle size and morphology of the samples. Therefore, the possible influence of BN on the behavior of the $LiNH_2$+LiH system cannot be attributed to a change in the powder particle morphology or size.

4.2.2 Sorption Behavior

Figure 4.35 summarizes the desorption profiles of the samples N12L-72-T, N12L-72+24-T, N12L-72-3BN-T, and N12L-72-D. The experiments were done with the volumetric Belsorp-HP system at a desorption temperature of 285°C. The desorption profiles of the four samples are very similar. Neither milling time, nor milling condition or inclusion of BN seemed to have an influence. Although sample N12L-72+24-T had a larger specific surface area and smaller particle sizes, the desorption kinetic and ending pressure did not differ from that of sample N12L-72-T. Obviously, the microstructure of the samples did not influence the sorption behavior of the $LiNH_2$+LiH system significantly.

The lacking influence of BN on the desorption kinetic of $LiNH_2$+LiH is in contrast to the report done by Aguey-Zinsou et al. [Agu07]. According to their work, BN improves the desorption kinetic of $LiNH_2$+LiH materials. This effect of BN on the $LiNH_2$+LiH system in this study will be further addressed in chapter 4.2.5.

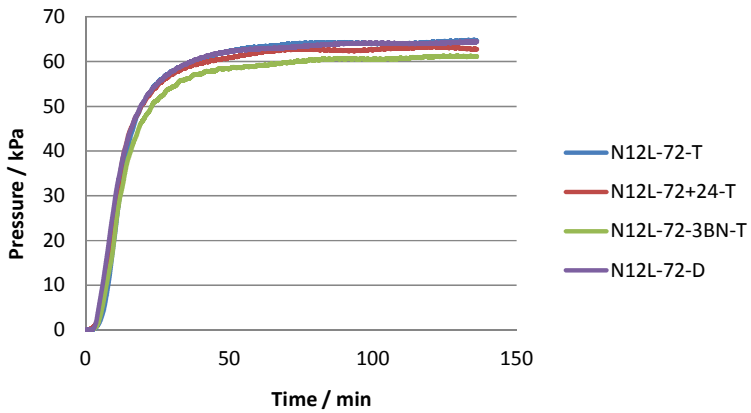

Figure 4.35: Desorption profiles of five differently processed LiNH2 samples at 285°C measured in the Belsorp-HP system

4.2.2.2 The Influence of Different Amounts of Additive on the System Behavior

In order to study the influence of different amounts of BN on the desorption behavior of the $LiNH_2$ +LiH system, samples with different BN amounts (1.5, 3, and 6 wt% BN) were studied using the Belsorp-HP volumetric system. The samples were heated up to 250°C in the closed system and kept at this temperature for 3 hours. The pressure results are illustrated in Figure 4.36.

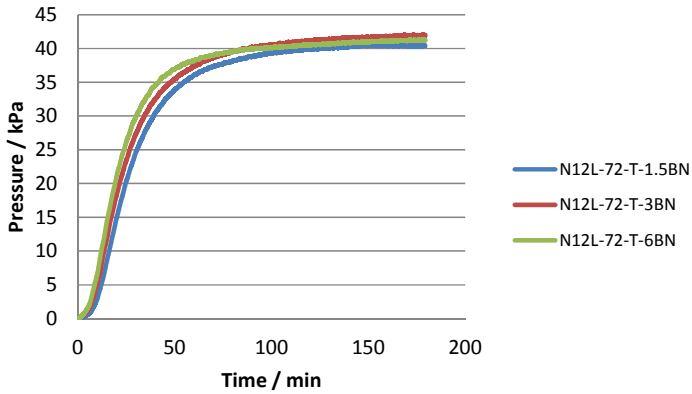

Figure 4.36: Desorption of three $LiNH_2$ +LiH samples with 1.5, 3 and 6 wt% BN, respectively, at 250°C for 3 hours

The initial desorption curve shows an increase in desorption kinetic with the amount of BN. However, the differences were not significant. The calculated weight loss for all the samples ranged from 2.1 wt% to 2.5 wt% at the temperature of 250°C.

4.2.3 Thermodynamic Analysis

4.2.3.1 Activation Energy

The influence of BN on the activation energy was studied for the samples N12L-72-T and N12L-72-T-3BN using the STA 449 F3 Jupiter system (Introduction see Chapter 3.3.2). The samples were heated from 50°C to 300°C at heating rates of 1 K/min, 2 K/min, and 5 K/min, respectively.

The sample masses were 60-63 mg. The results for the heating rate of 5 K/min are shown in Figure 4.37 and Figure 4.38. During the heating process, neither sample showed a release of NH_3 (cf. blue mass line for m=17). Only H_2 (m=2, pink lines) was detected.

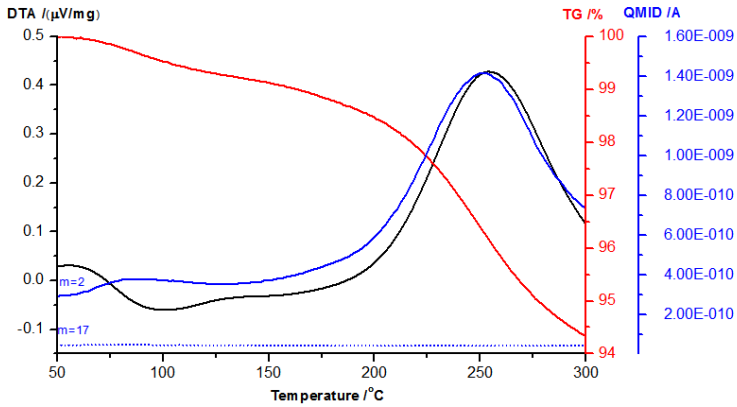

Figure 4.37: DTA-TG-MS result of sample N12L-72-T, heating rate: 5 K/min

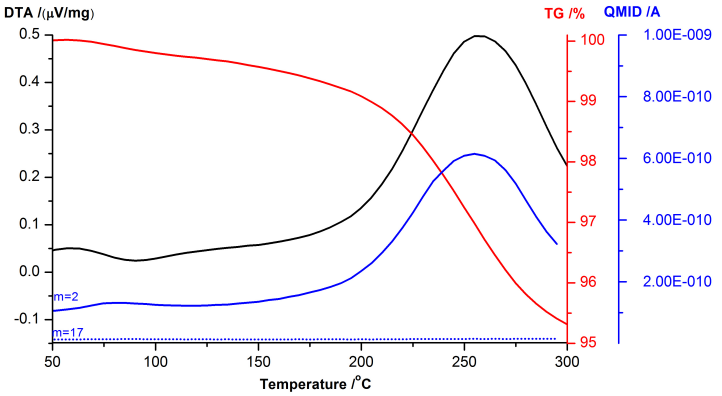

Figure 4.38: DTA-TG-MS result of the sample N12L-72-T-3BN, heating rate: 5 K/min

Similar to the findings of Yao et al. [Yao07] and Varin et al. [Var10a], the weight losses of the samples were accompanied by a very broad endothermic DTA peak. However, the on-set hydrogen desorption temperatures of both samples in this study were below 100°C, which are considerably lower than the 120-160°C reported by Yao et al. [Yao07] or the 187-268°C

published by Varin et al. [Var10a] With 219-255°C and 210-257°C, respectively, the peak positions measured in this study were up to 70°C lower than those reported by Varin et al. [Var10a]. However, their higher heating rate (5, 10, and 15 K/min) might be a reason for the differences.

In order to calculate the activation energy, the peak point (T_p) of the DTA result was taken (see also chapter 2.6.1). The three heating rates yielded three DTA peaks for each sample (see Figs 4.39 and 4.40). An X-Y plot with $1000/T_p$ on the X axis and $\ln(\beta/T_p^2)$ as Y variable (β being the heating rate) yielded the red lines in Figure 4.41 and Figure 4.42. The corresponding R-square values were larger than 0.95, which is better than published references [Var11] with four points. One reason for the better R-square values for the linear fit may be the use of only 3 points in contrast to that in the literature (4 points). The other reason may be the slower heating rates applied in this study which might render the temperature signals more reliable.

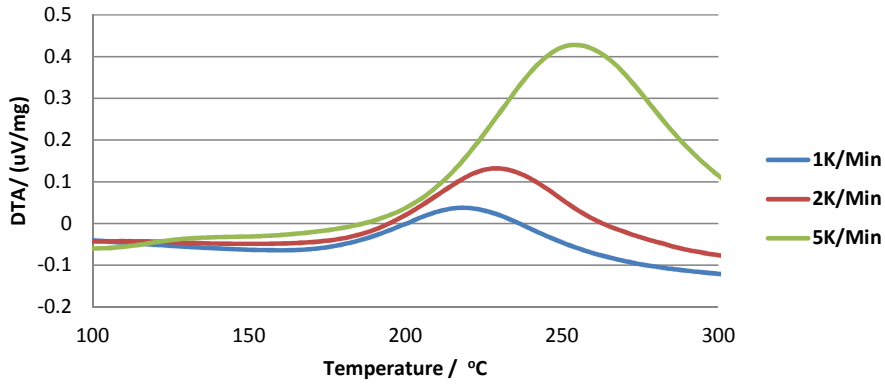

Figure 4.39: DTA result of N12L-72-T, heating rate: 1 K/min, 2 K/min, and 5 K/min

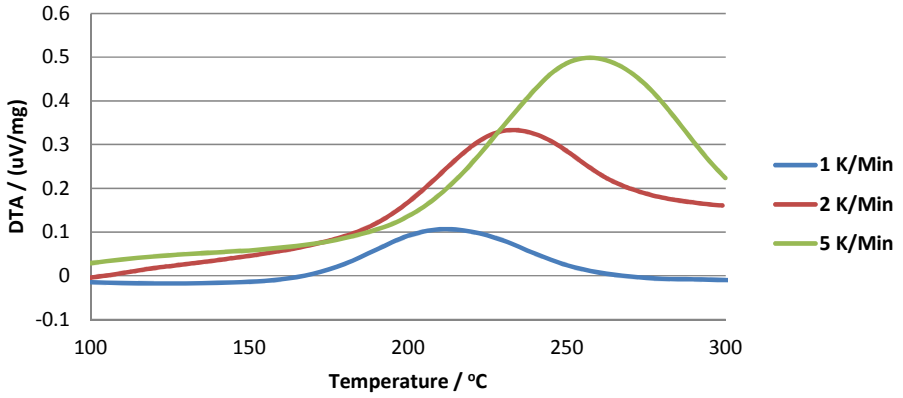

Figure 4.40: DTA result of N12L-72-T-3BN, heating rate: 1 K/min, 2 K/min, and 5 K/min

Applying the Kissinger method, the activation energy E_a can be calculated from the slope of the linear fit curves in Figure 4.41 and Figure 4.42. For the sample without additives (N12L-72-T), E_a was calculated as 84.7± 12.0 kJ/mol, which is very close to published data (85 kJ/mol) for the same system [Var11]. For the sample with 3 wt% BN (N12L-72-T-3BN) an E_a of 68.0± 6.5 kJ/mol was calculated. The comparison of the results shows that with the same milling process, the sample with 3 wt% BN has a lower activation energy based on the Kissinger method.

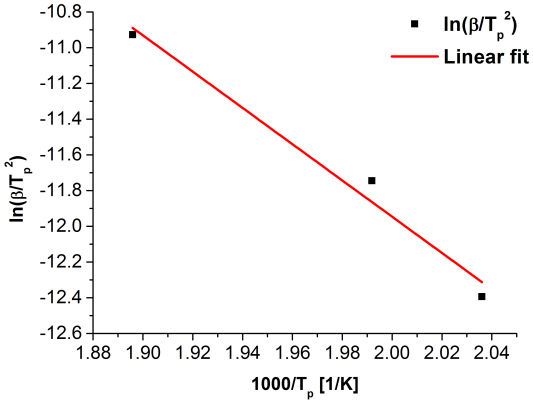

Figure 4.41: Activation energy calculation of N12L-72-T

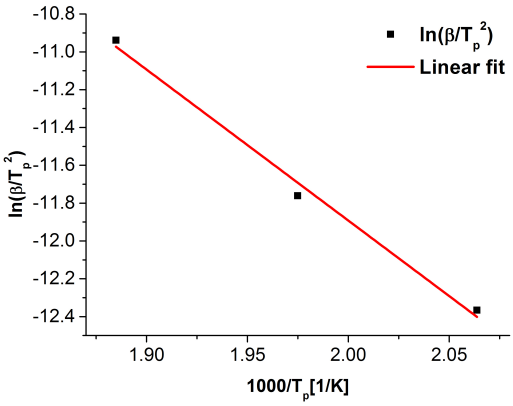

Figure 4.42: Activation energy calculation of N12L-72-T-3BN

4.2.3.2 Reaction Enthalpy Calculation

In order to study the desorption enthalpy of the different samples, three ball milled samples were desorbed at 4 different temperatures in the range from 250°C to 325°C with the Belsorp-HP volumetric system. The desorption time was 3 hours in each case.

The desorption results are illustrated in Figure 4.43, Figure 4.44, and Figure 4.45. The higher the desorption temperature the faster the initial desorption kinetic and the higher the final pressure, which was reached after approx. 60 min.

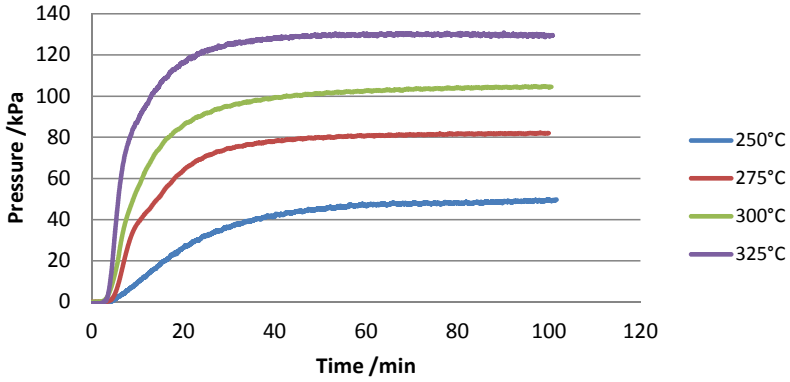

Figure 4.43: Desorption experiments of N12L-72-T, desorption temperatures were 250°C, 275°C, 300°C and 325°C

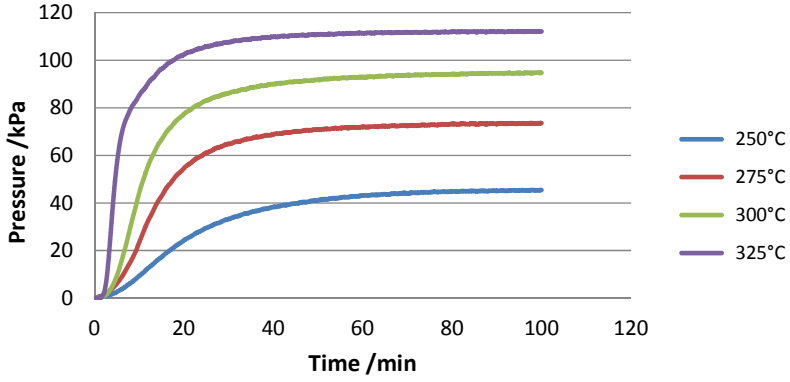

Figure 4.44: Desorption experiments of N12L-72-T-3BN, desorption temperatures were 250°C, 275°C, 300°C and 325°C

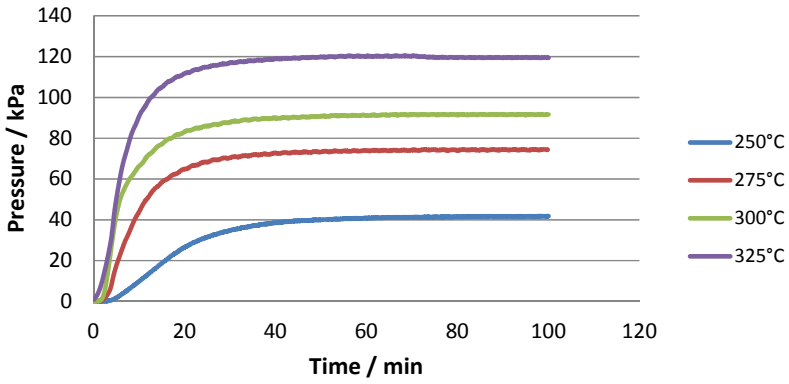

Figure 4.45: **Desorption experiments N12L-72-D-3BN, desorption temperature were 250°C, 275°C, 300°C and 325°C**

Applying the Van't Hoff equation (see Chapter 2.6.2), the enthalpy can be derived from a plot $\ln(P/P_0)$ vs. 1000/T. For each sample there were 4 data points at 4 different temperatures. Figure 4.46, Figure 4.47, and Figure 4.48 illustrate the situation for the three model samples. From the slopes of the linear fit, the desorption enthalpies and entropies were calculated and are given in the figures. The quite high R^2 values (over 0.93) indicating that the calculated enthalpies are reliable.

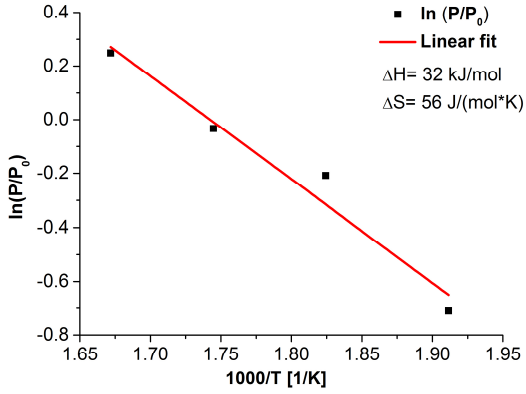

Figure 4.46: Enthalpy calculation of the sample N12L-72-T

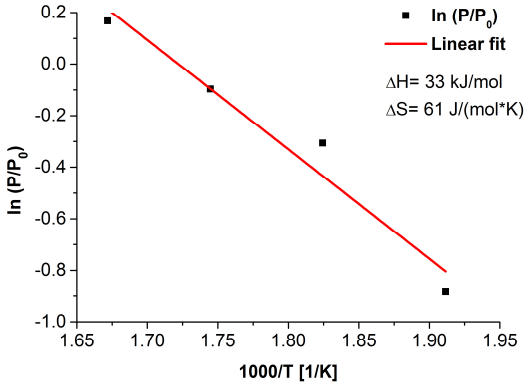

Figure 4.47: **Enthalpy calculation of the sample N12L-72-D-3BN**

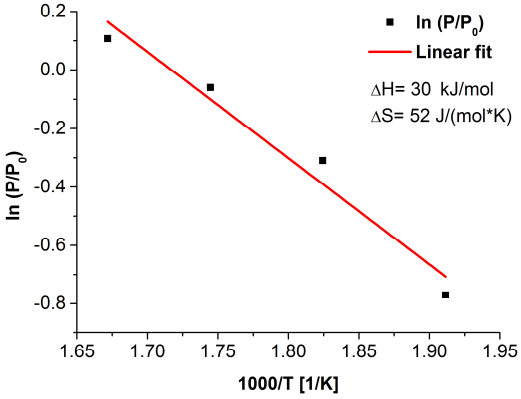

Figure 4.48: **Enthalpy calculation of the sample N12L-72-T-3BN**

Considering the standard errors of the linear fits, the desorption enthalpies for the samples are calculated. Considering the margin of error, there are no significant differences in the resulting desorption enthalpies between dry and wet ball milled samples (33±5 kJ/mol and 32±4 kJ/mol), and between samples with and without BN (30±4 kJ/mol and 32±4 kJ/mol). The results illustrated that neither wet ball milling process nor BN as additive influences the desorption enthalpy definitely.

The $LiNH_2$+LiH hydrogen storage system was first developed by Chen et al. [Che02], who reported an enthalpy of 45 kJ/mol. Varin and Yang [Var11] published a desorption enthalpy of 62.4 kJ/mol for the material system without additive. Even though slightly lower, the results of this study are in reasonable accordance with the literature.

4.2.4 Material Characteristics after Cyclic Desorption and Absorption

Not only the as-received and as-milled samples, but also the samples after cyclic desorption and absorption were characterized in this study. The wet ball milled $LiNH_2$+LiH samples were desorbed at 250°C. After that, absorption processes were done with some samples. The absorption temperature was 200°C with a beginning absorption pressure of approx. 1000 kPa. The desorption and absorption time for each sample was three hours. Table 4.3 illustrates the sample names and the corresponding process history.

Table 4.3: Preparation methods of the samples treated by cyclic desorption and absorption

Sample name	As milled sample	Desorption Temperature / °C	Absorption Temperature/ °C
N12L-25D	N12L-72-T	250	-
N12L-25D-20A	N12L-72-T	250	200
N12L-3BN-25D	N12L-72-T-3BN	250	-
N12L-3BN-25D-20A	N12L-72-T-3BN	250	200

Initially, the samples were studied by XRD method. The resulting XRD patterns are presented in Figure 4.49. The first two samples measured after desorption showed Li_2NH as main phase. The small Li_2O peaks that could be found suggest partial oxidation during the desorption process.

After hydrogen absorption (sample N12L-25D-20A and N12L-3BN-25D-20A), $LiNH_2$ and LiH were observed as main phases. This means that the samples achieved indeed one hydrogen desorption-absorption cycle and returned to the initial components.

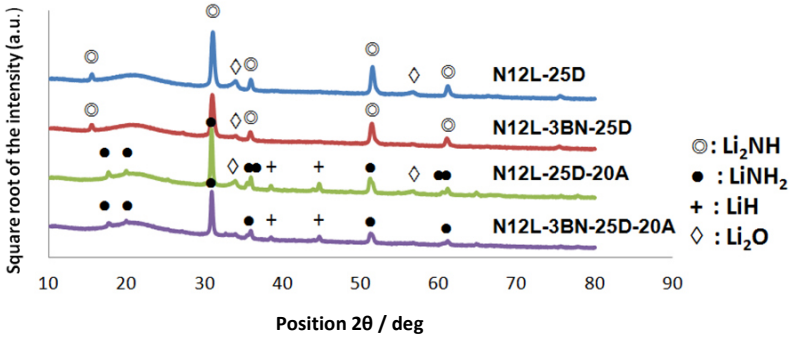

Figure 4.49: **XRD patterns of the samples after desorption and absorption [Du12]**

Based on the XRD patterns, the crystallite sizes of the milled samples and samples after desorption/absorption were calculated according to Williamson-Hall method. The results are shown in Figure 4.50.

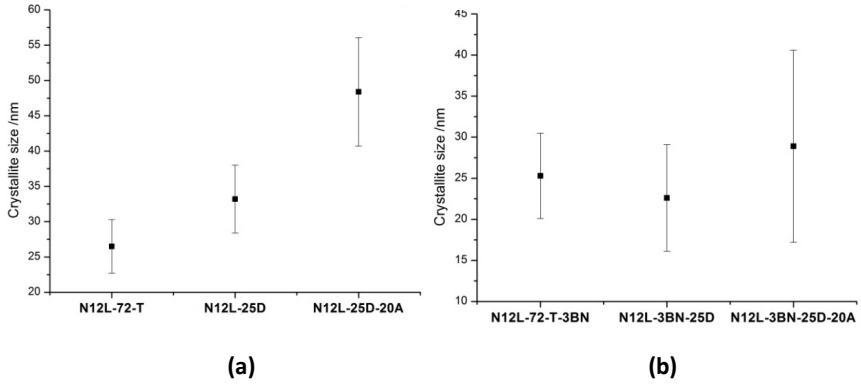

Figure 4.50: **Calculated crystallite sizes of two samples (a: without and b: with BN) after milling, 1st desorption, and 1st absorption, respectively**

In the sample without BN the crystallite size increased after the 3-hour desorption process. After the absorption process, the crystallite size reached almost twice the size of the as-milled original.

After the same cycle of three hours of desorption and three hours of absorption, the sample with 3 wt% of BN did not show a significant change in crystallite size (Figure 4.50b), which might

be an indication that BN stabilizes the crystallite size of the $LiNH_2$+LiH system during hydrogen sorption processes efficiently. To see Figure 4.51, after the 1st desorption both samples released the lattice stain, after the 1st absorption, some new strain appeared again.

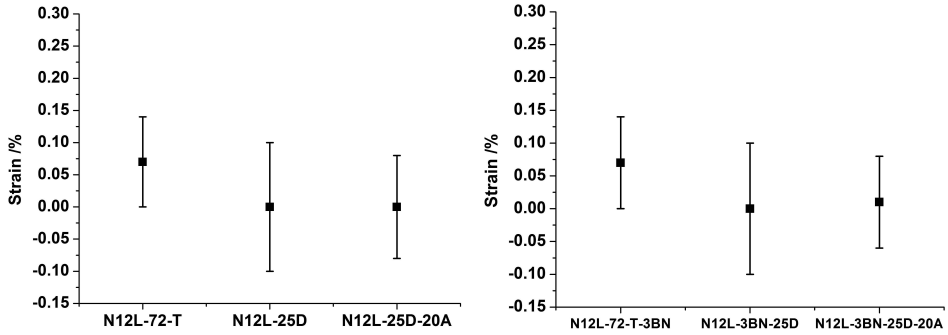

Figure 4.51: Calculated lattice strain of $LiNH_2$+LiH as milled, after 1st desorption, and 1st absorption, respectively (a): without BN, (b): with 3 wt% BN

Figure 4.52 displays SEM images of the samples after the desorption/absorption processes. The first line shows the sample without BN (N12L-72-T). In the SEM images it can be seen that after desorption and absorption processes, the particle size did not change visibly. The second line shows the SEM images of the sample with BN after desorption and absorption, respectively. From the SEM images it can be see that the particles sizes also show no obvious change. Figure 4.53 gives a quantification result of the particle size distribution which conforms to the conclusion above.

This results means that during the desorption and absorption processes, the particle sizes of the $LiNH_2$+LiH samples did not change. The sample with and without BN had no significant differences.

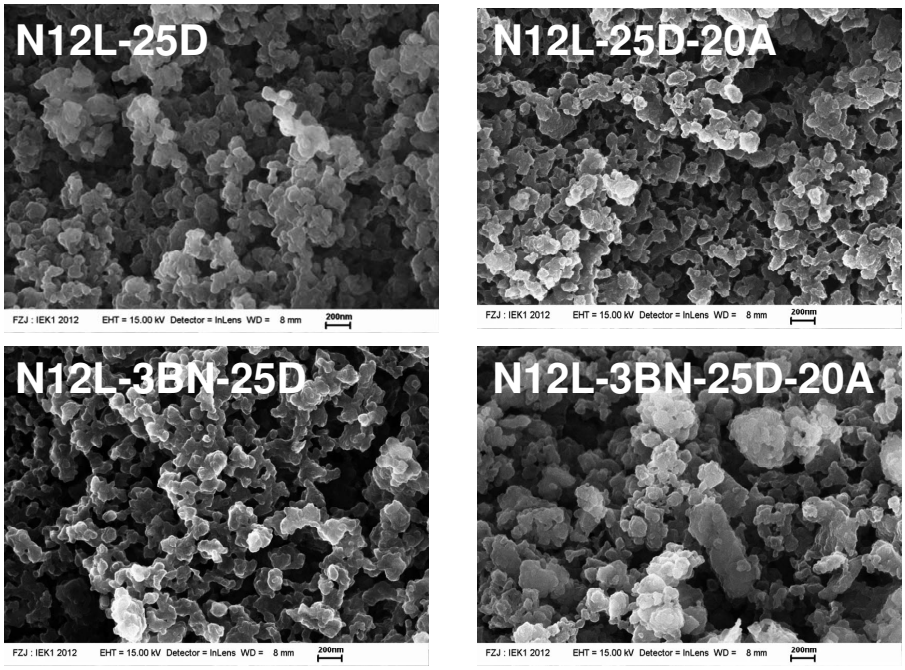

Figure 4.52: SEM images of two $LiNH_2$+LiH samples after hydrogen desorption and absorption [Du12]

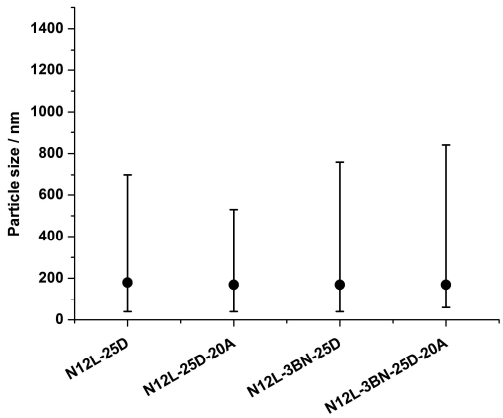

Figure 4.53: Particle size distribution of $LiNH_2$+LiH (with and without BN) after 1st desorption, and 1st absorption, respectively

4.2.5 Improvement of the Desorption Behavior by Additives

4.2.5.1 Wet Ball Milled Samples with BN

In order to study the influence of BN as additive on the $LiNH_2$+LiH system, the sample behavior was also studied in a cyclic desorption-absorption program. The desorption temperature was 285°C and the absorption temperature 200°C. The desorption/absorption period was 3 hours each and the initial absorption pressure was approx. 1000 kPa. Figure 4.54 gives an example of the first to third hydrogen desorption cycle for a wet ball milled sample without additives (N12L-72-T). Much less hydrogen was desorbed within the observed time period during the 2nd and 3rd cycles as compared to the 1st cycle. The relative desorption amount was 84.6 % and 38.5 % of the 1st cycle. Figure 4.54 also illustrates that the hydrogen release rates became smaller with increasing cycle number.

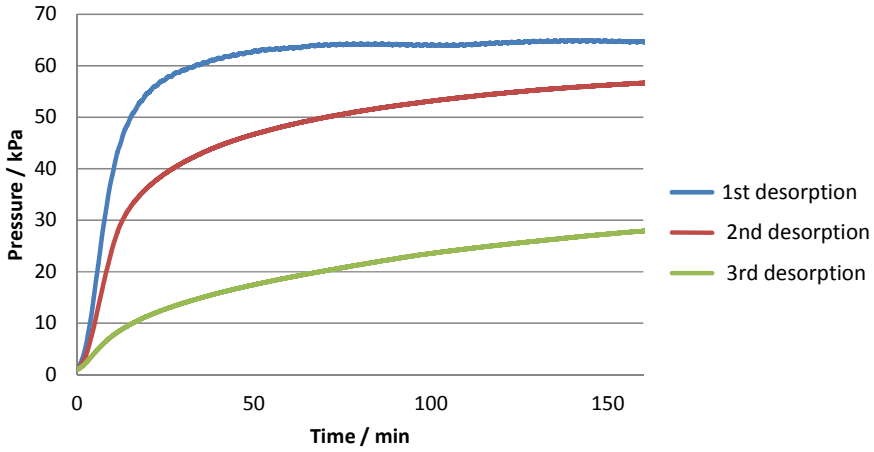

Figure 4.54: Cyclic hydrogen desorption of sample N12L-T-72 (D: 285°C, A: 200°C) [Du12]

Figure 4.55 shows the cyclic hydrogen desorption curves of a sample with BN (N12L-72-T-3BN). The cycle performance of this sample is much better than for the previous example without additive (see Figure 4.47). The desorption amount after the 2nd and 3rd cycle is still 90% and 85%

of that obtained in the first cycle, respectively. Also the release rates of the 2nd and 3rd cycles are similar to that of the 1st cycle.

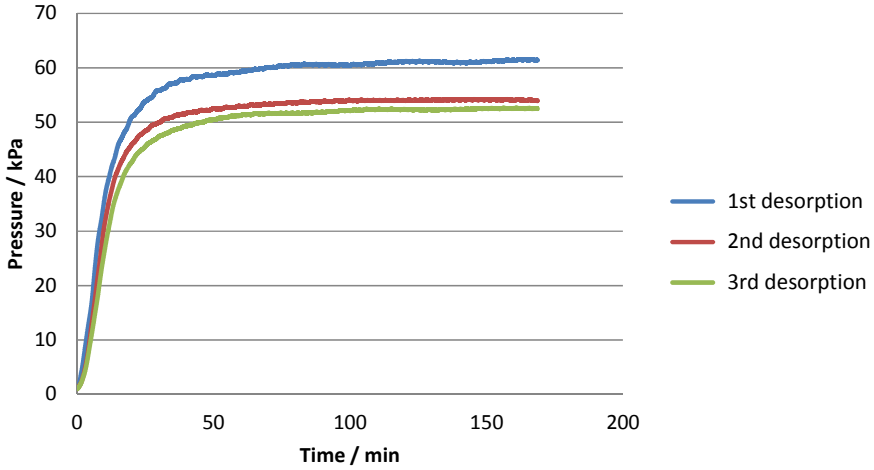

Figure 4.55: Cyclic hydrogen desorption curves of T52-72-3BN (D: 285°C, A: 200°C) [Du12]

According to the results presented in Figure 4.54 and Figure 4.55, the addition of 3 wt% BN can effectively enhance the recyclability of the $LiNH_2$+LiH system. In the previous chapters it was stated that BN did not influence the particle size of the $LiNH_2$+LiH samples, but seems to stabilize the crystallite size of the samples. That may give a hint that the recyclability of $LiNH_2$+LiH powder mainly depends on the crystallite size of the material.

4.2.5.2 BN with Dry Ball Milled Samples

In order to further understand the influence of BN on the $LiNH_2$+LiH hydrogen storage system, 3 wt% of BN was added to dry ball milled samples and their desorption behavior was studied.

The desorption temperatures were 275°C and 300°C. The desorption experiments were performed in the Belsorp-HP volumetric system. The desorption phases lasted three hours. After that, the whole system was cooled down with the furnace to room temperature. The whole process (including heating and cooling) took about five hours per experiment.

The results for three samples are shown in Figure 4.56-Figure 4.58. It can be seen that samples N12L-72-T-3BN and N12L-72-D-3BN have comparable desorption kinetics and equilibrium pressures. As the temperatures of the samples were only slowly decreasing during the cooling process (from minute 180 to minute 300), the samples began to absorb hydrogen again. For the samples without BN (N12L-72-D, cf. Fig 4.58), this re-absorption effect was only weak at either temperature.

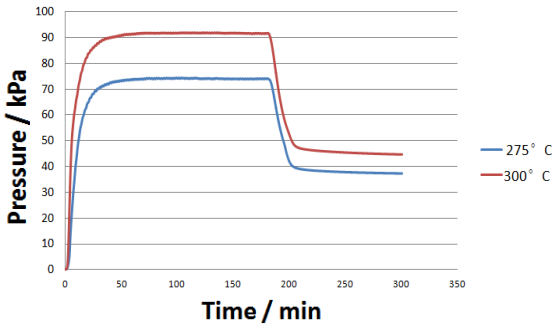

Figure 4.56: Desorption curves of sample N12L-72-D-3BN at 275°C and 300°C, with cooling down step

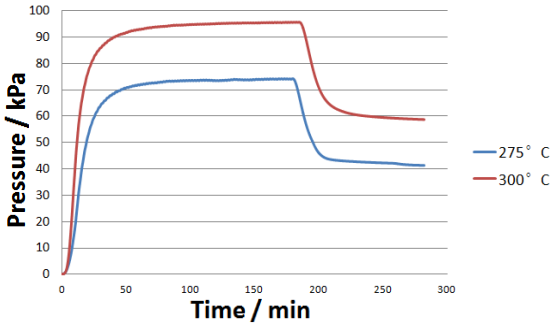

Figure 4.57: Desorption curves of sample N12L-72-T-3BN at 275°C and 300°C, with cooling down step

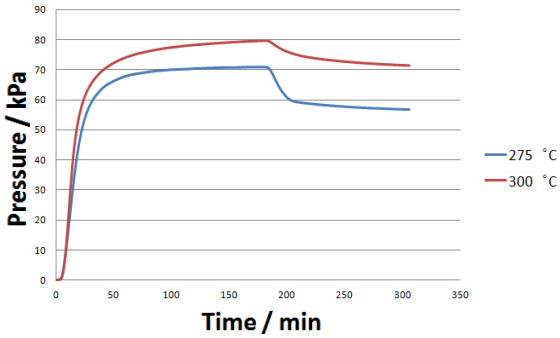

Figure 4.58: Desorption curves of sample N12L-72-D at 275°C and 300°C, with cooling down step

In order to prove that the pressure drop was mainly attributable to the re-absorption and not due to the influence of the temperature on the gas pressure, two blank measurements with empty sample holders were performed (cf. Figure 4.59).The empty sample holders were connected to the Belsorp-HP volumetric system, the system was filled with helium up to about 20 kPa and 45 kPa, respectively, and heated to 250°C. After the pressure had reached a constant level, the whole system was cooled down to room temperature. Even though, these two experiments were carried out at slightly different temperatures and pressures as compared to the desorption experiments in this study, they illustrate that the influence of the temperature on the system pressure was minor and hence, that the observed pressure drop in Figure 4.56 and Figure 4.57 was mainly caused by the hydrogen absorption of the test samples.

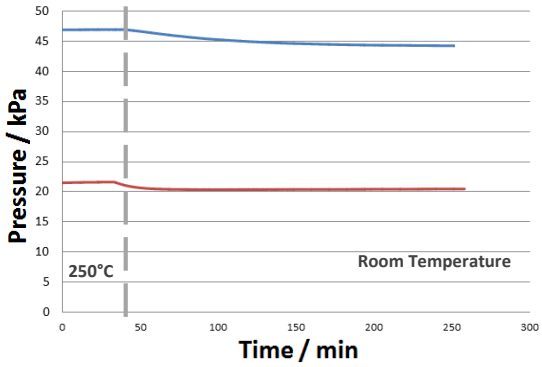

Figure 4.59: Belsorp system cooling down with empty sample holder (250°C to room temperature)

4.2.5.3 Influence of the Amount of BN on the $LiNH_2$+LiH System

The influence of the amount of BN on the first desorption behavior was described in Chapter 4.2.2.2. Here, the influence of the amount of BN on the recyclability will be described. Cyclic hydrogen desorption and absorption experiments were performed with samples N12L-T-1.5BN and N12L-T-6BN. The desorption temperature was 250°C, the absorption temperature 200°C. Desorption and absorption time periods were three hours, each. The initial desorption pressure was vacuum and absorption pressure was 1000 kPa. The results are shown in Figure 4.60 and Figure 4.61.

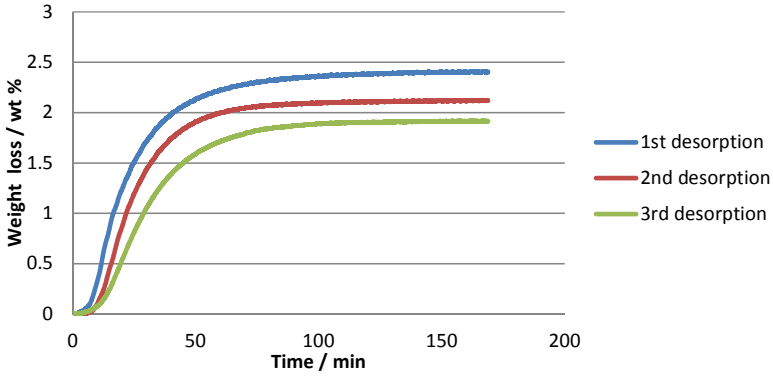

Figure 4.60: Cyclic desorption and absorption for N12L-72-T-1.5BN, calculated weight losses

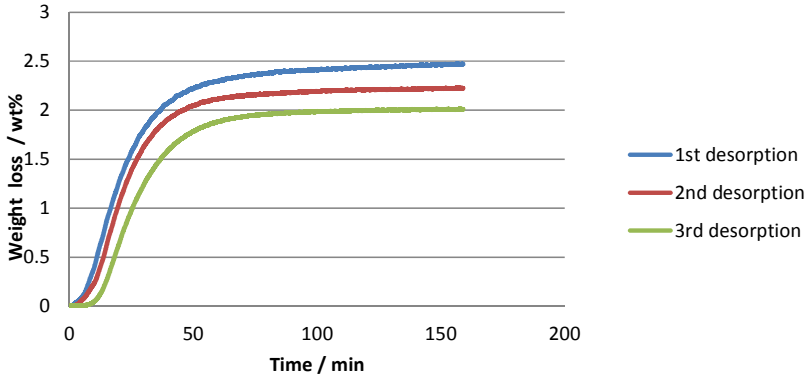

Figure 4.61: Cyclic desorption and absorption of N12L-72-T-6BN, calculated weight losses

As displayed in Figure 4.60 and Figure 4.61 both samples exhibit good recyclability and similar performance. Thus, within the range from 1.5 to 6 wt% BN, the effect of the additive on the sorption behavior of the $LiNH_2$+LiH system was constant.

4.2.6 Pressure Dependence of the Desorption Behavior

In this chapter results of hydrogen desorption cycling experiments are presented. Experiments were carried out with both the Belsorp-HP volumetric and the IsoSORP-MSB gravimetric system.

The experiments are desorption cycling experiments, because there was no absorption process between the individual desorption cycles. With Belsorp-HP system, the system was only cooled down to room temperature and evacuated (<$5*10^{-1}$ Pa) after one desorption experiment. With IsoSORP-MSB system, the experiment pressure was kept rather low (<1.4 kPa) compared with that in the Belsorp-HP system during the whole desorption processes. The desorption cycling experiments were performed in the Belsorp-HP system for 5 cycles and in IsoSORP-MSB gravimetric system for 2 cycles. For all experiments, the desorption temperature was 250°C.

The sample material was $LiNH_2$+1.2LiH with 3 wt% BN (N12L-72-T-3BN). The results of the Belsorp system (cf. Fig 4.62) demonstrate that at the first desorption round only 2.8 wt% weight loss were achieved. At the 5th round, the weight loss still amounted to approx. 0.75 wt%.

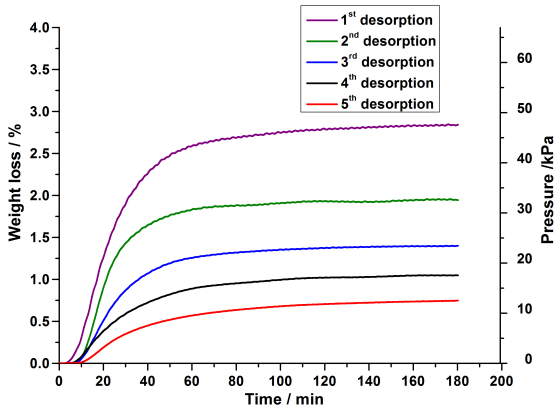

Figure 4.62: Desorption cycling of sample N12L-72-T-3BN at 250°C, Belsorp-HP system

With the IsoSORP-MSB gravimetric system a weight loss of 5.5% could be achieved after the 1st desorption cycle in the vacuum desorption condition. There was almost no further weight loss in the second round (see Figure 4.63). This result shows that the resulting weight loss of this hydrogen system is mainly pressure dependent.

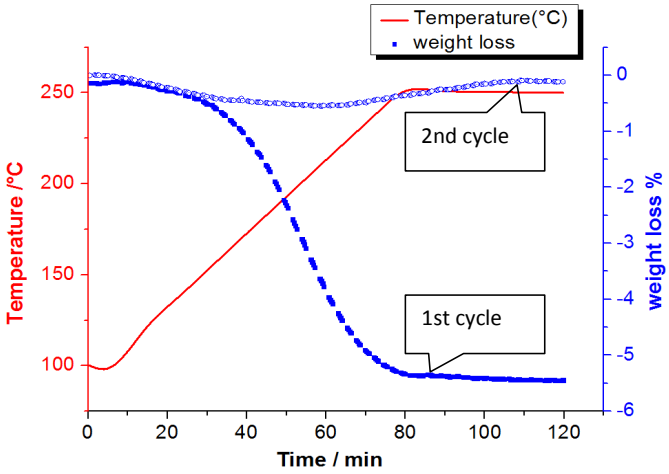

Figure 4.63: Desorption cycling experiment of sample N12L-3BN at 250°C, IsoSORP-MSB system

Based on the data obtained with these two systems, the relationship between the weight loss and pressure of the sample N12L-72-T-3BN is studied. It should be noticed that the resulting weight loss shown in Figure 4.62 for each cycle is not the final weight loss in each cycle because:

1 In the Beslorp-HP closed volumetric system, during the cooling down process, there is always a hydrogen re-absorption process following the desorption process (similar as shown in Fig 4.57). Due to these re-absorption phenomena, one cannot simply add the end pressures of all the completed cycles to obtain the accumulated desorbed amount. The re-absorption amount of each cycle was also recorded and considered in the calculation.

2. There is always a slight temperature influence on the pressure (cf. Fig 4.59), based on the temperature influence got in Figure 4.59, the pressure in each cycle was calibrated.

After calibration and calculation, the relationship between the desorption pressure and achieved weight loss is illustrated in Figure 4.64. The blue data point is got from the IsoSORP-MSB gravimetric system and red points are from the Belsorp-HP volumetric system. Combining the weight loss data and the particle sizes results (got from the SEM images), more useful information (e.g. diffusion length) could be calculated for the further modeling study (e.g. the model in Fig 2.9). So these data might serve as useful information for future model building.

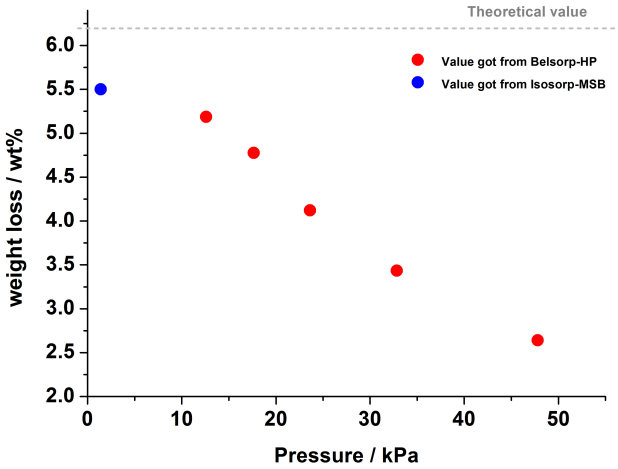

Figure 4.64: Accumulated results from the desorption cycling experiments performed in the Belsorp-HP (red dots) and IsoSORP-MSB system (blue dot), Sample: N12L-72-T-3BN, Temperature: 250°C

4.2.7 Theoretical Considerations on the Sorption Mechanism in the $LiNH_2$ Particle

4.2.7.1 Derivation of Formulas and Modeling

In order to understand the desorption process of the $LiNH_2$+LiH system, a model was developed based on thermodynamic and microstructure considerations. In addition, parameters such as

the system dead volume, sample amount, particle size, and desorption temperature were included.

As the desorption of $LiNH_2$ particles is the first step of the desorption process, the work of the model begins with the analysis of the desorption behaviour of $LiNH_2$ single component samples.

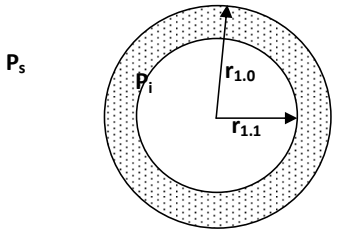

Figure 4.65: Graphical representation of the model (P_s: system NH_3 pressure, P_i: NH_3 pressure at the interface, $r_{1.0}$: initial particle radius, $r_{1.1}$: the inner radius of the $LiNH_2$ particle during desorption process)

Every $LiNH_2$ particle is considered a sphere (see Fig. 4.65). Initially, the radius of the $LiNH_2$ particle should be $r_{1.0.}$ During the desorption process, the inner radius of the $LiNH_2$ particle becomes $r_{1.1}$ and the surface shell forms the decomposition product Li_2NH. Ammonia desorbs at the interface and diffuses through the Li_2NH shell. The partial pressure of NH_3 at the $LiNH_2$-Li_2NH interface is P_i. The system pressure outside the particle is P_s. During the desorption process, the flow rate generated at the interface equals to the diffusion rate. If the flow rate of NH_3 through one such particle is $dN(NH_3)/dt$, then the following relationship exists at the reaction interface:

$$\frac{dN_{NH_3}(r)}{dt} = 4\pi {r_{1.1}}^2 \frac{P_i - P_{eq}}{P_{eq}} * k_0 \exp\left(-\frac{E}{RT}\right) \qquad \textbf{Equation 4.1}$$

$$\frac{dN_{NH_3}(r)}{dt} = A_1 {r_{1.1}}^2 (P_{eq} - P_i) \qquad \textbf{Equation 4.2}$$

with: P_{eq}: Equilibrium pressure

P_i: Pressure at interface between $LiNH_2$/Li_2NH

E: Activation energy

and:

$$A_1 = \frac{4\pi}{P_{eq}} * k_0 \exp(-\frac{E}{RT}) \quad \text{Equation 4.3}$$

Lu et al. [Lu96] have introduced a model describing the gas diffusion processes of gas-solid reaction base on the Darcy`s law. With this diffusion model, the NH_3 flow rate during the decomposition of $LiNH_2$ particles can be written as:

$$\frac{dN_{NH_3}(d)}{dt} = -\frac{4\pi r^2 D}{RT} \text{grad } P_{NH_3} \quad \text{Equation 4.4}$$

With: D: diffusivity of the gas

grad P_{NH3}: gradient of NH_3 pressure in the Li_2NH shell.

Integrated between $r_{1.1}$ and $r_{1.0}$:

$$\int_{P_i}^{P_s} dP = (\frac{dN_{NH_3}(d)}{dt}) \int_{r_{1,0}}^{r_{1.1}} \frac{RT}{4\pi r^2 D} dr \quad \text{Equation 4.5}$$

this results in

$$\frac{dN_{NH_3}(d)}{dt} = \frac{4\pi r_{1.0} r_{1.1} D}{RT(r_{1.0} - r_{1.1})} (P_i - P_s) \quad \text{Equation 4.6}$$

$$\frac{dN_{NH_3}(d)}{dt} = A_2 * \frac{r_{1.0} r_{1.1}}{r_{1.0} - r_{1.1}} (P_i - P_s) \quad \text{Equation 4.7}$$

with P_s: system pressure

and:

$$A_2 = \frac{4\pi D}{RT} \quad \text{Equation 4.8}$$

As the generated gas flow rate should be equal to the diffusion rate, the flow rates in Equation 4.2 and Equation 4.7 should be identical:

$$\frac{dN}{dt} = \frac{dN_{NH_3}(d)}{dt} = \frac{dN_{NH_3}(r)}{dt}. \quad \text{Equation 4.9}$$

With Equation 4.2 rearranged to

$$P_i = P_{eq} - \frac{\frac{dN_{NH_3}(r)}{dt}}{A_1 {r_{1.1}}^2}$$ **Equation 4.10**

and Equation 4.7 and Equation 4.9 combined, one can get:

$$\frac{dN}{dt} = A_2 \frac{r_{1.0} r_{1.1}}{r_{1.0} - r_{1.1}} (P_i - P_s) = A_2 \frac{r_{1.0} r_{1.1}}{r_{1.0} - r_{1.1}} (P_{eq} - \frac{\frac{dN}{dt}}{A_1 {r_{1.1}}^2} - P_s)$$ **Equation 4.11**

and

$$\frac{dN}{dt} = \frac{P_{eq} - P_s}{\frac{r_{1.0} - r_{1.1}}{A_2 r_{1.0} r_{1.0}} + \frac{1}{{r_{1.1}}^2 A_1}} = \frac{A_1 A_2 {r_{1.1}}^2 r_{1.0} (P_{eq} - P_s)}{(r_{1.0} - r_{1.1}) r_{1.1} A_1 + r_{1.0} A_2}.$$ **Equation 4.12**

In the Belsorp-HP system, the pressure changing rate should be:

$$\frac{dP_s}{dt} = \frac{dN}{dt} * \frac{RT}{V} * N_{particle} = \frac{dN}{dt} * A_3$$ **Equation 4.13**

with: V: the dead volume of the system

$N_{particle}$: the number of sample particles

R: the ideal gas constant

A3: constant depending on the sorption experimental environment

$$N_{particle} = \frac{\text{sample mass}}{\text{particle mass}} = \frac{\text{sample mass}}{\text{particle size} * \rho} = \frac{\text{sample mass}}{\frac{4}{3}\pi r^3 * \rho_{LiNH2}}$$ **Equation 4.14**

and A_3:

$$A_3 = \frac{RT}{V} * N_{particle}$$ **Equation 4.15**

As the system pressure P_s in the closed Belsorp-HP system is related to the amount of the reacted section of the $LiNH_2$ particles. Based on the reaction in Equation 2.10, every two molecules of reacted $LiNH_2$ correspond to one molecule of NH_3 in the closed system. This relationship can be written as:

$$\mathbf{P_s} = \frac{\frac{4}{3}(\mathbf{r_{1.0}}^3 - \mathbf{r_{1.1}}^3)\mathbf{N_{particle}} * \rho_{\mathbf{LiNH2}}\mathbf{RT}}{2 * \mathbf{M} * \mathbf{V}} \qquad \textbf{Equation 4.16}$$

with: M: Molar mass of $LiNH_2$

or

$$\boldsymbol{P_s} = \boldsymbol{A_4}(\boldsymbol{r_{1.0}}^3 - \boldsymbol{r_{1.1}}^3) \qquad \textbf{Equation 4.17}$$

with: $$\mathbf{A_4} = \frac{\frac{4}{3}N_{particle} * \rho_{\mathbf{LiNH2}}RT}{2\mathbf{M} * \mathbf{V}} \qquad \textbf{Equation 4.18}$$

Equation 4.17 can be rewritten as:

$$\boldsymbol{r_{1.1}} = \sqrt[3]{\boldsymbol{r_{1.0}}^3 - \frac{\boldsymbol{P_s}}{\boldsymbol{A_4}}} \qquad \textbf{Equation 4.19}$$

Put Equation 4.19 into Equation 4.12 results in:

$$\frac{\boldsymbol{dN}}{\boldsymbol{dt}} = \frac{\boldsymbol{A_1 A_2}\left(\boldsymbol{r_{1.0}}^3 - \frac{\boldsymbol{P}}{\boldsymbol{A_4}}\right)^{\frac{2}{3}} * \boldsymbol{r_{1.0}}(\boldsymbol{P_{eq}} - \boldsymbol{P_s})}{(\boldsymbol{r_{1.0}} - \sqrt[3]{\boldsymbol{r_{1.0}}^3 - \frac{\boldsymbol{P_s}}{\boldsymbol{A_4}}}) * \sqrt[3]{\boldsymbol{r_{1.0}}^3 - \frac{\boldsymbol{P_s}}{\boldsymbol{A_4}}} * \boldsymbol{A_1} + \boldsymbol{r_{1.0}} * \boldsymbol{A_2}} \qquad \textbf{Equation 4.20}$$

With Equation 4.20 put into Equation 4.13 finally results in:

$$\frac{\boldsymbol{dP_s}}{\boldsymbol{dt}} = \frac{\boldsymbol{dN}}{\boldsymbol{dt}} * \boldsymbol{A_3} = \frac{\boldsymbol{A_1 A_2 A_3}\left(\boldsymbol{r_{1.0}}^3 - \frac{\boldsymbol{P_s}}{\boldsymbol{A_4}}\right)^{\frac{2}{3}} * \boldsymbol{r_{1.0}}(\boldsymbol{P_{eq}} - \boldsymbol{P_s})}{(\boldsymbol{r_{1.0}} - \sqrt[3]{\boldsymbol{r_{1.0}}^3 - \frac{\boldsymbol{P}}{\boldsymbol{A_4}}}) * \sqrt[3]{\boldsymbol{r_{1.0}}^3 - \frac{\boldsymbol{P}}{\boldsymbol{A_4}}} * \boldsymbol{A_1} + \boldsymbol{r_{1.0}} * \boldsymbol{A_2}} \qquad \textbf{Equation 4.21}$$

In Equation 4.21, the pressure changing rate is a function of pressure. With the help MAPLE or similar software, the resulting system pressure profile over time can be calculated. The further work is to adjust the parameters.

4.2.7.2 Estimate of Constants for the Experimental System Used in This Study

In the Belsorp-HP system, the typical dead volume is around 40 cm^3. Based on the SEM images, the average particle size can be estimated as 200 nm. The diffusivity coefficient of NH_3 is 0.1978

cm^2/s [Mas97]. The density ρ of $LiNH_2$ is 19.44 cm^3/mol [Sha08a], the molar mass M is 23, and the temperature T was typically 523 K. With these values, Equation 4.8 and Equation 4.14 yields:

$$A_2 = \frac{4\pi D}{RT} = \frac{4*3.14*0.1978*10^{-4}}{8.314*523} = 5.71 * 10^{-8}$$ **Equation 4.22**

$$\mathrm{N_{particle}} = \frac{\text{sample mass}}{\frac{4}{3}\pi r^3 * \rho} = \frac{0.1}{\frac{4}{3}\pi*(1*10^{-7})^3*\frac{23}{19.44*10^{-6}}} = 2.01 * 10^{13}$$ **Equation 4.23**

Entering this $N_{particle}$ value into Equation 4.18, yields A_4 as:

$$\mathrm{A_4} = \frac{\frac{4}{3}N_{particle}*\rho RT}{\mathrm{M*V}} = \frac{4*1.61*10^{13}*\frac{23}{19.44*10^{-6}}*8.314*523}{2*3*23*40*10^{-6}} = 6.00 * 10^{25}$$ **Equation 4.24**

With the values for $N_{particle}$ and the dead volume V, A_3 from Equation 4.15 can be calculated as:

$$A_3 = \frac{RT}{V} * N_{particle} = \frac{8.314*523}{40*10^{-6}} * 2.01 * 10^{13} = 2.19 * 10^{21}\ \mathrm{K/m^3}$$ **Equation 4.25**

Apart from the parameters A_2, A_3, and A_4, A_1 was calculated based on the data got from one desorption experiment of sample $LiNH_2$-72-T. The calculation was done under the hypothesis that at the beginning desorption process, the sorption flow rate is only determined by the sorption kinetic but not the diffusion process. So with the experimental data, the A_1 value was calculated as $2.97*10^{-12}$. Put all the values in to Equation 4.21, with the help of MAPLE software, the resulting system pressure profile over time was calculated as shown in Figure 4.66.

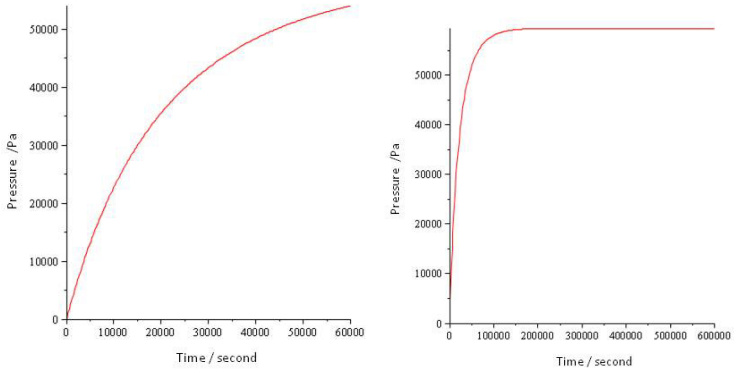

Figure 4.66: Pressure-Time plot calculated from Equation 4.21 with all parameters calculated above, T= 523 K (a): Time: 1-6*10^4 s, (b): Time: 0-6*10^5 s

Additionally, this model has also been applied at another, lower temperature (T=473 K). A_2, A_3, and A_4 were newly calculated based on Equation 4.8, Equation 4.15, and Equation 4.18. A_1 value was calculated based on the A_1 value got at 523 K and the activation energy of $LiNH_2$ desorption got in this study. The resulting system pressure profile over time was calculated as shown in Figure 4.68. In the figures it can be seen that at lower temperature, the desorption kinetic was largely reduced. It should be noticed that many parameters (such as $N_{particle}$, A_1 value, V) are rough values. So the pressure-time profiles showed in Figure 4.66 and Figure 4.67 are not exactly quantified results. However, sorption kinetic changing tendency under different temperatures is exactly as expect.

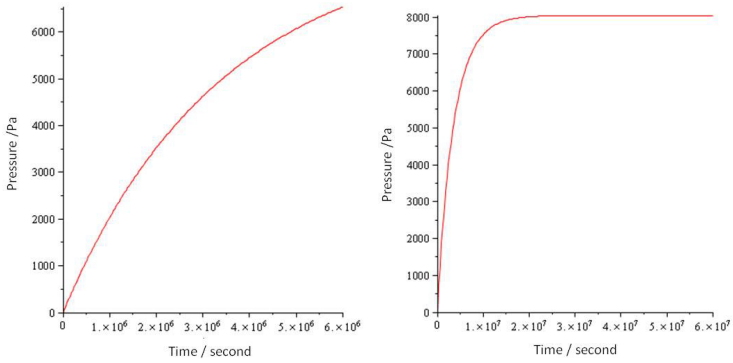

(a) (b)

Figure 4.67: Pressure-Time plot calculated T= 473 K (a): Time: 1-6*10^6 s, (b): Time: 0-6*10^7 s

Parameters A_1 and A_2 are related to the reaction mechanism and diffusion process, respectively. Their estimate is critical for model building. With the fixed calculated parameters A_4, A_3 and $N_{particle}$, it was interesting to find that with a fixed A_1 or A_2, the other parameter can be changed in a wider range without affecting the pressure-time curve. This may be a hint that either the decomposition or the diffusion is the rate-limiting step. Further investigation is still needed.

4.2.8 Alternative Doping of the $LiNH_2$ +LiH System

It has been found that 3 wt% of BN can improve the recyclability of the $LiNH_2$+LiH system very efficiently. As discussed in Chapter 2.3.2, Matsumoto et al. [Mat07] reported that $TiCl_3$ worked efficiently as additive with $LiNH_2$+LiH samples. As it is a well-understood system, $TiCl_4$ was applied as an alternative in this study. 3 wt% of $TiCl_4$ were added to the $LiNH_2$+LiH samples before they were wet ball milled with THF for 72 hours.

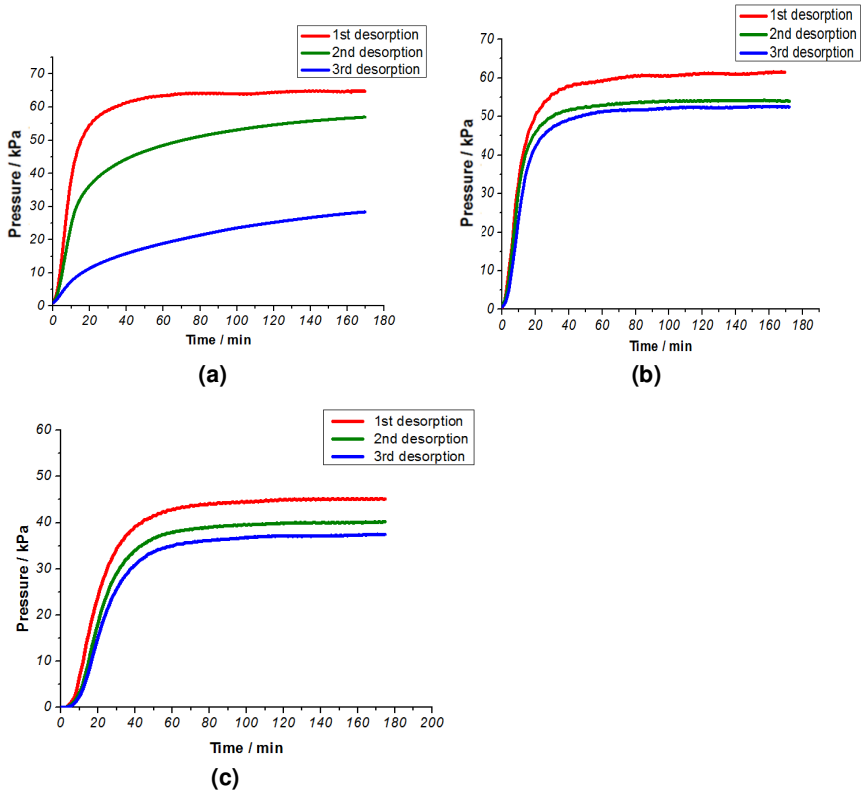

Figure 4.68: Hydrogen desorption and absorption cycling results as obtained in the Belsorp-HP system (a) without additive; (b) with 3 wt% BN; (c) with 3 wt% $TiCl_4$

After the milling process, a three-cycle hydrogen desorption/absorption experiment was performed in the Belsorp-HP volumetric system. The desorption temperature was 285°C and the absorption temperature 200°C, i.e., the same parameters as for the samples with BN (Chapter 4.2.5.1).

Figure 4.60 depicts the results obtained for $TiCl_4$ (cf. Figure 4.60c) in comparison to undoped (Figure 4.68a) and BN-doped (Fig. 4.60b) samples. $TiCl_4$ exhibited better recyclability as compared to undoped $LiNH_2$+LiH sample. In comparison to BN, however, the equilibrium pressure of the sample with $TiCl_4$ was lower than that with BN, making BN the more suitable additive.

4.3 $LiNH_2$+MgH_2 System

In this study the $2LiNH_2$+MgH_2 system was under investigation as an alternative system. Similar to the $LiNH_2$-LiH system, 20% excess of MgH_2 was used to absorb ammonia efficiently which means that the molecular ratio between $LiNH_2$ and MgH_2 was 2:1.2. The sample names and preparation methods applied are shown in Table 4.4:

Table 4.4: $LiNH_2$+MgH_2 sample names and preparation methods

Sample name	Milling time [hour]	Dry/wet ball milled	Milling ball diameter /(Ratio)	BN as Additive [wt%]
2N12Mg-24-D	24	dry	5 and 2 mm /(7:3)	_
2N12Mg-24-T	24	wet (with THF)	5 and 2 mm /(7:3)	_
2N12Mg-24-T-3BN	24	wet (with THF)	5 and 2 mm /(7:3)	3

4.3.1 SEM, XRD and BET Results

Figure 4.69 -4.70 show SEM images of the $LiNH_2$+MgH_2 samples with smaller (left side) and larger (right side) magnifications. The agglomeration sizes of the three samples were similar to each other (about 10-20 μm). Figure 4.72 gives the particle size distribution information of the three samples. It shows that the dry ball milled sample (2N12Mg-24-D) had larger particle size than the wet ball milled samples. Addition of 3 wt% of BN did not change the size and morphology of the sample particles clearly.

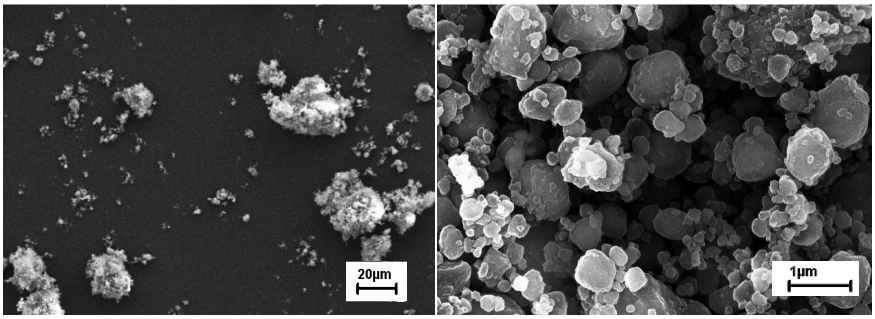

(a) (b)

Figure 4.69: SEM images of 2N12Mg-24-D

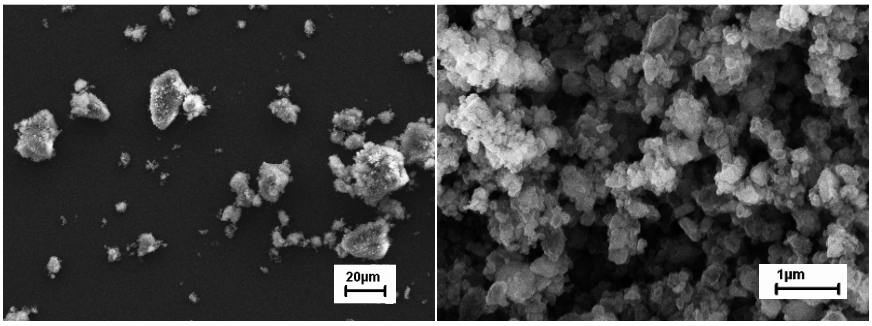

(a) (b)

Figure 4.70: SEM images of 2N12Mg-24-T

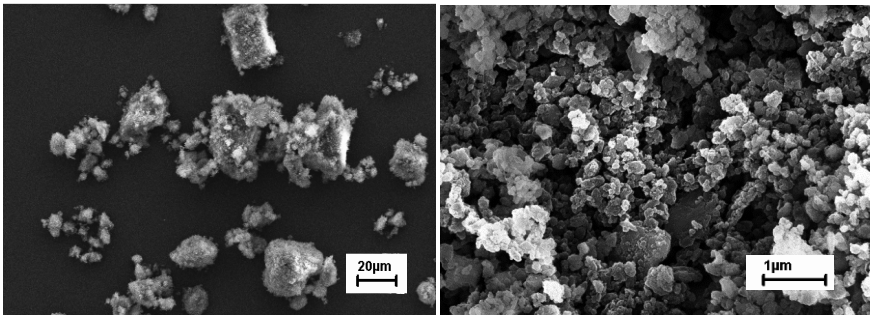

(a) (b)

Figure 4.71: SEM images of 2N12Mg-24-T-3BN

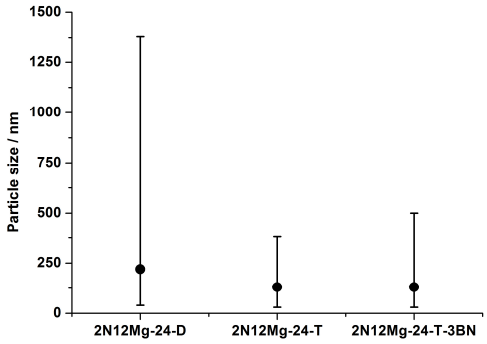

Figure 4.72: Particle size distribution of MgH_2+$LiNH_2$ as milled samples

The BET results given in Table 4.5 show a slightly larger specific surface area for the sample with additive. But the differences were not significant. The XRD patterns in Figure 4.73 of sample 2N12Mg-24 demonstrates that after 24 hours wet ball milling no obvious oxidation or other phase change with $LiNH_2$ or MgH_2 could be detected.

Table 4.5: Specific surface area results

sample	Specific surface area (m^2/g)
2N12Mg-24	78
2N12Mg-24-3BN	92

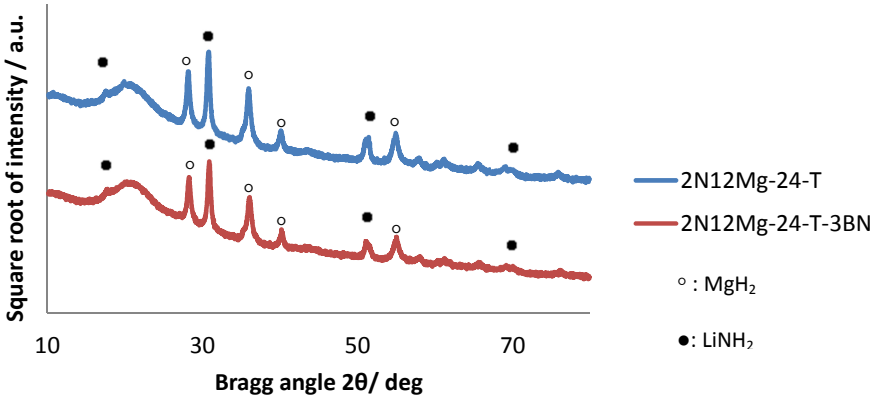

Figure 4.73: XRD pattern of sample 2N12Mg-24-T and 2N12Mg-24-T-3BN

4.3.2 Hydrogen Desorption and Absorption Cycles

Samples 2N12Mg-24-T and 2N12Mg-24-T-3BN were studied under the same desorption and absorption cycle conditions as described in Chapter 4.2.5.1, which means that desorption occurred at 285°C and absorption at 200°C for three hours each. The results are shown in Figure 4.74 and Figure 4.75.

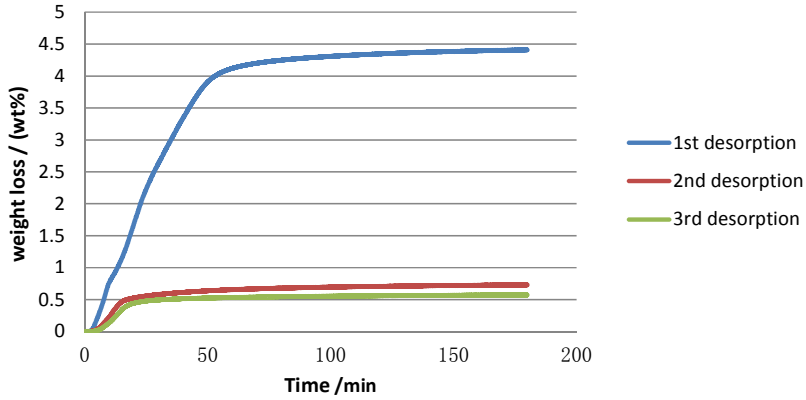

Figure 4.74: Cyclic sorption for 2N12Mg-24

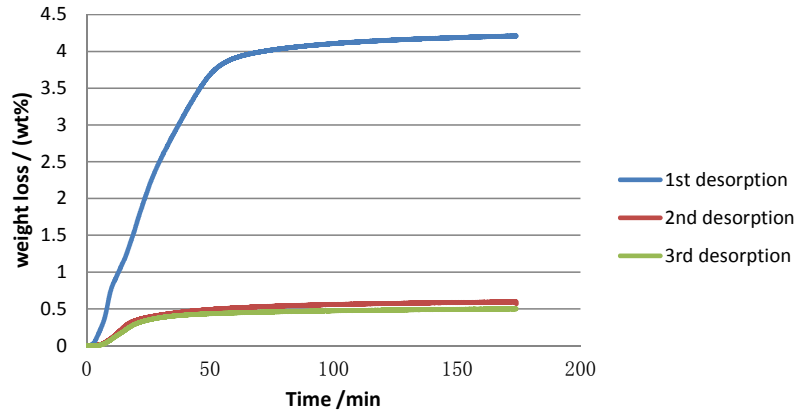

Figure 4.75: Cyclic sorption for 2N12Mg-24-3BN

From the results in Figures 4.65 and 4.66, respectively, one can see that the weight loss of the first cycle was higher than for the $LiNH_2$+LiH system (cf. Figs. 4.60 and 4.61). However, the

second and third cycles resulted in much lower weight loss. Unfortunately, this insufficient recyclability was not improved by the addition of 3 wt% of BN.

5. Summary and Conclusion

The specific aim of this work was to improve the property of hydrogen storage material, for example, recyclability. With high storage capacity and relatively low desorption temperature as compared to other complex hydride hydrogen storage materials, the $LiNH_2$+LiH system was the main subject of this thesis. A deeper understanding of its hydrogen desorption mechanism should be achieved by means of microstructure and thermodynamic studies.

As the desorption from $LiNH_2$ particles is the first step of the desorption process of the $LiNH_2$+LiH system, the work was divided into two main parts: the study of $LiNH_2$ samples and the study of $LiNH_2$+LiH samples.

5.1 $LiNH_2$

With regard to the $LiNH_2$ samples, it was found that all the ball milling processes applied (3-72 hours) successfully reduced the particle sizes of the samples. After 72 hours of wet ball milling, the particle sizes were successfully reduced to around 200 nm. XRD studies showed no phase change of $LiNH_2$ in the presence of tetrahydrofuran (THF). However, the wet ball milled samples with longer milling time tended to have larger crystallite sizes and lattice strain. Compared with the dry ball milled sample, within the same milling time the wet ball milled samples tended to have larger particle and crystallite size together with smaller lattice strain. This may due to the existence of liquid phase THF, the wet ball milled samples received less mechanical strain during the milling process. Similarly, the reduced oxidation of the wet ball milled $LiNH_2$ is also attributed to the liquid protective cover of THF during the milling process.

The presence of boron nitride (BN) as additive did not influence the microstructure of the samples, significantly. However, it was found that samples with BN had relatively lower desorption activation energies together with larger desorption kinetics so that a catalytic effect of BN could be presumed.

5.2 $LiNH_2$+LiH

Similar to the $LiNH_2$ samples, the samples with longer milling times tended to have larger specific surface areas. Measurements show that the samples possess higher specific surface area than reported in the literature. In contrast to the $LiNH_2$ samples, the wet ball milled samples tended to have approx. 20% larger specific surface areas as compared to dry ball milled samples. This indicated that the wet ball milling processes help to enlarge the specific surface areas of LiH but not of $LiNH_2$.

During the sample desorption process no release of was NH_3 detected by means of mass spectroscopy for the $LiNH_2$+LiH samples in contrast to the $LiNH_2$ single component specimens. Doping $LiNH_2$+LiH with BN did not change the microstructure of the sample powders but improved their recyclability, significantly. It has also been found that BN could lower the desorption activation energy but not influence the desorption enthalpy. All these results give a proof that BN is an efficient additive in the $LINH_2$+LiH system which works in the kinetic aspect. Furthermore, BN seemed to have a stabilizing effect on the crystallite size after the high temperature desorption and absorption processes. But within the range of 1.5 wt% to 6 wt% BN, there was no difference in desorption and recycling behaviour of the samples.

5.3 Reaction and Diffusion Mechanisms

Considering thermodynamic aspects together with the diffusion process during the desorption process permitted to develop a new model to describe the $LiNH_2$ particle desorption behaviour. Including several experimental parameters such as the system dead volume, the sample amount, particle size, and desorption temperature provided a general model, which after adjustment of a couple of parameters can be applied to other experimental conditions.

5.4 Outlook

The results obtained in this work indicate that specific surface area is not as critical for the $LiNH_2$ +LiH hydrogen storage system as thought. Further studies should concentrate more on thermodynamic aspects. Different from Ti-based catalysts, BN is not a widely used doping for hydrogen storage materials. An extended understanding of its working mechanism together with a refinement of the newly developed model could contribute to the development of $LiNH_2$+LiH and other hydrogen storage materials.

Recyclability, storage capacity, and operation temperature are the most important aspects to value the practical usefulness of a hydrogen storage material. In this study, the recyclability of $LiNH_2$+LiH samples could successfully be improved by BN doping. However, the target operational life with a requested number of desorption-absorption cycles in the range of 1000-1700 was not tested. Therefore, for practical purposes, the long-term behaviour of the material requires further work.

Regarding the storage aspect, a 5.5 wt% weight loss could be achieved with single-desorption experiments under vacuum condition. In the closed system, about 2 wt% hydrogen could be recycled stored at a desorption temperature of 250°C and an absorption temperature of 200°C. This is still too high for engineering considerations, where an operation temperature of approx. 100°C needs to be met. To improve the low-temperature desorption kinetic will still be a key point for further studies.

References

[Agu07]: K.F. Aguey-Zinsou, J. Yao, Z.X. Guo: Reaction Paths between $LiNH_2$ and LiH with Effects of Nitrides, The Journal of Physical Chemistry B, 111 (2007) 12531-12536.

[Akb07]: A.R. Akbarzadeh, V. Ozoliņš, C. Wolverton: First-Principles Determination of Multicomponent Hydride Phase Diagrams: Application to the Li-Mg-N-H System, 19 (2007) 3233-3239.

[Aki97]: E. Akiba, H. Iba: Hydrogen Absorption by Laves Phase Related BCC Solid Solution, Intermetallics, 6 (1998) 461-470.

[Au06]: M. Au, A. Jurgensen: Modified Lithium Borohydrides for Reversible Hydrogen Storage, The Journal of Physical Chemistry B, 110 (2006) 7062-7067.

[Bar06]: G. Barkhordarian, T. Klassen, R. Bormann: Catalytic Mechanism of Transition-metal Compounds on Mg Hydrogen Sorption Reaction, The Journal of Physical Chemistry B, 110 (2006) 11020–11024.

[Ben02]: R.W. Bentley: Global Oil & Gas Depletion: an Overview, Energy Policy 30 (2002) 189–205.

[Ble12]: Blewbury Energy Initiative: Hydrogen and Fuel Cells, 09 Mai 2011, http://www.blewbury.co.uk/energy/hydrogen.htm, 29 Mai 2013.

[Bos79]: P.G. Boswell: On the Calculation of Activation Energies Using a Modified Kissinger Method, Journal of Thermal Analysis, 18 (1980) 353-358.

[Bra13]: W.H. Bragg, W.L. Bragg: The Reflection of X-rays by Crystals, Proceedings of the Royal Society A, 88 (1913) 428-438.

[Bri10]: Bristol University - Gas Chromatography Mass Spectrometry (GC/MS): 14 Jan 2008, http://www.bris.ac.uk/nerclsmsf/techniques/gcms.html, 29 Mai 2013.

[Bro08]: D.P. Broom: Hydrogen Sorption Measurements on Potential Storage Materials: Experimental Methods and Measurement Accuracy, International Journal of Hydrogen Energy, 32 (2007) 4871-4888.

[Bro11]: D.P. Broom: Hydrogen Storage Materials: The Characterization of their storage properties, Springer, London (2011) 30.

[Bro11a]: D.P. Broom: Hydrogen Storage Materials: The Characterization of their storage properties, Springer, London (2011) 124.

[Bru38]: S. Brunauer, P.H. Emmett, E. Teller: Adsorption of Gases in Multimolecular Layers, Journal of the American Chemical Society, 60 (1938) 309-319.

[Che01]: J. Chen, N. Kuriyama, Q. Xu, T. Takeshita, T. Sakai: Reversible Hydrogen Storage via Titanium-Catalyzed $LiAlH_4$ and $LiAlH_6$, The Journal of Physical Chemistry B, 105 (2001) 11214-11220.

[Che01a]: H.-M. Cheng, Q.-H. Yang, C. Liu: Hydrogen Storage in Carbon Nanotubes, 39 (2001) 1447-1454.

[Che02]: P. Chen, Z. Xiong, J. Luo, J. Lin, L. Tan: Interaction of Hydrogen with Metal Nitrides and Imides, Nature, 420 (2002) 302-304.

[Che05]: Y.Chen, C.Z.Wu, P.Wang, H.M. Cheng: Structure and Hydrogen Storage Property of Ball Milled $LiNH_2/MgH_2$ Mixture, International Journal of Hydrogen Energy, 31 (2006) 1236-1240.

[Chh07]: D. Chhabil: Fundamentals of Contemporary Mass Spectrometry, Wiley-VCH, Weinheim, (2007).

[CIS07]: CIS Ingenieurbüro Seifert: Area-Max I - Schnellbestimmung spezifischer Oberflächen von Feststoffen nach DIN 66 132, http://www.areameter.de/media/Area-Pros-deut-web.pdf, 29. Mai 2013.

[Cro10]: F. Crotogino, S. Donadei, U. Bünger, H. Landinger: Large-Scale Hydrogen Underground Storage for Securing Future Energy Supplies, WHEC 2010 Proceedings - Parallel Sessions Book 4, D. Stolten, T. Grube (Eds.), Forschungszentrum Jülich (2010), 37-45.

[Dav02]: T. Davie: Fundamentals of Hydrology, 2nd edition, Taylor & Francis, London (2008) 139.

[Dew98]: J. Dewar: Preliminary Note on the Liquefaction of Hydrogen and Helium, Proceedings of the Royal Society of London, 63 (1898) 256-258.

[Dil00]: A.C. Dillon, T. Gennett, J. L. Alleman, K.M. Jones, P.A. Parilla, and M.J. Heben: Carbon Nanotube Materials for Hydrogen Storage, Proceedings of the 2000 DOE/NREL Hydrogen Program Review, May 8-10 (2000).

[Din01]: L.N. Dinh, C.M. Cecala, J.H. Leckey, M. Balooch: The Effects of Moisture on LiD Single Crystals Studied by Temperature-programmed Decomposition, Journal of Nuclear Materials, 295 (2001) 193-204.

[Du12]: L. Du, G. Mauer, R Vaßen: Study on the Effects of Wet Ball Milling and Boron Nitride Additive on Li-N-H Hydrogen Storage System, Energy Procedia, Volume 29, 2012, Pages 147–155.

[Ebe09]: U. Eberle, M. Felderhoff and F. Schueh: Chemical and Physical Solutions for Hydrogen Storage, Angewandte Chemie International Edition, 48 (2009) 6608-6630.

[Fan08]: Z.Z. Fang, P. Wang, T.E. Rufford, X.D. Kang, G.Q. Lu, H.M. Cheng: Kinetic and Thermodynamic-based Improvements of Lithium Borohydride Incorporated into Activated Carbon, Acta Materialia, 56 (2008) 6257-6263.

[Fri64]: H.L. Friedman: Kinetics of thermal degradation of char-forming plastics from thermogravimetry. Application to a phenolic plastic, Journal of Polymer Science Part C, 6 (1964) 183-195.

[Gao10]: J. Gao, P. Adelhelm, M.H.W. Verkuijlen, C. Rongeat: Confinement of $NaAlH_4$ in Nanoporous Carbon: Impact on H_2 Release, Reversibility, and Thermodynamics, The Journal of Physical Chemistry C 114 (2010) 4675-4682.

[God12]: A. Godula-Jopek, W. Jehle and J. Wellnitz: Hydrogen Storage Technologies, Wiley-VCH, Weinheim, (2012).

[Gro04]: W. Grochala, P. P. Edwards: Thermal Decomposition of the Non-Interstitial Hydrides for the Storage and Production of Hydrogen, Chemical Reviews, 104 (2004) 1283-1315.

[Her05]: J.F. Herbst, L.G. Hector: Energetics of the Li Amide / Li Imide Hydrogen Storage Reaction, Physical Review B 72 (2005) 125120-125127.

[Heu03]: L.K. Heung: On-Board Hydrogen Storage System Using Metal Hydride, Hydrogen Power: Theoretical and Engineering Solutions - Proceedings of the Hypothesis II Symposium, T.O. Saetre (Ed), Springer Netherlands, Dordrecht (1998) 251-256.

[Hin07]: S. Hino, T. Ichikawa, K. Tokoyoda, Y. Kojima, H. Fujii: Quantity of NH_3 Desorption Rom the Li–N–H Hydrogen Storage System Examined by Fourier Transform Infrared Spectroscopy, Journal of Alloys and Compounds, 446–447 (2007) 342–344.

[Hir10]: M. Hirscher (Ed): Handbook of Hydrogen Storage, Wiley-VCH, Weinheim (2010)

[Hof00]: J. H. van't Hoff: Die Gesetze des chemischen Gleichgewichtes für den verdünnten, gasförmigen oder gelösten Zustand, Engelmann, Leipzig (1900).

[Hu03]: Y.H. Hu, E. Ruckenstein: Ultrafast Reaction between LiH and NH_3 during H_2 Storage in Li_3N, The Journal of Physical Chemistry A, 107, (2003) 9739-9739.

[Hu05]: Y.H. Hu, E. Ruckenstein: High Reversible Hydrogen Capacity of $LiNH_2/Li_3N$ Mixtures, Industrial & Engineering Chemistry Research , 44 (2005) 1510-1513.

[Hua07]: C. Huang, H. Wu, Y. Li: Hydrogen Storage in Platelet Graphite Nanofibers, Seperation and Purification Technology, 58 (2007) 219-223.

[Hua11]: T.Q. Hua, R.K. Ahluwalia, J.K. Peng, M. Kromer, S. Lasher, K. McKenney, K. Law, J. Sinha: Technical Assessment of Compressed Hydrogen Storage Tank Systems for Automotive Applications, International Journal of Hydrogen Energy, 36 (2011) 3037–3049.

[Hwa08]: S.-J. Hwang, R.C. Bowman, J.W. Reiter, Job, G.L. Soloveichik, J.-C. Zhao, H. Kabbour, C.C. Ahn: NMR Confirmation for Formation of $[B_{12}H_{12}]^{2-}$ Complexes during Hydrogen Desorption from Metal Borohydrides, The Journal of Physical Chemistry C, 112 (2008) 3164-3169.

[Hyn96]: S. Hynek, W. Fuller and J. Bentley: Hydrogen Storage by Carbon Sorption, International Journal of Hydrogen Energy, 22 (1997) 601-610.

[Ich04]: T. Ichikawa, S. Isobe, N. Hanada, H. Fujii: Lithium Nitride for Reversible Hydrogen Storage, Journal of Alloys and Compounds, 365 (2004) 271–276.

[Ich04a]: T. Ichikawa, N. Hanada, S. Isobe, H.Leng, H. Fujii: Mechanism of Novel Reaction from $LiNH_2$ and LiH to Li_2NH and H_2 as a Promising Hydrogen Storage System, The Journal of Physical Chemistry B, 108 (2004) 7887-7892.

[Ich05a]: T. Ichikawa, N. Hanada, S. Isobe, H.Y. Leng, H. Fujii: Hydrogen storage properties in Ti catalyzed Li–N–H system, Journal of Alloys and Compounds 404–406 (2005) 435–438.

[Iso05]: S. Isobe, T. Ichikawa, N. Hanada, H.Y. Leng, M. Fichtner, O. Fuhr, H. Fujii: Effect of Ti catalyst with different chemical form on Li–N–H hydrogen storage properties, Journal of Alloys and Compounds 404–406 (2005) 439–442.

[Jan07]: R. Janot, J. Eymery, J. Tarascon: Investigation of the Processes for Reversible Hydrogen Storage in the Li–Mg–N–H System, Journal of Power Sources, 164 (2007) 496–502.

[Jim09]: V. Jimenez, P. Sanchez, J.A. Diaz, J.L. Valverde and A. Romero: Hydrogen Storage Capacity on Different Carbon Materials, Chemical Physics Letters, 485 (2010) 152-155.

[Kis57]: H.E. Kissinger: Reaction Kinetics in Differential Thermal Analysis, Analytical Chemistry, 29 (1957) 1702-1706.

[Kle13]: L.E. Klebanoff, J.O. Keller: 5 Years of hydrogen storage research in the U.S. DOE Metal Hydride Center of Excellence (MHCoE), International Journal of Hydrogen Energy, 38 (2013) 4533-4576.

[Kra03]: G. Krainz, G. Bartlok, P. Bodner, P. Casapicola, Ch. Doeller, F. Hofmeister, E. Neubacher, A. Zieger: Development of Automotive Liquid Hydrogen Storage Systems, AIP Conference Proceedings, 710 (2003) 35-40.

[Ku02]: C. Ku: Carbon Nanotubes for Hydrogen Storage, 31 November 02, http://www.sjsu.edu/faculty/selvaduray/page/papers/mate115/chiaoku.pdf, 29. Mai 2013.

[Kum11] T. Kume, Y. Matsumura, Y. Higaonna: Carbon material and electricity storage device, US-Patent US 20110195312 A1 (2011)

[Len04]: H. Leng, T. Ichikawa, S. Hino, N. Hanada, S. Isobe, and H. Fujii: New Metal-N-H System Composed of $Mg(NH_2)_2$ and LiH for Hydrogen Storage, The Journal of Physical Chemistry B , 108 (2004) 8763-8765.

[Lu07]: J. Lu, Z. Fang, Y.J. Choi, and H.Y. Sohn: Potential of Binary Lithium Magnesium Nitride for Hydrogen Storage Applications, The Journal of Physical Chemistry C, 111 (2007) 12129-12134.

[Lu10]: J. Lu, Y. J. Choi, Z.Z. Fang, H.Y. Sohn: Effect of milling intensity on the formation of LiMgN from the dehydrogenation of LiNH2–MgH2 (1:1) mixture, Journal of Power Sources, 195 (2010) 1992-1997.

[Lu96] H.-B. Lu, N. Mazet, Bernard Spinner: Modelling of Gas-Solid Reaction—Coupling of Heat and Mass Transfer with Chemical Reaction, Chemical Engineering Science, 51 (1996) 3829–3845.

[Luo04]: W. Luo: ($LiNH_2$–MgH_2): a Viable Hydrogen Storage System, Journal of Alloys and Compounds, 381 (2004) 284–287.

[Mar06]: T. Markmaitree, R. Ren, L. Shaw: Enhancement of Lithium Amide to Lithium Imide Transition via Mechanical Activation, The Journal of Physical Chemistry B, 110 (2006) 20710–20718.

[Mas97]: W. J. Massman: A Review of The Molecular Diffusivities of H_2O, CO_2, CH_4 ,CO, O_3, SO_2, NH_3, N_2O, NO, anf NO_2 in Air, O_2 and N_2 Near STP, Atmospheric Environment , 32 (1998) 1111-1127.

[Men10]: L. Meng: Improved Hydrogen Sorption Kinetics in Wet Ball Milled Mg Hydrides, Dissertation, Ruhr-Universität Bochum (2011).

[Mic10]: G. Miceli: First Principles Study of the $LiNH_2/Li_2NH$ Hydrogen Storage System, Dissertation, Università degli Studi di Milano-Bicocca (2010)

[Min94]: M.H. Mintz, Y. Zeiri: Hydrating Kinetics of Powders, Journal of Alloys and Compounds, 216 (1994) 159−175.

[Nak04]: Y. Nakamori, S. Orimo: Destabilization of Li-based Complex Hydrides, Journal of Alloys and Compounds, 370 (2004) 271.

[Nan13]: http://www.nanotechnologies.qc.ca/wp-content/uploads/2010/02/nanotubes_large.jpg, 29. Mai 2013.

[Nay11]: S. Nayebossadri, K. Aguey-Zinsou: Destabilisation of the Li–N–H Hydrogen Storage System with Elemental Si, Physical Chemistry Chemical Physics, 13 (2011) 17683–17688.

[Ohb06]: K. Miwa, M. Aoki, T. Noritake, N. Ohba, Y. Nakamori, S.-I. Towata, A. Züttel, S.-I. Orimo: Thermodynamical Stability of Calcium Borohydride $Ca(BH4)_2$, Physival Review B, 74 (2006) 155122-155126.

[Ori07]: S.-I. Orimo, Y. Nakamori, J.R. Eliseo, A. Züttel, C.M. Jensen: Complex Hydrides for Hydrogen Storage, Chemical Reviews, 107 (2007) 4111-4132.

[Osb09] W. Osborn, T. Markmaitree, L.D. Shaw, J.-Z. Hu, J. Kwak, Z. Yang: Low temperature milling of the $LiNH_2$ + LiH hydrogen storage system, International Journal of Hydrogen Energy, 34 (2009) 4331-4339.

[Oza57]: T. Ozawa: A New Method of Analyzing Thermogravimetric Data, Bulletin of the Chemical Society of Japan, 38 (1965) 1881-1886.

[Pen09]: F. Pendolino, Ph. Mauron, A. Borgschulte, and A. Züttel: Effect of Boron on the Activation Energy of the Decomposition of LiBH4, The Journal of Physical Chemistry C, 113 (2009) 17231-17234.

[Pil23]: N.B. Pilling, R.E. Bedworth: The Oxidation of Metals at High Temperature, Institute of Metals 29 (1923) 529.

[Ros03]: N.L. Rosi, J. Eckert, M. Eddaoudi, D.T. Vodak, J. Kim, M. O'Keeffe, O. M. Yaghi: Hydrogen Storage in Microporous Metal-Organic Frameworks, 300 (2003) 1127-1129.

[Rub10]: Rubotherm: Gravimetric Sorption Analyser with Magnetic Suspension Balance - Manual, (2010).

[Rub10a]: Rubotherm: Magnetic Suspension Balance - Manual, (2010)

[Sak07]: B. Sakintuna, F. Lamari-Darkrim, M. Hirscher: Metal Hydride Materials for Solid Hydrogen Storage: A Review, International Journal of Hydrogen Energy, 32 (2007) 1121-1140.

[Sat07]: S. Satyapal, J. Petrovic, C. Read, G. Thomas and G. Ordaz: The U.S. Department of Energy`s National Hydrogen Storage Project: Progress towards meeting hydrogen-powered vehicle requirements, Catalysis Today, 120 (2007) 246-256.

[Sch01]: L. Schlapbach, A. Züttel: Hydrogen Storage Materials for Mobile Applications, Nature, 414 (2001) 353-358.

[Sch18]: P. Scherrer: Bestimmung der Größe und der inneren Struktur von Kolloidteilchen mittels Röntgenstrahlen, Nachrichten von der Gesellschaft der Wissenschaften zu Göttingen, Mathematisch-Physikalische Klasse 1918 (1918) 98-100.

[Sha08]: R.R. Shahi, T.P. Yadav, M.A. Shaz, O.N. Srivastava: Effect of Mechanical Milling on Desorption Kinetics and Phase Transformation of $LiNH_2/MgH_2$ Mixture, International Journal of Hydrogen Energy 33 (2008) 6188-6194.

[Sha08a]: L.L. Shaw, W. Osborn, T. Markmaitree, X. Wan: The Reaction Pathway and Rate-limiting Step of Dehydrogenation of the $LiHN_2$ + LiH Mixture, Journal of Power Sources, 177 (2008) 500–505.

[Son06]: Y. Song, Z.X. Guo: Electronic Structure, Stability and Bonding of the Li-N-H Hydrogen Storage System, Physical Review B, 74 (2006) 195120-195126.

[Sta03]: M.J. Starink: The Determination of Activation Energy from Linear Heating Rate Experiments: A Comparison of the Accuracy of Isoconversion Methods, Thermochimica Acta, 404 (2003) 163-176.

[Str06]: R. Ströbel, J. Garche, P.T .Moseley, L. Jörissen: Hydrogen Storage by Carbon Materials, Journal of Power Sources, 159 (2006) 781-801.

[Tao06]: Z. Tao, M. Li: What is the limit of Chinese coal supplies—A STELLA model of Hubbert Peak, Energy Policy, 35 (2007) 3145–3154.

[Ter98]: R. Terry, K. Baker: Synthesis, Properties and Applications of Graphite Nanofibers, G.M. Holdrifge (Ed) Proceedings of WTEC Workshop (1998) 172-176.

[Tho97]: J.M. Thomas, W.J. Thomas: Principles and Practice of Heterogeneous Catalysis, Wiley-VCH, Weinheim (1997).

[Uni05]: United States Department of Energy: Freedom CAR Fuel Partnership: Hydrogen Storage Technologies Roadmap, United States Department of Energy, Washington (2005).

[Uni09]: United States Department of Energy, Office of Energy Efficiency and Renewable Energy and The FreedomCAR and Fuel Partnership: Targets for Onboard Hydrogen Storage Systems for Light-Duty Vehicles, Washington (2009).

[Var10]: R.A. Varin, T. Czujko, Z.S. Wronski: Nanomaterials for Solid State Hydrogen Storage, Springer, New York (2009).

[Var10a]: R.A. Varin, M. Jang, M. Polanski: The Effects of Ball Milling and Molar Ratio of LiH on the Hydrogen Storage Properties of Nanocrystalline Lithium Amide and Lithium Hydride ($LiNH_2$ + LiH) System, Journal of Alloys and Compounds 491 (2010) 658–667.

[Var11]: R.A. Varin, M. Jang: The Effects of Graphite on the Reversible Hydrogen Storage of Nanostructured Lithium Amide and Lithium Hydride ($LiNH_2$ + 1.2LiH) System, Journal of Alloys and Compounds, 509 (2011) 7143-7151.

[VBG12]: Verwaltungs-Berufsgenossenschaft (VBG) gesetzliche Unfallversicherun: BGI 5108: Wasserstoffsicherheit in Werkstätten, 3 Stand der Speichertechnik, http://www.vbg.de/apl/zh/bgi5108/3.htm, 29. Mai 2013.

[Ven11]: M. Vennila, G. Manikandan, V. Thanikachalam, J. Jayabharathi: Thermal Decomposition of N-(salicylidene)-L-leucine in Static Air Atmosphere, European Journal of Chemistry 2 (2011) 229-234.

[Wel09]: M. Swellons, P.A. Berseth, R. Zidan: Novel Catalytic Effects of Fullerene for $LiBH_4$ Hydrogen Uptake and Release, Nanotechnology, 20 (2009) 204022.

[Wil53]: G.K Williamson, W.H Hall: X-ray Line Broadening from Filed Aluminium and Wolfram, Acta Metallurgica, 1 (1953) 22–31.

[Xio05]: Z. Xiong, J. Hu, G. Wu, P. Chen, W. Luo, K. Gross, J. Wang: Thermodynamic and Kinetic Investigations of the Hydrogen Storage in the Li–Mg–N–H System, Journal of Alloys and Compounds, 398 (2005) 235–239.

[Yan03]: K. Yang, X. Wang, Y. Zhong, B. Wu, Y. Jin and B. Yang: Kinetics of Thermal Degradation and Thermal Oxidative Degradation of Poly(p-dioxanone), European Polymer Journal, 39 (2003) 1567-1574.

[Yao07]: J.H. Yao, C. Shang, K.F. Aguey-Zinsou, Z.X. Guo: Desorption Characteristics of Mechanically and Chemically Modified $LiNH_2$ and ($LiNH_2$ + LiH), Journal of Alloys and Compounds, 432 (2007) 277-282.

[Zha08]: D. Zhao, D. Yuan, H.-C: Zhou: The Current Status of Hydrogen Storage in Metal–Organic Frameworks, Energy & Environmental Science, 1 (2008) 222-235.

[Zue03]: A. Züttel: Materials for Hydrogen Storage, Materials Today, 6 (2003) 24-33.

Acknowledgments

During my work on this thesis, I have received much support and motivation from many people. Without their help, it would not have been possible for me to finish this work.

First I would like to express my sincere appreciation to Prof. Dr. Robert Vaßen for his great support of my work as my 'Doktorvater'. He gave me the chance to work on this topic and taught me how to do research. During my 3 years of Ph.D. research, he took time from his busy schedule to discuss my work with me every two weeks which I very much appreciate. He has given me a lot instructions and I will benefit from this kind of scientific attitude in my future career. I also want to give my thanks to Prof. Dr. Detlev Stöver for his following of the progress of my work, helpful suggestions and for having accepted to evaluate my thesis. I also want to thank Prof. Andreas Ostendorf for chairing my final defense.

I would like to convey my great thanks to Dr. Georg Mauer. During my three years of work, he gave me a lot of help and suggestions. More than that, he also made me know how to work efficiently and easily. I especially appreciate the "positive energy" that he gave to me. It will not only enhance my work in the future, but also my attitude towards life. I am very happy to get him as a good friend.

There are also many nice and helpful people who have made experiments with my samples. I want to give a lot of thanks to Marie-Theres Gerhards for her DTA-TG-MS measurements and her shining smile. I am grateful to Dr. Doris Sebold for her very good quality and timely SEM results of my samples. I also want to give much thanks to Sigrid Schwartz-Lückge for the effective BET results. I want to give thanks to Mirko Ziegner and his nice help with my XRD result analysis.

I want to give thanks to Volker Bader especially for his timely help of my work. I also want to thank Karl-Heinz Rauwald that he gave me a lot technical help, for example by building the exhaust pipe of the Belsop-HP and IsoSORP-MS systems, order and install the helium bottles,

and much more. I am grateful to Dr. Maria Ophelia Jarligo for her three years concern of my work, for her help with the lab work in Lab 133 and her help with the battery sample. I want to give thanks to Dr. Robert Mücke for his helping me using the Maple software.

I am very thankful to Dr. Qianli Ma. I am also very grateful to Dr. Li Meng who has given a lot of support and suggestions at the beginning of my work. I am also very thankful to Dr. Diana Marcano, Dr. Nan Meng, Dr. Ye Xing and Dr. Feng Han Dr. Alesandre Guignard for their concern and help with my work and life. I am also thankful to Yaping Song. Her independent work attitude gave me a positive effect.

I am very thankful to Dr. Dr. Ute Linz for her grammatical correction of my English, for her support of my German study and personal life and for the nice "Thursday lunches" in the last three years. I am very thankful to Dr. Jan Hoffmannn, Dr. Svenja Maria Ebert, Dr. Martin Bitzer, and Dr. Sebastian Vieweger for their help and discussion about the graduation formalities. I also want to give thanks to Gerd Mattonet, Tobias Offermanns and Fred Oellers from the workshop for their technical support. Thanks a lot to Dr. Wilhelm Albert Meulenberg for his consideration of my application for a Ph.D position at IEK-1 and for giving me a chance to do an application presentation. I want to give thanks to Hiltrud Moitroux, Stefan Weitz and Marianne Meyer for their support with my work in IEK-1. There are also many people that I want to give my thanks: Andrea Hilgers, Werner Herzhof, Dr. Mariya Inanova, Thomas Keuter, Rainer Kriescher, etc….

Special thanks must be given to my boyfriend Jan Eiberger for his support and help in all the aspects of my life and work, for his good cooking, positive energy, nice smiling, understanding and accompanying in the last two years. I also want to give my thanks to the family Eiberger. They are so nice with me and let me feel like home here in Germany. I am also thankful to the DPPS group who has made me feel very happy and love my life.

At the end I want to give great thanks to my mother and father. They are so great to give me unconditional support in every aspect of my life. Thanks to their love and giving me the chance to enjoy the wonderful life. Thanks also to my grandparents for their love.

Band / Volume 199
Improved characterization of river-aquifer interactions through data assimilation with the Ensemble Kalman Filter
W. Kurtz (2013), xxv, 125 pp
ISBN: 978-3-89336-925-6

Band / Volume 200
Innovative SANEX process for trivalent actinides separation from PUREX raffinate
A. Sypula (2013), 220 pp
ISBN: 978-3-89336-927-0

Band / Volume 201
Transport and deposition of functionalized multi-walled carbon nanotubes in porous media
D. Kasel (2013), 103 pp
ISBN: 978-3-89336-929-4

Band / Volume 202
Full-waveform inversion of surface ground penetrating radar data and coupled hydrogeophysical inversion for soil hydraulic property estimation
S. Busch (2013), 112 pp
ISBN: 978-3-89336-930-0

Band / Volume 203
Politikszenarien für den Klimaschutz VI – Treibhausgas-Emissionsszenarien bis zum Jahr 2030
Advances in Systems Analysis 5
P. Hansen, S. Gores und F. Chr. Matthes (Hrsg.)
(2013), XX, 257 pp
ISBN: 978-3-89336-932-4

Band / Volume 204
Effect of Composition, Microstructure and Component Thickness on the Oxidation Behaviour of Laves Phase Strengthened Interconnect Steel for Solid Oxide Fuel Cells (SOFC)
C. Asensio Jimenez (2014), 210 pp
ISBN: 978-3-89336-935-5

Band / Volume 205
Airborne VOC measurements on board the Zeppelin NT during the PEGASOS campaigns in 2012 deploying the improved Fast-GC-MSD System
J. Jäger (2014), VIII, 182 pp
ISBN: 978-3-89336-936-2

Band / Volume 206
Pulvermetallurgische Funktionsbauteile aus NiTi- und NiTi-X Legierungspulvern
M. Bitzer (2014), III, 144 pp
ISBN: 978-3-89336-937-9

Band / Volume 207
Zinkoxid: Einfluss von Dotierung und Legierungen auf elektro-optische Eigenschaften, auf das Ätzverhalten und auf die Tempernachbehandlung
M. Warzecha (2014), 8, vii, 170 pp
ISBN: 978-3-89336-938-6

Band / Volume 208
SGSreco - Radiologische Charakterisierung von Abfallfässern durch Segmentierte γ-Scan Messungen
T. H. Krings (2014), ix, 181, XI
ISBN: 978-3-89336-945-4

Band / Volume 209
Kühlkonzepte für Hochtemperatur-Polymerelektrolyt-Brennstoffzellen-Stacks
J. Supra (2014), III, 191 pp
ISBN: 978-3-89336-946-1

Band / Volume 210
Eigenschaften des Phosphorsäure-Polybenzimidazol-Systems in Hochtemperatur-Polymerelektrolyt-Brennstoffzellen
A. Majerus (2014), viii, 141 pp
ISBN: 978-3-89336-947-8

Band / Volume 211
Study on the Complex Li-N-H Hydrogen Storage System
L. Du (2014), I, 132 pp
ISBN: 978-3-89336-952-2

Energie & Umwelt / Energy & Environment
Band / Volume 211
ISBN 978-3-89336-952-2

JÜLICH
FORSCHUNGSZENTRUM